

Hyperelastic Modelling of Rubber Behaviour in Finite Element Software

Matthew Wadham-Gagnon
Department of Mechanical Engineering
McGill University
Montreal, Quebec, Canada
August 2006

A thesis submitted to McGill University in partial
fulfilment of the requirements of the degree of

Masters in Mechanical Engineering

©Matthew Wadham-Gagnon 2006
All rights reserved.



Library and
Archives Canada

Bibliothèque et
Archives Canada

Published Heritage
Branch

Direction du
Patrimoine de l'édition

395 Wellington Street
Ottawa ON K1A 0N4
Canada

395, rue Wellington
Ottawa ON K1A 0N4
Canada

Your file Votre référence

ISBN: 978-0-494-32625-1

Our file Notre référence

ISBN: 978-0-494-32625-1

NOTICE:

The author has granted a non-exclusive license allowing Library and Archives Canada to reproduce, publish, archive, preserve, conserve, communicate to the public by telecommunication or on the Internet, loan, distribute and sell theses worldwide, for commercial or non-commercial purposes, in microform, paper, electronic and/or any other formats.

The author retains copyright ownership and moral rights in this thesis. Neither the thesis nor substantial extracts from it may be printed or otherwise reproduced without the author's permission.

AVIS:

L'auteur a accordé une licence non exclusive permettant à la Bibliothèque et Archives Canada de reproduire, publier, archiver, sauvegarder, conserver, transmettre au public par télécommunication ou par l'Internet, prêter, distribuer et vendre des thèses partout dans le monde, à des fins commerciales ou autres, sur support microforme, papier, électronique et/ou autres formats.

L'auteur conserve la propriété du droit d'auteur et des droits moraux qui protègent cette thèse. Ni la thèse ni des extraits substantiels de celle-ci ne doivent être imprimés ou autrement reproduits sans son autorisation.

In compliance with the Canadian Privacy Act some supporting forms may have been removed from this thesis.

Conformément à la loi canadienne sur la protection de la vie privée, quelques formulaires secondaires ont été enlevés de cette thèse.

While these forms may be included in the document page count, their removal does not represent any loss of content from the thesis.

Bien que ces formulaires aient inclus dans la pagination, il n'y aura aucun contenu manquant.


Canada

Abstract

Experimental characterisation of rubber in uniaxial, equi-biaxial and planar tension under cyclic quasi-static loading shows strain-induced stress softening, hysteresis and unrecoverable strain. The objective of this work is to study the applications and limitations involved in predicting the behaviour of rubber with hyperelastic models. To assume a preconditioned perfectly elastic material, the data obtained from experiments must first be simplified. The data is then fitted to popular hyperelastic models in the finite element analysis (FEA) software ANSYS™. A single hyperelastic model (with given coefficients) is shown to only provide a good fit to a single characterisation test and level of preconditioning at the time. A two-iteration preconditioning method is developed using different hyperelastic models for a given material to approximate the softening effect of cyclic loading in a static FEA simulation. A biaxiality test is developed, providing information on the dominant mode of simple strain in the elements of a FE model. FEA simulations and experimental tests of a cantilevered rubber plate subjected to a bending load at its free end as well as a rubber guide lug subjected to a transverse deflection are presented and discussed. It is shown that using a single hyperelastic model is insufficient to predict the behaviour of these experiments in FEA simulations. The preconditioning iteration, when applied to these simulations, shows very good agreement with the experiments, both qualitatively and quantitatively. The biaxiality test provides insight on which characterisation test is the most appropriate for curve fitting hyperelastic models for a given analysis.

Sommaire

La caractérisation mécanique du caoutchouc par des essais quasi-statiques et cycliques sous tension uniaxiale, équi-biaxiale et planaire révèle un matériau comportant de l'adoucissement de contraintes induit par l'historique des déformations, de l'hystérésis ainsi que des déformations résiduelles. L'objectif principal de cette recherche est d'étudier les applications et les limitations des modèles hyperélastiques pour prédire le comportement du caoutchouc. Afin de réduire le comportement du matériau à un phénomène purement élastique, les données expérimentales de caractérisation ont dû d'abord être simplifiées. Ces données ont été ensuite soumises à une régression de courbe afin de déterminer les coefficients hyperélastiques du matériau pour quelques modèles hyperélastiques couramment disponibles dans les logiciels d'analyse par éléments finis tel que ANSYSTM. Il est démontré qu'un seul modèle hyperélastique propre (avec des coefficients déterminés) ne peut représenter convenablement qu'un seul test de caractérisation à un seul niveau de préconditionnement à la fois. Une itération de préconditionnement a été développée permettant de simuler l'adoucissement induit par la déformation quasi-statique et cyclique en utilisant plusieurs modèles hyperélastiques dans une même analyse par éléments finis. Un test de biaxialité a été également développé permettant d'identifier les régions de déformations dominantes dans le modèle d'éléments finis. Deux expériences ont été réalisées : la première est une plaque en porte-à-faux chargée en flexion, la deuxième porte sur la déflexion d'une dent guide typique des véhicules à chenilles. Les expériences ont été parallèlement simulées par des modèles d'éléments finis. Il est démontré que l'utilisation d'un seul modèle hyperélastique est insuffisante pour bien prédire le comportement expérimental du matériau. La méthode de préconditionnement, lorsqu'elle est appliquée aux simulations, semble grandement améliorer les prédictions numériques, qualitativement et quantitativement. Le test de biaxialité pour sa part peut aider à comprendre quel test de caractérisation est le plus approprié pour la régression hyperélastique.

Acknowledgements

Special thanks go to my supervisors, Professors Pascal Hubert and Michael P. Païdoussis, for going beyond their academic duties throughout this research project; their moral support and genuine friendliness was and will always be greatly appreciated. Professor Michael P. Païdoussis has been a mentor to me and I must thank him for being a source of inspiration through his professional habits and ethics. I must also express my deep gratitude to Professor Pascal Hubert for his guidance and particularly for his time and commitment in finalising this thesis.

I would like to thank Dr. Christian Semler for believing in me and providing the opportunity to work on an industrial project at ROI Engineering Inc. I greatly appreciated the freedom he gave me within the project definition and with my schedule.

Many thanks go to Martin Vézina and Faycal Ben Yahia from the ROI Engineering Inc. Montreal office; they have helped me on countless occasions with ANSYSTM. Special thanks to Faycal for all his assistance and endless generosity. I am grateful to have met Pablo Vasquez, also from the Montreal office, and would like to wish him the best of luck with his newly founded family. I would like to extend my gratitude to ROI Engineering's Toronto office, the people from which I am very pleased to have met, corresponded and/or worked with.

Thank you to Denys Lavoie, from Camoplast, Groupe Traction – Recherche et Développement, for providing the characterisation data for the rubber compound used in this work as well as the facilities and equipment to conduct the experimental bench tests. I also greatly appreciated working with Maxime Desjardins, an intern at Camoplast, with whom I conducted the experiments.

Special thanks go to Mary Fiorilli-St-Germain who has always been available to lend a cheerful and helping hand.

An expression of my appreciation goes to all of my colleagues at McGill with whom I have built friendships over the years. Thank you to Karine Lolei Khoun for helping me with the French version of my abstract. Special thanks go to Kostas Karagiozis for taking me under his wing back when I was “four feet tall”; and to Frederick Gosselin, a colleague, roommate and friend from day 1 at McGill: thanks for the several fruitful and inspiring discussions we have had over the years.

I would like to thank Isabelle for her love and support. She has been the sunshine in my life on numerous rainy days.

I would like to express immeasurable gratitude to my parents who have supported and encouraged me my entire life. I would particularly like to thank my mother for worrying for me so that I didn’t have to, and my father for helping me put things in perspective whenever it was necessary. I am grateful to my brothers Ben and Tom, whom I have grown closer to in the last few years and with whom have shared good times. And I am grateful to my entire extensive family, who are all fantastic and loving.

Finally, I would like to acknowledge the Natural Sciences and Engineering Research Council (NSERC) of Canada for providing support through an Industrial Postgraduate Scholarship (IPS) award. I would also like to acknowledge the support provided by ROI Engineering Inc, as the industrial partner in the IPS award, and for the SAMPE 2006 conference.

*“Man’s mind, once stretched by a new idea,
never regains its original dimensions”*

*--Oliver Wendell Holmes
Author, Poet & Physician*

Table of Contents

Abstract	i
Sommaire	ii
Acknowledgements	iii
Table of Contents	vi
List of Tables	ix
List of Figures	x
Chapter 1: Introduction	1
1.1. Rubber: historical review	1
1.2. Thesis outline	5
Chapter 2: The Mechanics of Rubber	7
2.1. General mechanics of rubber	7
2.1.1. Nonlinear elasticity	7
2.1.2. Hysteresis, strain induced stress-softening and preconditioning	9
2.1.3. Viscoelasticity (strain rate dependence, creep and relaxation)	12
2.1.4. Crystallization	13
2.2. Fundamental concepts of continuum mechanics	14
2.2.1. Deformation and strain	14
2.2.2. Strain invariants	18
2.2.3. Stress principles	19
2.2.4. Strain-energy function	20
2.3. Hyperelastic models	21
Chapter 3: Material Characterisation	25
3.1. Experimental procedure	27
3.1.1. Uniaxial tension test	32
3.1.2. Equi-biaxial extension test	33
3.1.3. Planar tension test	34
3.2. Curve-fitting	36
3.2.1. General curve-fitting procedure in ANSYS TM	38
3.2.2. Limitations of the hyperelastic models	47
Chapter 4: Hyperelasticity in ANSYS TM	51

4.1.	Selection and validation of finite element analysis options.....	51
4.1.1.	Element type and technology	52
4.1.2.	Element technology and formulation.....	53
4.1.3.	Element size	54
4.1.4.	Nonlinear solution control	55
4.1.5.	Finite element analysis validation with analytical solutions.....	55
4.2.	Modelling preconditioning	56
4.3.	Biaxiality test	58
4.4.	FEA procedure and methodology	60
Chapter 5: Bending of a Cantilevered Plate.....		63
5.1.	Experimental bench-test	63
5.1.1.	Experimental set-up and procedure	63
5.1.2.	Results from experimental bench-test.....	65
5.2.	Finite Element Simulations.....	67
5.2.1.	Finite element simulation problem definition.....	67
5.2.2.	FEA results using a simple hyperelastic model for the rubber	70
5.2.3.	Preconditioning iteration applied to the bending cantilevered plate.....	75
5.2.4.	Biaxiality test applied to the bending cantilevered plate	82
Chapter 6: Transverse Deflection of a Guide Lug		87
6.1.	Experimental bench-test	88
6.1.1.	Experimental set-up	88
6.1.2.	Results from experimental tests	91
6.2.	Finite Element Simulations.....	94
6.2.1.	Finite element simulation problem definition.....	94
6.2.2.	FEA results using a single hyperelastic model for the rubber	97
6.2.3.	Preconditioning macro applied to the bending cantilevered plate	98
6.2.4.	Biaxiality test applied to the deflecting guide lug problem	101
Chapter 7: Conclusion.....		106
References.....		109
Appendices.....		112
Appendix A: Strain energy derivation		113

Appendix B: Zero shift and corrected gauge length	116
Appendix C: Characterisation data	118
Appendix D: Curve-fitting demo in Workbench 10.0	123

List of Tables

Table 1: Table showing the expression for engineering stress, S_1, as a function of the stretch ratio, λ_1, for the uniaxial tension case ($\lambda_1 = \lambda$, $\lambda_2 = \lambda_3 = \lambda^{-1/2}$, $\sigma_1 = \sigma$, $\sigma_2 = \sigma_3 = 0$).....	24
Table 2: First-order Yeoh hyperelastic model coefficients (C_{10}) fitted to single characterisation curves as indicated with corresponding normalised root-mean-squared error, E_{NR}	45
Table 3: Third-order Yeoh hyperelastic model coefficients (C_{10}, C_{20} and C_{30}) fitted to single characterisation curves as indicated with corresponding normalised root-mean-squared error, E_{NR}	46
Table 4: Advantages and disadvantages of selected hyperelastic models.....	47
Table 5: Classification of elements according to their maximum principal strain	57
Table 6: Classification of elements according to their biaxiality ratio.....	60
Table 7: Geometric parameters for the bending cantilevered rubber plate bench test.....	64
Table 8: Hyperelastic models used in the first FEA simulation to be used in the preconditioning iteration.....	76
Table 9: Distribution of elements in the three regions of dominant deformation determined by the biaxiality test	85
Table 10 : Guide lug dimensions as labelled in Fig. 61.....	90
Table 11: Percentage distribution of elements in the three regions of dominant deformation defined by the biaxiality ratio when the FEA simulation is conducted with first-order Yeoh models.....	102
Table 12: Percentage distribution of elements in the three regions of dominant deformation defined by the biaxiality ratio when the FEA simulation is conducted with third-order Yeoh models.....	104

List of Figures

- Fig. 1: Schematic interpretation of the theory of long-chain molecules which compose rubber. (a) A long-chained molecule for natural rubber; (b) the reinforcing cross-linking of the natural rubber molecule.2**
- Fig. 2: 1912 Model T Ford. The Model T Ford series were in production from 1908 to 1927 and only late in the last year of production did black tires become standard; until then, white tires were used such as those shown above. Image and information taken from the Model T Ford Club of America website: www.mtfca.com.....3**
- Fig. 3: Qualitative representation of the nonlinear stress-strain relationship under simple extension observed in a rubber-like material, showing initial softening followed by stiffening near the elongation limit of the material.....4**
- Fig. 4: Equi-biaxial extension data from Treloar (1944) showing measured tension (kg/cm^2) with respect to extension ratio, λ8**
- Fig. 5: Stress-stretch curve for an unfilled rubber specimen in uniaxial tension; S is engineering stress expressed in MPa and λ is the stretch ratio. The dotted line, (...), represents the virgin stretch to high strain. The specimen is subjected to an incremental cyclic path, represented by the continuous lines (—), where it is first stretched to $\lambda = 2$, unloaded, then stretched to $\lambda = 3$, and so on until $\lambda = 6$. λ represents the stretch ratio, as defined in Section 2.2. The dashed lines (---) represent unrecoverable strain. Figure taken from Muhr (1999).9**
- Fig. 6: Stress-stretch curve for a filled rubber specimen under cyclic uniaxial tension; S is nominal stress expressed in MPa and λ is the stretch ratio. The dotted line, (...), represents the virgin stretch to high strain, the continuous lines (—) represent the cyclic path described in Fig. 5 and the dashed lines (---) show unrecoverable strain. Figure taken from Muhr (1999).10**
- Fig. 7: Cyclic loading stress-strain curve for liquid silicone rubber under uniaxial tension, the behaviour of which approaches the idealised Mullins effect; S is nominal stress expressed in MPa and λ is the stretch ratio. The dotted line, (...), represents the virgin stretch to high strain, the continuous lines (—) represent the cyclic path described in Fig. 5 and the dashed lines (---) show unrecoverable strain. Figure taken from Muhr (1999).11**
- Fig. 8: Preconditioning of a carbon-filled rubber specimen in simple tension. Figure taken from Dorfmann and Ogden (2003).12**
- Fig. 9: Schematic representation of viscoelastic behaviour. (a) Creep, a constant load is applied from $t = 0$ to $t = t_o$; when the load is completely removed a certain amount of strain is immediately recovered and more strain is recovered over time, without necessarily being a full recovery in this case. (b) Relaxation is depicted here; at a fixed amount of strain, the load decreases with time. (c) Strain rate effect; most materials become stiffer when loaded at higher strain rate.13**

Fig. 10: Position vectors \mathbf{X} and \mathbf{x} , defining points P and P' , respectively, as well as displacement vector \mathbf{u} are given in a Cartesian coordinate system.....	15
Fig. 11: Figure comparing the four finite strain definitions in simple extension, expressed in terms of: the stretch, λ ; natural strain, $\bar{\varepsilon} = \ln(\lambda)$; Lagrangian strain, $E = \frac{1}{2}(\lambda^2 - 1)$; Eulerian strain, $e = \frac{1}{2}(1 - \lambda^{-2})$; and engineering strain, $\varepsilon = \lambda - 1$	18
Fig. 12: Traction vector t_i acting on point P whose normal is n_i . This figure and caption are inspired from Mase and Mase (1999).	20
Fig. 13: Schematic representation demonstrating the equivalence between uniaxial tension and equi-biaxial compression ($\lambda_1 = \lambda$, $\lambda_2 = \lambda_3 = \lambda^{-1/2}$).....	25
Fig. 14: Schematic representation demonstrating the equivalence between equi-biaxial extension and uniaxial compression ($\lambda_1 = \lambda_2 = \lambda$, $\lambda_3 = \lambda^{-2}$).	26
Fig. 15: Schematic representation demonstrating the equivalence between a state of planar tension test and a state of pure shear ($\lambda_1 = \lambda$, $\lambda_2 = 1$, $\lambda_3 = \lambda^{-1}$).....	26
Fig. 16: Original data for the uniaxial tension test showing preconditioning at four different levels of strain: 5%, 10%, 15% and 25% nominal strain.	28
Fig. 17: The preconditioned loading cycles (dark continuous lines) extracted from the original data (grey lines) in uniaxial tension.	29
Fig. 18: The preconditioned loading cycles (dark full lines) extracted from the original data (grey lines) in planar tension.....	29
Fig. 19: The preconditioned loading cycles (dark continuous lines) extracted from the original data (grey lines) in equi-biaxial extension.	30
Fig. 20: Preconditioned curves, manipulated to eliminate the offset strain, for the uniaxial tension test.	31
Fig. 21: Stress-strain response of rubber at hand up to ~150% engineering strain (grey line). The strain range of interest in this thesis is relatively moderate (black line).....	31
Fig. 22: Picture of the uniaxial tension test set-up, courtesy of Axel Products Inc.	32
Fig. 23: Quarter model of a FEA simulation of the uniaxial tension test showing contours of the maximum principal strain, ε_1	33
Fig. 24: Equal-biaxial tension test, courtesy of Axel Products Inc.	34
Fig. 25: FEA model showing one sixteenth of the equi-biaxial extension testpiece, the contours are of the maximum principal strain, ε_1	34
Fig. 26: Planar tension test, courtesy of Axel Products Inc.....	35
Fig. 27: Quarter FEA model of the planar tension test showing contours of the middle principal strain, ε_2	35

Fig. 28: Mooney-Rivlin model with three parameters fitted to the uniaxial tension data preconditioned to 25% strain; $C_{10} = -19.969$ MPa, $C_{01} = 23.257$ MPa and $C_{11} = 13.536$ MPa.....	39
Fig. 29: Mooney-Rivlin model with three parameters fitted to the data preconditioned to 25% strain in all three states of simple stress simultaneously; $C_{10} = 2.2011$ MPa, $C_{01} = -0.27146$ MPa and $C_{11} = -0.36157$ MPa.	40
Fig. 30: Third-order Ogden model fitted to uniaxial tension data preconditioned to 25% strain; $\mu_1 = 196.78$ MPa, $\alpha_1 = 3.9680e-2$, $\mu_2 = -0.34627$ MPa, $\alpha_2 = -69.277$, $\mu_3 = -0.35077$ MPa and $\alpha_3 = 34.561$	41
Fig. 31: Third-order Ogden model fitted to data preconditioned to 25% strain in all three states of simple stress simultaneously; $\mu_1 = 99.319$ MPa, $\alpha_1 = -1.2080e-2$, $\mu_2 = 18.853$ MPa, $\alpha_2 = 7.4442$, $\mu_3 = -16.875$ MPa and $\alpha_3 = 7.7678$	42
Fig. 32: First-order Yeoh hyperelastic model fitted to characterisation data preconditioned to 25% engineering strain in (a) uniaxial tension, (b) planar tension and (c) equi-biaxial extension. The coefficients are given in Table 2.....	43
Fig. 33: Third-order Yeoh hyperelastic model fitted to characterisation data preconditioned to 25% engineering strain in (a) uniaxial tension, (b) planar tension and (c) equi-biaxial extension. The coefficients are given in Table 3.....	44
Fig. 34: Uniaxial tension data preconditioned to 15% (thick continuous line) then stretched beyond maximum preconditioning strain (dotted line). Ogden model: $\mu_1 = 208.41$ MPa, $\alpha_1 = 0.05305$, $\mu_2 = -0.40443$ MPa, $\alpha_2 = -123.08$, $\mu_3 = -0.4075$ MPa and $\alpha_3 = 61.4723$. 1 st order Yeoh model: $C_{10} = 2.6408$ MPa.	50
Fig. 35 : (a) 8-node linear hexahedral element (SOLID185), (b) 10-node quadratic tetrahedral element (SOLID187).	52
Fig. 36 : Hourglassing in two-dimensional linear elements showing: (a) a parallelogram type hourglass mode and (b) a trapezoid type hourglass mode. The original element shape is represented with a dashed line (---) while the hourglass mode is represented with a continuous line (—), the integration point is shown in the middle of each element.....	54
Fig. 37: Defined biaxiality ratios plotted against the maximum principal stretch, λ_1 . It is assumed that the biaxiality ratio of any incompressible element will have a value between α_B and α_U	59
Fig. 38: Flow chart describing the procedure to follow in order to perform a FEA simulation with the biaxiality test and preconditioning iteration.....	61
Fig. 39: Schematic representation of the experimental bench test of a cantilevered rubber plate subjected to a bending load, mg . The labels indicate the 1) rubber plate, 2) clamped section, 3) displacement gauge, 4) free section and 5) rigid steel bar.	64
Fig. 40: Loading paths only for load sets 1 and 2 of the bending cantilevered plate experiment.	66

Fig. 41: Loading and unloading paths for load sets 2, 3 and 4 of the bending cantilevered plate experiment. The arrows indicate whether it is a loading or unloading path.	66
Fig. 42: FEA model with boundary conditions for the bending cantilevered plate.	68
Fig. 43: Effect of refining the mesh in the FEA of the bending cantilevered plate modelled here with a first-order Yeoh hyperelastic model fitted to the planar characterisation data preconditioned to 10% engineering strain.....	69
Fig. 44: FEA predictions with a first-order Yeoh hyperelastic model fitted to the uniaxial tension characterisation data preconditioned to (a) 5%, (b) 10% and (c) 15% engineering strain.....	70
Fig. 45: FEA predictions with a first-order Yeoh hyperelastic model fitted to the planar tension characterisation data preconditioned to (a) 5%, (b) 10% and (c) 15% engineering strain.....	71
Fig. 46: FEA predictions with a first-order Yeoh hyperelastic model fitted to the equi-biaxial extension characterisation data preconditioned to (a) 5%, (b) 10% and (c) 15% engineering strain.	71
Fig. 47: FEA predictions with third-order Yeoh hyperelastic models fitted to the uniaxial tension characterisation data preconditioned to (a) 5% and (b) 10% engineering strain, as labelled in the figure.	73
Fig. 48: FEA predictions with third-order Yeoh hyperelastic models fitted to the planar tension characterisation data preconditioned to (a) 5% and (b) 10% engineering strain, as labelled in the figure.	74
Fig. 49: FEA predictions with third-order Yeoh hyperelastic models fitted to the equi-biaxial extension characterisation data preconditioned to (a) 5% and (b) 10% engineering strain.....	75
Fig. 50: Classification of elements according to their level of maximum principal strain for a simulation solved with the Y1ST_10P hyperelastic model. White: $0 < \bar{\epsilon}_1 \leq 0.005$; light grey: $0.005 < \bar{\epsilon}_1 \leq 0.03$; dark grey: $0.03 < \bar{\epsilon}_1 \leq 0.06$; black: $0.06 < \bar{\epsilon}_1 \leq 0.10$	77
Fig. 51: Classification of elements according to their level of maximum principal strain for a simulation solved with the Y1PT_10P hyperelastic model. White: $0 < \bar{\epsilon}_1 \leq 0.005$; light grey: $0.005 < \bar{\epsilon}_1 \leq 0.03$; dark grey: $0.03 < \bar{\epsilon}_1 \leq 0.06$	78
Fig. 52: Classification of elements according to their level of maximum principal strain for the simulation solved with the Y3PT_10P hyperelastic model. White: $0 < \bar{\epsilon}_1 \leq 0.005$; light grey: $0.005 < \bar{\epsilon}_1 \leq 0.03$; dark grey: $0.03 < \bar{\epsilon}_1 \leq 0.06$	78
Fig. 53: Predictions from the preconditioning iteration with first-order Yeoh hyperelastic models fitted to the uniaxial characterisation data for the second iteration. The FEA predictions are identified according to the hyperelastic model used in the first analysis.	79

Fig. 54: Predictions from the preconditioning iteration with first-order Yeoh hyperelastic models fitted to the planar characterisation data for the second iteration. The FEA predictions are identified according to the hyperelastic model used in the first analysis.	80
Fig. 55: Predictions from the preconditioning iteration with first-order Yeoh hyperelastic models fitted to the equi-biaxial characterisation data for the second iteration. The FEA predictions are identified according to the hyperelastic model used in the first analysis.	80
Fig. 56: FEA predictions following the preconditioning iteration where the elements were classified according to the strains from the first analysis with the Y1PT_10P hyperelastic model. The first-order Yeoh hyperelastic models used in the preconditioning (second) iteration were fitted to the (a) planar tension, (b) uniaxial tension and (c) equi-biaxial extension characterisation data.	81
Fig. 57: The elements not between the clamped surfaces plus the first row under the clamped surfaces (shown in grey) are submitted to the biaxiality test. The elements in white are neglected in the biaxiality test.	83
Fig. 58: Distribution of elements in the three regions of dominant deformation defined in the biaxiality test as a function of the predicted gauge displacement. These results were obtained with a first-order Yeoh hyperelastic model fitted to the planar characterisation data preconditioned to 10% engineering strain.	84
Fig. 59: Distribution of elements in the regions of dominant strain shown on the symmetrical half of the cantilevered plate subjected to a bending load at its free end; 1) region of dominantly planar deformations, 2) region of dominantly uniaxial deformation and 3) region of dominantly equi-biaxial deformation. A first-order Yeoh hyperelastic model was used fitted to the planar characterisation data preconditioned to 10% engineering strain.	85
Fig. 60 : Illustration of the experimental set-up for the guide lug deflection test. The dashed lines (---) delimit components that are not directly represented in the FEA model. The continuous lines (—) delimit the geometry that is modelled in the finite element analysis. Note that this illustration is not necessarily to scale.	88
Fig. 61: Schematic representation of the guide lug and pushing block used to deflect the guide lug transversally (X-direction). The labelled dimensions are defined in Table 10.	89
Fig. 62: Position of the displacement gauges used in the guide lug deflection experiments. Displacement gauge (1) measured the X-direction displacement of the deflection bar while displacement gauge (2) measured its displacement in the Y-direction. Displacement gauge (3) measured the X-direction displacement of the side of the guide lug opposite to the deflection bar. Displacement gauge (3) was centered in Z with respect to the guide lug geometry and positioned at a height $h = 71$ mm from the base of the guide lug.	91
Fig. 63: Experimental results showing the load-displacement path of the deflection bar for the 1 st , 2 nd , 3 rd , and 4 th loading cycles (no unloading recorded).	92
Fig. 64: Vertical (gauge 2) vs. horizontal (gauge 1) displacement of the deflection bar.	93

Fig. 65: Displacement measured at the third displacement gauge (from Fig. 62) vs. the horizontal displacement of the deflection block (second displacement gauge).	94
Fig. 66: Meshed guide lug and boundary conditions applied to designated faces.....	95
Fig. 67: Effect of refining the mesh in the FEA of the bending cantilevered plate modelled here with a first-order Yeoh hyperelastic model fitted to the planar characterisation data preconditioned to 10% engineering strain. Note that the percent change in load was calculated starting with the results from a global element size of 40 mm.	97
Fig. 68: Load-displacement predictions from the FEA model of the deflection of a guide lug compared to the experimental measurements. The first-order Yeoh model was fitted to uniaxial characterization data preconditioned to 5% engineering strain while the third-order Yeoh model fitted to planar characterization data preconditioned to 10% engineering strain.....	98
Fig. 69: Classification of elements according to their level of maximum principal strain for (a) load set 1, (b) load set 2, (c) load set 3. White: $0 < \bar{\epsilon}_1 \leq 0.005$; light grey: $0.005 < \bar{\epsilon}_1 \leq 0.03$; grey: $0.03 < \bar{\epsilon}_1 \leq 0.06$; dark grey: $0.06 < \bar{\epsilon}_1 \leq 0.10$; black: $\bar{\epsilon}_1 > 0.10$	99
Fig. 70: Load-displacement path for load set 2 from the preconditioning iteration with first-order Yeoh models fitted to (a) planar tension data, (b) uniaxial tension data, and (c) equi-biaxial extension data, for the second iteration.....	100
Fig. 71: Load-displacement path for load set 3 from the preconditioning iteration with first-order Yeoh models fitted to (a) planar tension data, (b) uniaxial tension data, and (c) equi-biaxial extension data, for the second iteration.....	100
Fig. 72: Load-displacement path for load set 4 from the preconditioning iteration with first-order Yeoh models fitted to (a) planar tension data, (b) uniaxial tension data, and (c) equi-biaxial extension data, for the second iteration.....	101
Fig. 73: 3810 elements (in grey) of the 4907 elements in the model are considered for the biaxiality test.	102
Fig. 74: Distribution of elements in the regions of dominant deformation for (a) load set 1, (b) load set 2 and (c) load set 3. Black: Region of dominant uniaxial tension; white: Region of dominant planar tension; grey: Region of dominant equi-biaxial tension.	103
Fig. 75: Distribution of elements in the regions of dominant deformation obtained with third-order Yeoh hyperelastic models fitted to planar characterisation data preconditioned to 10% for (a) load set 1, (b) load set 2 and (c) load set 3. Black: Region of dominant uniaxial tension; white: Region of dominant planar tension; grey: Region of dominant equi-biaxial tension.....	104

Chapter 1: Introduction

1.1. Rubber: historical review

Natural rubber comes from wounded tree/vine secretions, milky in appearance, thus the origin of the word *caoutchouc* derived from the Maya Indian words meaning “weeping wood” (Treloar, 1975). In their virgin form, these secretions contain mostly hydrocarbon (92-98%), known as latex, plus resin, minerals, proteins and water. The secretions are collected and heated to separate the latex from impurities. Although the most popular rubber tree in the industry is the *Hevea Braziliensis* (originating from South America), other flora species found around the world can also produce natural rubber, such as the *Funtumia Elastica* tree as well as a vine called the *Landolphia*, both found in Africa. Another tree, the *Ficus Elastica*, was discovered by British explorers in Southern Asia. Although none of these species have any direct botanical relation, they all contain the same hydrocarbon composition.

The Egyptians are said to have been the first to use natural rubber (Bettinali and Dusi, 2004). African and American tribes used the flexible material to make shoe soles and to play sports involving hitting a rubber ball with their knees and shoulders into a vertical hole on a wall[†]. But until the discovery of vulcanization, independently made in 1839 by Charles Goodyear and Thomas Hancock, rubber did not have much industrial potential due to its great sensitivity to the environment. Natural rubber becomes soft and sticky when slightly heated, then hard and brittle when cooled. Vulcanization modifies the physical properties of rubber such that it decreases its solubility in solvents, increases its tensile strength and resistance to heat, and maintains its elasticity at lower temperatures.

It is commonly accepted that, at the molecular level, natural rubber is composed of long-chain molecules, refer to Fig. 1(a) for a schematic representation of one long-chained molecule. Vulcanization (a.k.a. cross-linking or curing) is defined as the process of

[†] During a recent trip by the author to the ancient Maya ruins of Chichén Itzá in the Yucatán peninsula of Mexico, a tour guide described a similar sport where the captain of the winning team was sacrificed in a religious ceremony following the game. Whether the sacrifice was real or symbolic still remains to be determined.

linking the chains by chemical bonds to give an elastic three-dimensional network (Johnson, 2001). A visual interpretation of the cross-linking of a long-chained molecule is shown in Fig. 1(b). A curing agent, such as the sulphur that Goodyear would have accidentally dropped into a cooking pot of natural rubber, must be mixed to natural rubber for the chemical process to take place.

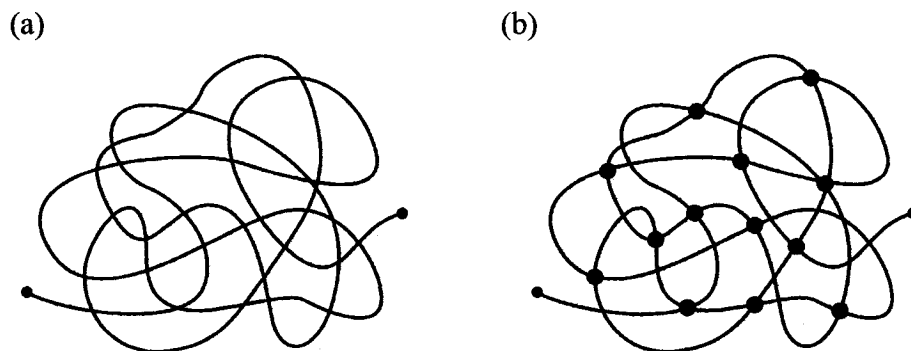


Fig. 1: Schematic interpretation of the theory of long-chain molecules which compose rubber. (a) A long-chained molecule for natural rubber; (b) the reinforcing cross-linking of the natural rubber molecule.

Zinc oxide was later found (late 19th century) to reinforce rubber, which may explain why the entire series of Model T Ford[‡] cars had white tires (see Fig. 2). Carbon black was initially only used as pigmentation in small concentrations, but when added in larger quantity it was also found to reinforce rubber and is probably today's most popular filler.

Rubber compounds are generally composed of a base rubber (e.g. natural rubber), a filler (e.g. carbon black) and a curing agent (e.g. sulphur). Additional components may include antioxidants, adhesion agents, flame retardant agents and special process-enhancing chemical additives. Common physical properties measured in compounds include hardness, ultimate tensile strength, ultimate elongation, rebound resilience as well as aging, tear, weather and fatigue resistance, to name a few. Every ingredient of a rubber recipe may affect these physical properties, independently or in concert with each other.

[‡] In the later years of production of the Model T Ford, black tires became optional and eventually, towards the end of the final year of production (1927), black tires (carbon black filled) became standard.

The mixing and curing process is also critical in determining these properties. Improving one compound property always results in changing other properties, for better or for worse (Dick, 2004).

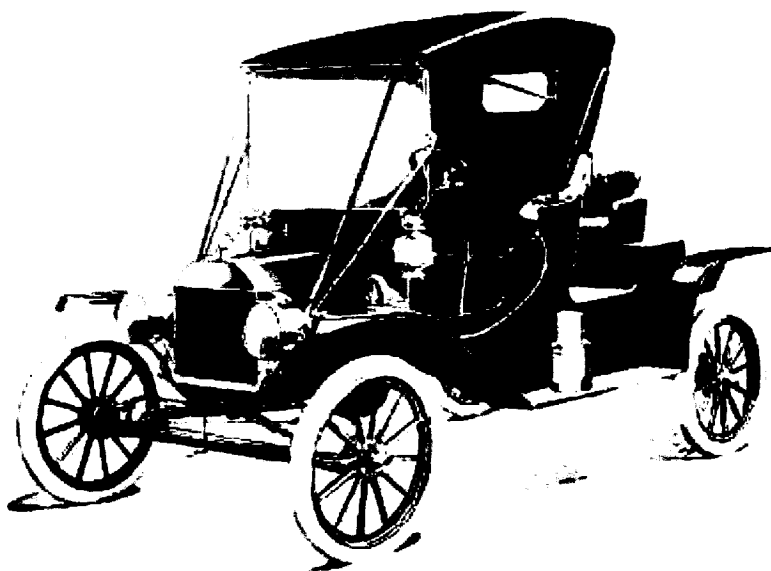


Fig. 2: 1912 Model T Ford. The Model T Ford series were in production from 1908 to 1927 and only late in the last year of production did black tires become standard; until then, white tires were used such as those shown above. Image and information taken from the Model T Ford Club of America website: www.mtfca.com.

Ultimately, chemists must trade-off some properties for others. For example, increasing the concentration of carbon black in a rubber compound will increase the ultimate tensile strength, the hardness, the rebound resilience and the tear resistance of the material; in exchange, the ultimate elongation of the compound will be reduced (Dick, 2004). Coming up with the right recipe and the appropriate process to meet consumer specifications can be very expensive. Most rubber manufacturers are very secretive about their formulations in order to maintain a competitive advantage (Dick, 2004).

Apart from evident relevance to the automotive industry, rubber compounds are used worldwide in multiple types of applications. They are used, for example, for their low electrical and thermal conductivity (e.g. wire coating, electrical component seals and o-

rings), for their capacity to absorb sound and vibration (e.g. seismic isolation bearings for buildings [see Bettinali and Dusi, 2004], mounts, bushings and connectors) and also for their impermeability (e.g. seals, rain coats and condoms). Rubber compounds would not be appropriate for any of the aforementioned applications if it weren't for the material's particular toughness and capability to recover from large deformations. In fact, some rubber compounds can stretch up to 5 or 6 times their original length.

Uniquely in terms of elasticity, the nonlinear stress-strain behaviour of rubber-like materials is characterised by the softening of the instantaneous modulus of elasticity at low and moderate strain, then sudden stiffening near the maximum strain of the material, as qualitatively depicted in Fig. 3. The first attempts to represent the elastic behaviour of rubber [described by Treloar (1943)] required considering finite deformation theory and led to constitutive material laws defined through strain energy functions, commonly referred to in this context as *hyperelasticity*. Treloar's (1943, 1944) pioneering work triggered further developments in hyperelastic models that particularly addressed the stiffening of rubber-like materials near their elongation limit. A more extensive review of existing hyperelastic models will be undertaken in Section 2.3.

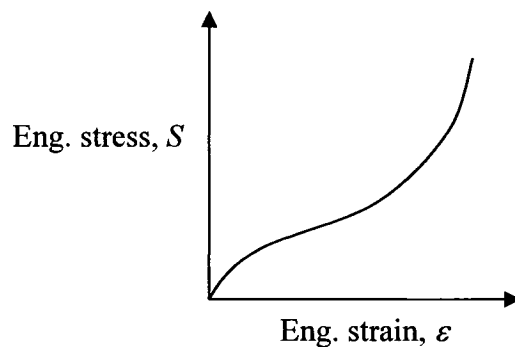


Fig. 3: Qualitative representation of the nonlinear stress-strain relationship under simple extension observed in a rubber-like material, showing initial softening followed by stiffening near the elongation limit of the material.

With the applications for rubber compounds growing exponentially emerged the desire to model and predict the mechanics of this particular material with FEA software packages. While hyperelastic models have been implemented in recent years to commercially

available FEA software packages, hyperelastic models alone will not always capture the complex mechanical behaviour of certain rubber or rubber-like materials, particularly carbon-black-filled compounds. These compounds will often exhibit hysteresis, strain-induced stress-softening, viscoelasticity and unrecoverable strain. There are therefore a certain number of necessary assumptions and limitations involved in using hyperelastic models in FEA software packages to predict the behaviour of certain rubbers; these assumptions and limitations are not very well understood.

1.2. Thesis outline

The applications and limitations of modelling the behaviour of carbon black filled rubber at moderate strain (0-25% engineering strain) uniquely with constitutive hyperelastic laws in commercial finite element analysis (FEA) packages (in this case ANSYS™) are investigated here.

For the considered hyperelastic models to apply, the material that is characterised must adhere to certain assumptions, which are:

- (i) the material is incompressible;
- (ii) deformations are quasi-static (no strain-rate effects);
- (iii) internal heat generation is negligible (isothermal);
- (iv) the mechanical behaviour of the material is purely elastic.

A brief examination of the general mechanical behaviour of rubber is first undertaken in Chapter 2, followed by a review of the underlying concepts of continuum mechanics for large deformations, stress, strain and strain energy density. A chronological glance at the development of constitutive hyperelastic material laws concludes this chapter.

Experimental characterisation data is provided from which the elastic behaviour of the material is extracted. Chapter 3 presents the data, how it was obtained, how it is used to obtain constitutive hyperelastic relations and how it is fitted to hyperelastic models in ANSYS™.

Considerations regarding the FEA options chosen for this work are briefly discussed in Chapter 4. Two iteration based routines are also described in Chapter 4: one to account for the strain-induced stress-softening typically observed in carbon-black-filled rubber. The second routine serves to predict the dominant state of strain (uniaxial, planar or equibiaxial) of elements under multiaxial loading.

The simple experiment of bending a cantilevered rubber plate is described in Chapter 5 and FEA simulations are compared to the experimental measurements. Chapter 6 describes experiments consisting in deflecting of a rubber guide lug typically used in tracked vehicles. FEA simulations of the experimental bench tests were also conducted. The comparison of the experimental data with the FEA predictions demonstrates the degree of accuracy achieved and exposes the limitations of hyperelastic models fitted to the characterisation data of Chapter 3. The preconditioning iteration and the biaxiality test are applied to these simulations as well.

Finally, in Chapter 7, concluding remarks and observations are discussed with respect to the assumptions, data manipulations and experimental procedures. Ideas for future work are proposed.

Chapter 2: The Mechanics of Rubber

The general mechanical behaviour of rubber is presented in Section 2.1 so that the reader fully understands the complexity of the material at hand as well as the assumptions involved in using hyperelastic models. A brief review of fundamental concepts in solid mechanics constitutes Section 2.2, namely definitions of nominal versus true stress and strain, stretch ratio, strain energy, principal strain and strain invariants. These are provided as quick reference for the discussion that follows on the different hyperelastic models presented in Section 2.3. Hyperelastic models, where incompressibility is assumed, are presented in historical order and only some are discussed in more detail.

2.1. General mechanics of rubber

Many observations can be made from the stress-strain behaviour of rubber. These observations are discussed in this section in a general manner. First the nonlinear elastic behaviour of rubber is described, disregarding any other phenomena. The next section discusses hysteresis, the so-called Mullins effect and preconditioning. Finally, viscoelasticity and crystallization are discussed before being discarded via the original assumptions.

It is common practice to present the stress-strain data collected from experimental characterisation of rubber behaviour in terms of engineering stress and engineering strain or extension ratio. Although stress and strain definitions will be discussed in more mathematical detail in the subsequent section, it will suffice for now to define the engineering stress, S , as the applied load, P , divided by the reference cross-sectional area, A_o . The engineering strain, ε , is the change in length, $\Delta L = L - L_o$, divided by the reference length, L_o , whereas the extension (a.k.a. stretch) ratio, λ , is defined as the current length, L , divided by the reference length, L_o .

2.1.1. Nonlinear elasticity

Treloar (1944) performed pioneering work in rubber characterisation by collecting experimental data for vulcanized natural rubber with 8% sulphur at large extensions in

uniaxial, equi-biaxial and planar tension. A specimen that is stretched equally in two orthogonal directions is said to be in equi-biaxial extension. Equi-biaxial extension is often assumed to be equivalent to uniaxial compression and can be measured in various ways. Treloar (1944) inflated a circular rubber disk clamped around its circumference into the shape of a balloon to reproduce the state of equi-biaxial extension. It is noted that the “tension” units he uses are not the conventional units of force, in [N], but rather in $[\text{kg}/\text{cm}^2]$, defined from the pressure measurement in mm of mercury.

The stress-stretch loading path of the equi-biaxial extension test conducted by Treloar is shown in Fig. 4. Although the unloading path is slightly different from the loading path, the difference (hysteresis) is considered negligible here (thus not shown) compared to the hysteretic behaviour that can be observed for other rubber compounds, particularly carbon-filled rubbers. It is clear that there is no linear relationship here between stress and strain, thus indicating the nonlinear nature of the elastic behaviour. Typically, the nonlinearity is characterised by an initial reduction in stiffness followed by an increase in stiffness as the strain approaches the physical limit (failure) of the material.

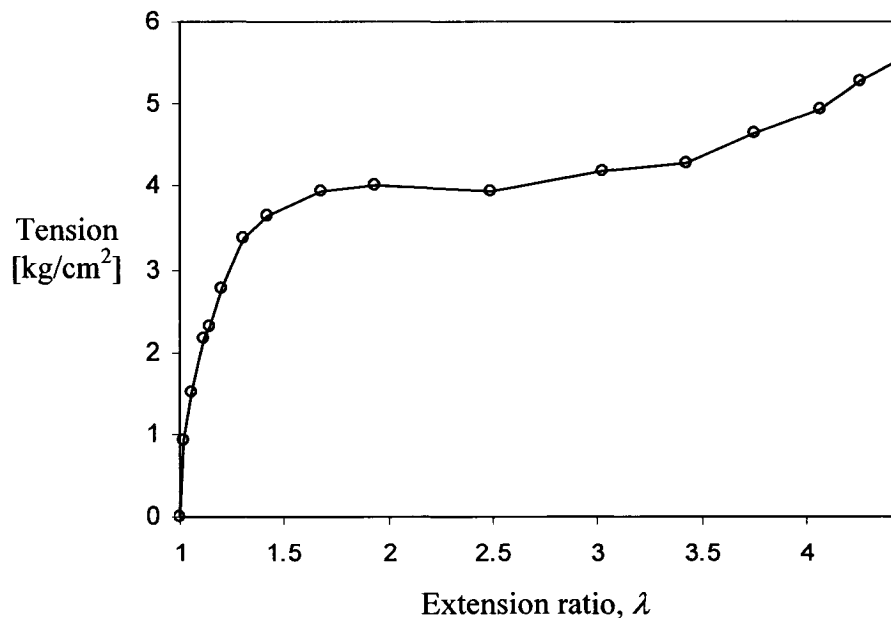


Fig. 4: Equi-biaxial extension data from Treloar (1944) showing measured tension (kg/cm^2) with respect to extension ratio, λ .

2.1.2. Hysteresis, strain induced stress-softening and preconditioning

Hysteresis occurs when the unloading path of a stress-strain curve is different from the loading path. Unfilled rubber shows little hysteretic behaviour, as it usually follows practically the same path during loading and unloading, only at lower strains, as shown in Fig. 5. Hysteresis becomes more pronounced when approaching ultimate elongations. Note that these observations and loading patterns are assumed to be time-independent, or quasi-static. For filled rubber, the loading stress-strain path is considerably different from the unloading path, as seen in Fig. 6.

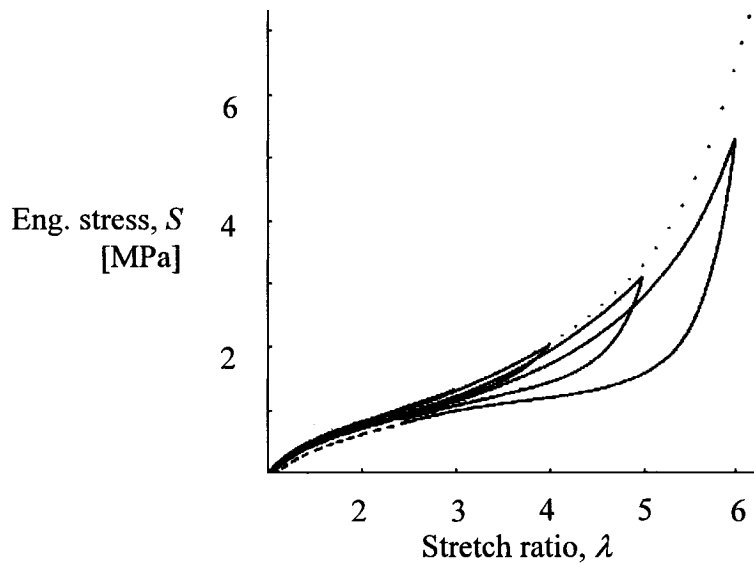


Fig. 5: Stress-stretch curve for an unfilled rubber specimen in uniaxial tension; S is engineering stress expressed in MPa and λ is the stretch ratio. The dotted line, (...), represents the virgin stretch to high strain. The specimen is subjected to an incremental cyclic path, represented by the continuous lines (—), where it is first stretched to $\lambda = 2$, unloaded, then stretched to $\lambda = 3$, and so on until $\lambda = 6$. λ represents the stretch ratio, as defined in Section 2.2. The dashed lines (---) represent unrecoverable strain. Figure taken from Muhr (1999).

The stress-strain path of the first stretch (virgin stretch) of a rubber testpiece is often observed to be different than subsequent stretches of the same specimen. This is known as *strain-induced stress-softening*, often called the *Mullins effect*, named after Mullins' (1969) outstanding original contributions to the study of this particular behaviour. Unfilled rubber usually only demonstrates noticeable stress-softening at higher strains, as

shown in Fig. 5. In contrast, filled rubber shows considerable stress softening even at relatively low strain (see Fig. 6). In Figs. 5 and 6, notice how the loading path of subsequent cycles is below the virgin stretch path of the testpiece.

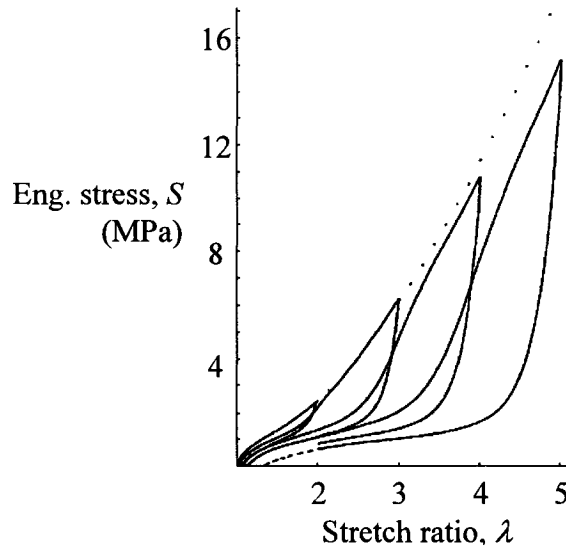


Fig. 6: Stress-stretch curve for a filled rubber specimen under cyclic uniaxial tension; S is nominal stress expressed in MPa and λ is the stretch ratio. The dotted line, (...), represents the virgin stretch to high strain, the continuous lines (—) represent the cyclic path described in Fig. 5 and the dashed lines (---) show unrecuperable strain. Figure taken from Muhr (1999).

The idealised Mullins effect occurs when the ensuing loading path follows the preceding unloading path until it stretches beyond the previously attained maximum strain; the stress-strain path then follows the virgin path. Liquid silicone rubber tested by Muhr (1999) nearly reproduces this idealised behaviour, as shown in Fig. 7. Note that in Figs. 5, 6 and 7 there is a certain amount of unrecuperable strain after the testpieces are fully unloaded, particularly when the loading stretch approaches the strain limit of the material. This can be attributed to the breaking of chemical links at the molecular level in the rubber.

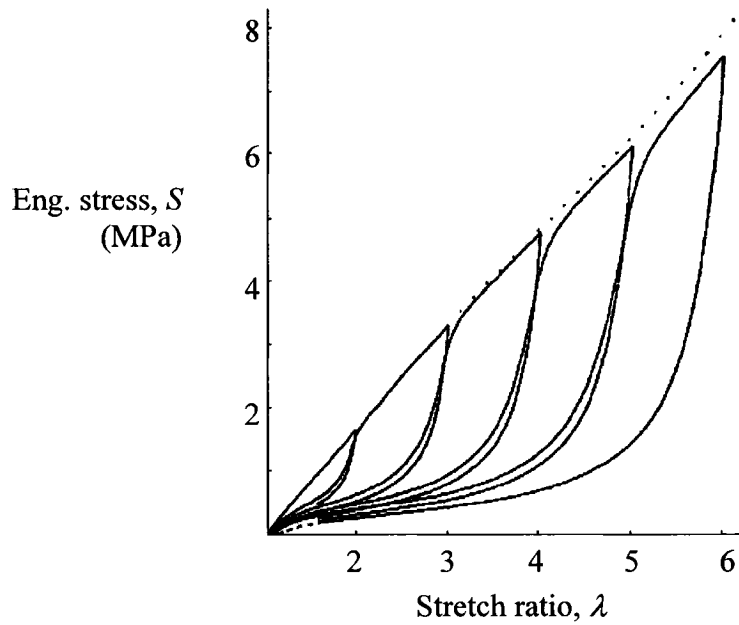


Fig. 7: Cyclic loading stress-strain curve for liquid silicone rubber under uniaxial tension, the behaviour of which approaches the idealised Mullins effect; S is nominal stress expressed in MPa and λ is the stretch ratio. The dotted line, (...), represents the virgin stretch to high strain, the continuous lines (—) represent the cyclic path described in Fig. 5 and the dashed lines (---) show unrecoverable strain. Figure taken from Muhr (1999).

Preconditioning is defined by loading and unloading a testpiece to the same stretch over several cycles, as demonstrated by Dorfmann and Ogden (2003) and shown in Fig. 8 for a carbon-filled rubber specimen in uniaxial tension, until the stress-strain path settles to a seemingly stable cycle.

The Mullins effect is actually considered to be temporary and usually the rubber recovers with time back to the virgin state. This can take hours, days, weeks or even months, depending on the material (Ogden, 2004).

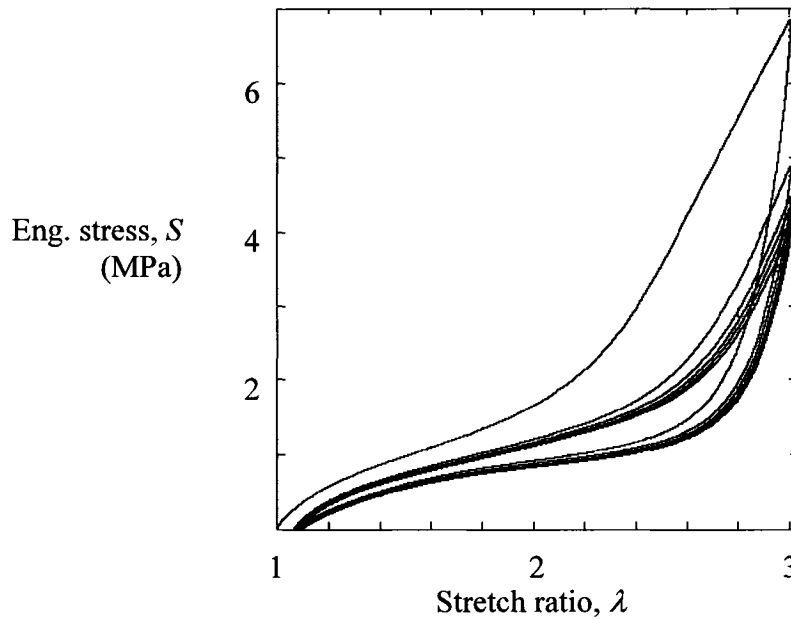


Fig. 8: Preconditioning of a carbon-filled rubber specimen in simple tension. Figure taken from Dorfmann and Ogden (2003).

2.1.3. Viscoelasticity (strain rate dependence, creep and relaxation)

Rubber is also known to demonstrate viscoelastic mechanical properties. Viscoelasticity may be observed in three different forms: creep, relaxation and strain rate dependence, all three described schematically in Fig. 9. Creep, Fig. 9(a), occurs when strain changes in time under a fixed load. A material is said to undergo relaxation, Fig. 9(b), when the load diminishes under a fixed state of strain. Finally, most materials have been observed to become stiffer for higher strain rates, Fig. 9(c). Refer to Mase and Mase (1999) for further discussion on viscoelasticity.

Due to the assumption of quasi-static loading, viscous effects will be neglected in this work.

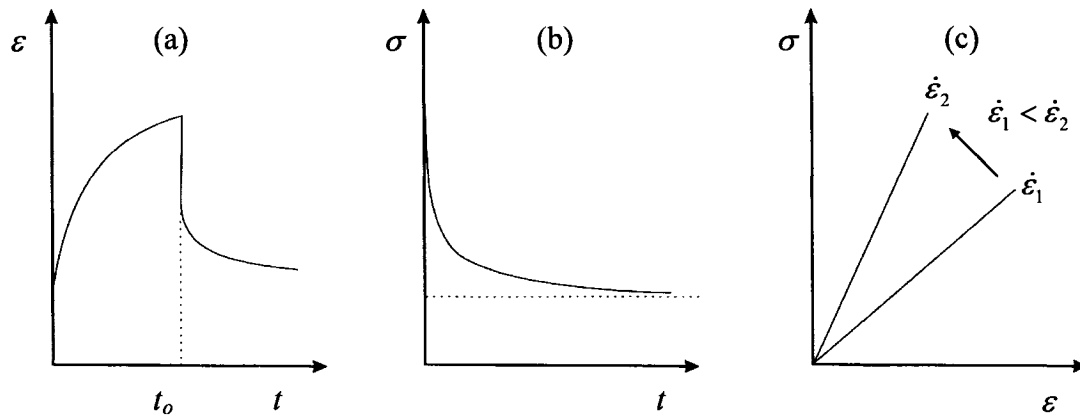


Fig. 9: Schematic representation of viscoelastic behaviour. (a) Creep, a constant load is applied from $t = 0$ to $t = t_0$; when the load is completely removed a certain amount of strain is immediately recovered and more strain is recovered over time, without necessarily being a full recovery in this case. (b) Relaxation is depicted here; at a fixed amount of strain, the load decreases with time. (c) Strain rate effect; most materials become stiffer when loaded at higher strain rate.

2.1.4. Crystallization

Under quasistatic loading, rubber is assumed not to generate any heat and stretching is accordingly generally considered to be isothermal. Müller and Strehlow (2004) described a simple experiment where a thin slab of natural rubber is quickly stretched up to 8 times its original gauge length. Internal heat generation brings the temperature of the rubber from the ambient 20°C to 45°C. If released before it has time to cool, the rubber specimen will recover its original form completely. It is thus said to be adiabatic in that there was no gain or loss of heat and no change in entropy. On the other hand, if the rubber specimen is held at its 8-fold stretch until it cools down to 20°C and then released, it remains stretched in a stress-free configuration; this is referred to as crystallization. If the stretched, stress-free slab of rubber is heated to 45°C, it recovers its original shape again. It can thereby be compared to a shape-memory alloy to some extent.

In this work, loading is quasi-static, and consequently the effects of internal heating such as crystallization are assumed to be negligible.

2.2. Fundamental concepts of continuum mechanics

A modicum of fundamental concepts in continuum mechanics is provided here, as theoretical background for large deformations and hyperelastic constitutive material relations. Most of the information provided in this section is extensively discussed in numerous publications. The interested reader is referred to Mase and Mase (1999) for a quite complete review of continuum mechanics, to Freed (1995) for a thorough synopsis of natural (Hencky) strain and strain rate, and finally to Ogden (2004) for a similar review of the basic concepts of continuum mechanics used in constitutive laws of hyperelasticity.

2.2.1. Deformation and strain

The starting point of continuum mechanics is the measurement of displacement and deformation in space. A given point, P , in a body is defined as having the reference position vector $\mathbf{X} = X_i \hat{\mathbf{e}}_i$ (refer to Fig. 10). Following a body deformation and/or motion, the new position of point P is defined by point P' which has the current position vector $\mathbf{x} = x_i \hat{\mathbf{e}}_i$. The reference position vector, \mathbf{X} , and the current position vector, \mathbf{x} , are related by the displacement vector, \mathbf{u} , such that

$$x_i = X_i + u_i. \quad (2.1)$$

Note that the italic font style, indicial form of vectors, such as X_i , or tensors, such as F_{ij} , is simply a different way of expressing their equivalent bold font style, matrix form, \mathbf{X} and \mathbf{F} , respectively. The differential form of Eq.(2.1) can be reduced to

$$dx_i = \frac{\partial x_i}{\partial X_j} dX_j = F_{ij} dX_j, \quad (2.2)$$

where F_{ij} , here in indicial form, is commonly known as the *deformation gradient tensor*, or simply the *deformation gradient*, \mathbf{F} , in matrix form.

The *right Cauchy-Green tensor*, \mathbf{C} , is obtained from the deformation gradient, such that

$$C_{ij} = F_{mi} F_{mj}, \quad (2.3)$$

or in matrix form,

$$\mathbf{C} = \mathbf{F}^T \cdot \mathbf{F}. \quad (2.4)$$

Similarly, the *left Cauchy-Green tensor*, \mathbf{B} , is defined by

$$B_{ij} = F_{im} F_{jm}, \quad (2.5)$$

or in matrix form,

$$\mathbf{B} = \mathbf{F} \cdot \mathbf{F}^T. \quad (2.6)$$

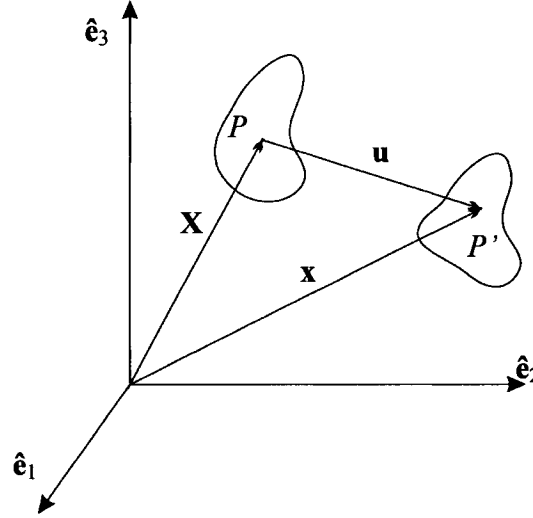


Fig. 10: Position vectors \mathbf{X} and \mathbf{x} , defining points P and P' , respectively, as well as displacement vector \mathbf{u} are given in a Cartesian coordinate system.

These tensor definitions lead to the first definitions of strain presented here for comparative purposes. The right Cauchy-Green tensor, \mathbf{C} , is used in obtaining the *Lagrangian* (a.k.a. *Green* or *covariant*) *finite strain tensor*, \mathbf{E} , which expresses a form of strain with respect to the reference state:

$$E_{ij} = \frac{1}{2} (C_{ij} - \delta_{ij}), \quad (2.7)$$

where δ_{ij} is the Kronecker delta function ($\delta_{ii} = 1$ and $\delta_{ij} = 0$ if $i \neq j$). The *Eulerian* (a.k.a. *Almansi* or *contravariant*) *finite strain tensor*, \mathbf{e} , which expresses a form of strain with respect to the deformed position, is

$$e_{ij} = \frac{1}{2} (\delta_{ij} - B_{ij}^{-1}). \quad (2.8)$$

Let us define the stretch ratio, λ , for a one-dimensional element of reference length L_o , and current length L , such that

$$\lambda = \frac{L}{L_o}. \quad (2.9)$$

The most familiar definition of strain may be the *principal engineering* (or *nominal*) *strain*, ε_i , which can simply be expressed as the change in reference length, $\Delta L = L - L_o$, over the reference length, L_o , and can be obtained directly from the principal stretch ratios, as follows:

$$\varepsilon_i = \lambda_i - 1. \quad (2.10)$$

By polar decomposition, the deformation gradient, \mathbf{F} , can be decomposed into two multiplicative tensors: an orthogonal *rotation tensor*, \mathbf{R} , and a positive definite, symmetric, *right stretch tensor*, \mathbf{U} , or *left stretch tensor*, \mathbf{V} , such that

$$\mathbf{F} = \mathbf{R} \cdot \mathbf{U} = \mathbf{V} \cdot \mathbf{R}. \quad (2.11)$$

The *Hencky* (a.k.a. *logarithmic* or *natural*) *strain tensor*, $\bar{\boldsymbol{\varepsilon}}$, can be obtained from the right stretch tensor, \mathbf{U} , as follows:

$$\bar{\boldsymbol{\varepsilon}} = \ln \mathbf{U}. \quad (2.12)$$

The right stretch tensor, \mathbf{U} , has eigenvalues λ_n provided the following can be solved:

$$\det[U_{ij} - \lambda_n \delta_{ij}] = 0. \quad (2.13)$$

The choice of symbol for the eigenvalues in Eq.(2.13) is not coincidental; the λ_n actually happen to be the principal stretch ratios as well. The principal Hencky strains, $\bar{\varepsilon}_i$, are thereby defined by the natural logarithms (hence the alternate name: logarithmic strain) of the principal stretches:

$$\bar{\varepsilon}_i = \ln(\lambda_i). \quad (2.14)$$

The eigenvalues, λ_n , have principal directions defined by the eigenvectors, \mathbf{e}_i , where the subscript i in this case refers to the vector associated with the principal direction concerned. Since the right stretch tensor is a second order tensor, Eq.(2.12), is determined through the spectral decomposition of \mathbf{U} :

$$\bar{\boldsymbol{\varepsilon}} = \sum_{i=1}^3 \left\{ \ln \lambda_i (\mathbf{e}_i \otimes \mathbf{e}_i) \right\}, \quad (2.15)$$

where the operator \otimes indicates a dyadic product. The Hencky strain can be viewed as the instantaneous change in length over the instantaneous gauge length.

The engineering strain and the Hencky strain, in the principal directions, are related as follows:

$$\bar{\varepsilon}_i = \ln(1 + \varepsilon_i), \quad (2.16)$$

or

$$\varepsilon_i = e^{\bar{\varepsilon}_i} - 1. \quad (2.17)$$

The relationship between engineering strain and Hencky strain is necessary in this context. Engineering (a.k.a. nominal) strain is usually used when collecting experimental data for its ease of measurement; it is the case with the characterisation data presented in this work. Logarithmic (a.k.a. natural or Hencky) strain is used in the finite element analysis (FEA) software ANSYS™ when large strain simulations are performed.

An interesting observation to make here is that the eigenvalues of the right Cauchy-Green tensor, \mathbf{C} , turn out to be λ_i^2 i.e. the square of the principal stretch ratios, since the following holds:

$$\det[C_{ij} - \lambda_i^2 \delta_{ij}] = 0. \quad (2.18)$$

Furthermore, the eigenvalues of the left Cauchy-Green tensor, from a similar analysis can be shown to be equal to λ_i^{-2} . Therefore, the principal logarithmic, Lagrangian, Eulerian and nominal strain tensors can all be defined by the principal stretch ratios, λ_i . Inspired from a figure given by Freed (1995), Fig. 11 shows the strain-stretch relationship of all four aforementioned strain definitions.

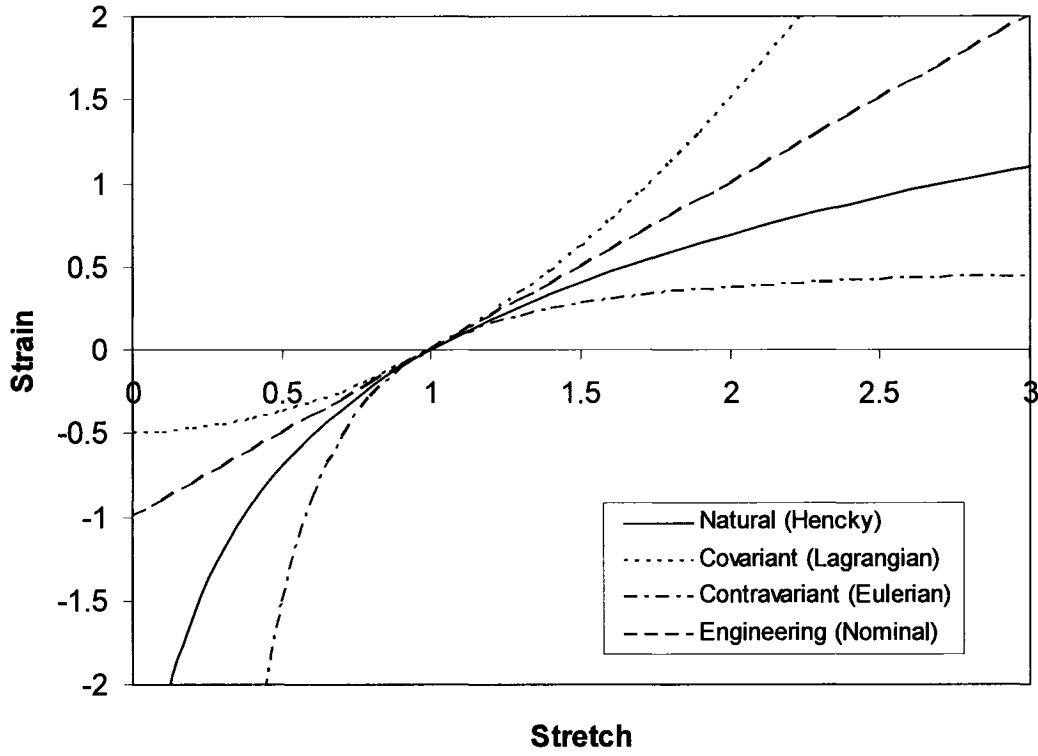


Fig. 11: Figure comparing the four finite strain definitions in simple extension, expressed in terms of: the stretch, λ ; natural strain, $\bar{\varepsilon} = \ln(\lambda)$; Lagrangian strain, $E = \frac{1}{2}(\lambda^2 - 1)$; Eulerian strain, $e = \frac{1}{2}(1 - \lambda^{-2})$; and engineering strain, $\varepsilon = \lambda - 1$.

2.2.2. Strain invariants

From the right Cauchy-Green tensor, \mathbf{C} , strain invariants can be defined such that they are constant regardless of the coordinate orientation:

$$\begin{aligned} I_1 &= \lambda_1^2 + \lambda_2^2 + \lambda_3^2 = \text{tr}(\mathbf{C}), \\ I_2 &= \lambda_1^2 \lambda_2^2 + \lambda_2^2 \lambda_3^2 + \lambda_3^2 \lambda_1^2 = \frac{1}{2}(I_1^2 - \text{tr}(\mathbf{C}^2)), \\ I_3 &= \lambda_1^2 \lambda_2^2 \lambda_3^2 = J^2 = \det(\mathbf{C}). \end{aligned} \quad (2.19)$$

The third invariant, I_3 , is a volumetric constant equal to 1 initially, since all three principal stretch ratios are equal to 1 when the strain is zero. In a similar fashion, the determinant of the right stretch tensor, \mathbf{U} , is equal to J ; i.e.,

$$J = \det(\mathbf{U}) = \lambda_1 \lambda_2 \lambda_3. \quad (2.20)$$

If the material is incompressible, J will always remain equal to 1, thus providing a useful relation between the principal stretch ratios:

$$J = \lambda_1 \lambda_2 \lambda_3 = 1. \quad (2.21)$$

Physically, the scalar value of J may be seen as a volumetric parameter defined as the infinitesimal volume, dV , divided by the infinitesimal reference volume, dV_o , such that

$$J = \frac{dV}{dV_o}. \quad (2.22)$$

2.2.3. Stress principles

Taking a point P in the plane of an element with normal n_j and traction vector t_i acting on point P , such as sketched in Fig. 12, the *Cauchy stress* is defined as

$$t_i = \sigma_{ji} n_j. \quad (2.23)$$

Due to its definition, the Cauchy stress implies that it represents the state of stress of a point in its current deformed state and is thus often referred to as the *true stress*. The FEA software ANSYS™ outputs true stresses when large strain simulations are performed.

Fictitious stresses based on the reference position of the body are often used in practice, though they may become quite meaningless to the true state of stress present in a body when large deformations are involved. It is often convenient to measure the engineering (a.k.a. first Piola-Kirchhoff, Lagrange or nominal) stress, defined in indicial form as

$$S_{ij} = J F_{ij}^{-1} \sigma_{ij}, \quad (2.24)$$

where J is the determinant of \mathbf{U} , such as defined in Eq.(2.20). In practice, and for simple states of stress, engineering stress is a measure of the applied force over the reference cross-section.

In the presence of infinitesimal displacements, the nuance between the Cauchy and engineering stress tensors is negligible and a first-order approximation reduces them to same expression.

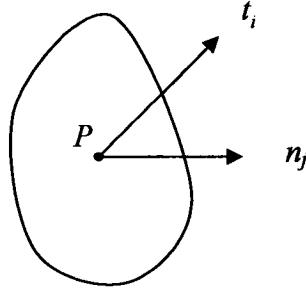


Fig. 12: Traction vector t_i acting on point P whose normal is n_i . This figure and caption are inspired from Mase and Mase (1999).

2.2.4. Strain-energy function

A constitutive material law is said to be *hyperelastic* if it is defined by a strain energy function. The strain energy function is originally derived from the 1st law of thermodynamics, expressed as

$$\frac{D}{Dt}(K + U) = P + Q, \quad (2.25)$$

where K is kinetic energy, U is internal energy, P is mechanical power, and Q is the rate at which thermal energy is added to the body. From Eq.(2.25), and following appropriate assumptions, an expression for the strain energy, W , may be derived. This derivation, which closely follows the work of Mase and Mase (1999), is presented in Appendix A. Assuming incompressibility, it is shown that the Cauchy stress tensor may be obtained from the strain energy via

$$\sigma_{ij} = J^{-1} F_{ip} \frac{\partial W}{\partial F_{jp}} - p \delta_{ij}, \quad (2.26)$$

where the scalar p is conveniently chosen to represent the hydrostatic pressure serving as the internal constraint due to the incompressible response of the material. Note that the Cauchy stress tensor is symmetric here; thus, $\sigma_{ij} = \sigma_{ji}$. Assuming a state of simple strain (i.e. with no rotations) and considering only the principal axes, Eq.(2.26) reduces to the familiar form found in most literature on hyperelasticity, which is

$$\sigma_i = \lambda_i S_i = \lambda_i \frac{\partial W}{\partial \lambda_i} - p. \quad (2.27)$$

Hyperelastic models are usually expressed as a function of the principal stretch ratios, λ_i , so that $W(\lambda_1, \lambda_2, \lambda_3)$; or as a function of the strain invariants, I_i , so that $W(I_1, I_2, I_3)$. And so, using the partial derivative chain rule, Eq.(2.27) may also be written as

$$\sigma_i = \lambda_i S_i = \lambda_i \left[\frac{\partial W}{\partial I_1} \frac{\partial I_1}{\partial \lambda_i} + \frac{\partial W}{\partial I_2} \frac{\partial I_2}{\partial \lambda_i} \right] - p. \quad (2.28)$$

2.3. Hyperelastic models

Treloar (1943) provided one of the first sound demonstrations on how to obtain a hyperelastic model by combining statistical thermodynamics to a one-dimensional theory of long chained molecules. The strain-energy density function he obtained is commonly known today as the Neo-Hookean model:

$$W = \frac{1}{2} \mu (I_1 - 3), \quad (2.29)$$

where μ is the initial shear modulus, although in the actual statistical mechanics derivation (e.g. Sears, 1955), $\mu = NkT$, where N is the number of chains of molecules per unit volume, k is the Boltzmann constant and T is the absolute temperature. While the Neo-Hookean model is acceptable to represent the geometric softening of rubber due to large deformations, it does not capture the sudden stiffening this particular material will exhibit just before breaking.

Few others have explored the statistical mechanics approach to modelling the elastic behaviour of rubber. Among the few, Arruda and Boyce (1993) derived a hyperelastic constitutive relation based on a three-dimensional array of long-chained molecules. Their work successfully captured the stiffening of rubber near its elongation limit although the model they have proposed is somewhat complicated.

Rivlin (1948a) proposed a phenomenologically based strain energy model for incompressible materials, commonly referred to (e.g. in ANSYS™) as the polynomial model, which takes the following form:

$$W = \sum_{i,j=1}^{\infty} C_{ij} (I_1 - 3)^i (I_2 - 3)^j. \quad (2.30)$$

The Neo-Hookean model can easily be obtained from Rivlin's formulation, such that

$$W = C_{10} (I_1 - 3),$$

taking $C_{10} = \frac{1}{2} \mu = \frac{1}{2} NkT$. Mooney's (1940) earlier work can also be expressed with Eq. (2.30), resulting in what is generally accepted today as the Mooney-Rivlin model, the first two terms of which are

$$W = C_{10} (I_1 - 3) + C_{01} (I_2 - 3). \quad (2.31)$$

Eq. (2.31) represents the first-order Mooney-Rivlin model. Three and five parameter Mooney-Rivlin models are defined as

$$W = C_{10} (I_1 - 3) + C_{01} (I_2 - 3) + C_{11} (I_1 - 3)(I_2 - 3), \quad (2.32)$$

$$W = C_{10} (I_1 - 3) + C_{01} (I_2 - 3) + C_{11} (I_1 - 3)(I_2 - 3) + C_{20} (I_1 - 3)^2 + C_{02} (I_2 - 3)^2, \quad (2.33)$$

respectively. The Mooney-Rivlin model has been proven in literature to be accurate, although mostly for unfilled rubber compounds (Yeoh, 1990).

The next popular hyperelastic model was proposed by Ogden (1972a, b). His work includes models for incompressible and slightly compressible materials. Ogden's approach is to some extent different, for it defines the strain energy directly as a function of the principal stretch ratios rather than the strain invariants; it is commonly known today as the Ogden hyperelastic model under the following form:

$$W = \sum_{i=1}^n \frac{\mu_i}{\alpha_i} (\lambda_1^{\alpha_i} + \lambda_2^{\alpha_i} + \lambda_3^{\alpha_i} - 3) + \sum_{k=1}^n \frac{1}{d_k} (J - 1)^{2k}, \quad (2.34)$$

where n determines the number of terms in the expression and d_k represents a compressibility factor. A modified stretch ratio is introduced as well, λ_i^* , defined as

$$\lambda_i^* = J^{-\frac{1}{3}} \lambda_i, \quad (2.35)$$

such that the modified volumetric ratio, J^* , remains incompressible, i.e.:

$$J^* = \lambda_1^* \lambda_2^* \lambda_3^* = \left(J^{-\frac{1}{3}} \lambda_1\right) \left(J^{-\frac{1}{3}} \lambda_2\right) \left(J^{-\frac{1}{3}} \lambda_3\right) = J^{-1} J = 1. \quad (2.36)$$

As mentioned before, when a material is assumed incompressible, the volumetric parameter J is equal to 1 and hence the second summation on the right-hand side of Eq.(2.34) becomes zero. Similarly, $\lambda_i^* = \lambda_i$ and Ogden's special formulation for a slightly compressible material reduces to a familiar form. The modified stretch ratio, λ_i^* , is a linear approximation that only applies if the material is slightly compressible, i.e. with a Poisson ratio between 0.49 and 0.5. Modified strain invariants, I_i^* , may also be defined from the modified stretch ratios and thus all the hyperelastic models mentioned in this section may be modified to accommodate a slightly compressible material with an additional compressibility term similar to the second term on the right hand side of Eq.(2.34).

One may notice that taking $n = 1$, $\alpha_1 = 2$, and $\mu_1 = NkT$ from Eq.(2.34) leads to the Neo-Hookean model. Furthermore, taking $n = 2$, $\alpha_1 = 2$, $\mu_1 = 2C_{10}$, $\alpha_2 = -2$, $\mu_2 = 2C_{01}$ again from Ogden's formulation [and substituting Eq.(2.21) into the first invariant of Eq.(2.19)] leads to the first-order Mooney-Rivlin model [Eq.(2.31)].

Yeoh (1990) suggested yet another model, which can be derived from Rivlin's (1948a) generic formulation, under the false assumption [later discussed in Yeoh (1996)] that the second strain invariant, I_2 , is constant with stretch and thus does not contribute to the strain energy density:

$$W = \sum_{i=1}^N C_{i0} (I_1 - 3)^i, \quad (2.37)$$

where N determines the order of the model. This model nonetheless successfully handles filled rubber to a certain degree of accuracy and is said to only need equi-biaxial characterisation data for an acceptable fit.

The Neo-Hookean model can be presented once again in a different format, as done by Gent (1996), namely

$$W = \frac{E}{6} (I_1 - 3), \quad (2.38)$$

where E represents the tensile modulus at small strains. Comparing Eq.(2.38) to Eq.(2.29) one may notice the linear relationship defined by Hooke's law between tensile and shear modulus if the Poisson ratio is taken to be 0.5 (incompressible). Gent (1996) also proposes a constitutive formulation for the strain energy density, this time, by introducing a constant, J_m , defined as the maximum strain to which a molecular network can stretch:

$$W = -\frac{E}{6} J_m \ln \left(1 - \frac{I_1 - 3}{J_m} \right). \quad (2.39)$$

This expression introduces a singularity when $I_1 - 3 = J_m$, which successfully succeeds in representing the stiffening of rubber near ultimate elongation. Gent's formulation may also be seen as empirical, since it is assumed to be independent of molecular length.

The expressions for stress in uniaxial tension as well as the initial tensile modulus of these hyperelastic models are given in Table 1.

Table 1: Table showing the expression for engineering stress, S_1 , as a function of the stretch ratio, λ_1 , for the uniaxial tension case ($\lambda_1 = \lambda$, $\lambda_2 = \lambda_3 = \lambda^{-1/2}$, $\sigma_1 = \sigma$, $\sigma_2 = \sigma_3 = 0$)

	Engineering stress, $S_1 = \frac{\sigma_1}{\lambda_1}$	Initial tensile modulus
Neo-Hookean	$2\left(\frac{1}{2}\mu\right)(\lambda_1 - \lambda_1^{-2})$	$6\left(\frac{1}{2}\mu\right)$
Mooney-Rivlin	$(2C_{10} + 2C_{01}\lambda_1^{-1})(\lambda_1 - \lambda_1^{-2})$	$6(C_{10} + C_{01})$
Ogden	$\sum_{i=1}^n \mu_i \left(\lambda_1^{\alpha_i-1} - \lambda_1^{-\frac{1}{2}\alpha_i-1} \right)$	$\frac{3}{2} \sum_{i=1}^n \mu_i \alpha_i$
Yeoh	$2(\lambda_1 - \lambda_1^{-2}) \left[\sum_{i=1}^N C_{i0} i (I_1 - 3)^{i-1} \right]$	$6C_{10}$
Gent	$2\mu(\lambda_1 - \lambda_1^{-2})(J_m - (I_1 - 3))^{-1}$	$6\mu J_m^{-1}$

Chapter 3: Material Characterisation

Standard characterisation tests have been developed to measure the stress-strain response of rubber under states of simple stress. It is generally desirable to characterise the material in tension, in compression and in shear. Due to the incompressibility of rubber, certain states of simple stress are equivalent to each other. For example, a state of uniaxial tension is equivalent to a state of equi-biaxial compression. As illustrated in Fig. 13, the equivalence may be visualised by adding a hydrostatic compression to the state of uniaxial tension. Note that hydrostatic compression has no effect on the state of strain due to the rubber's incompressibility. The traditional dog-boned uniaxial tension test is probably the most popular and widely used characterisation test, mainly for its simplicity.

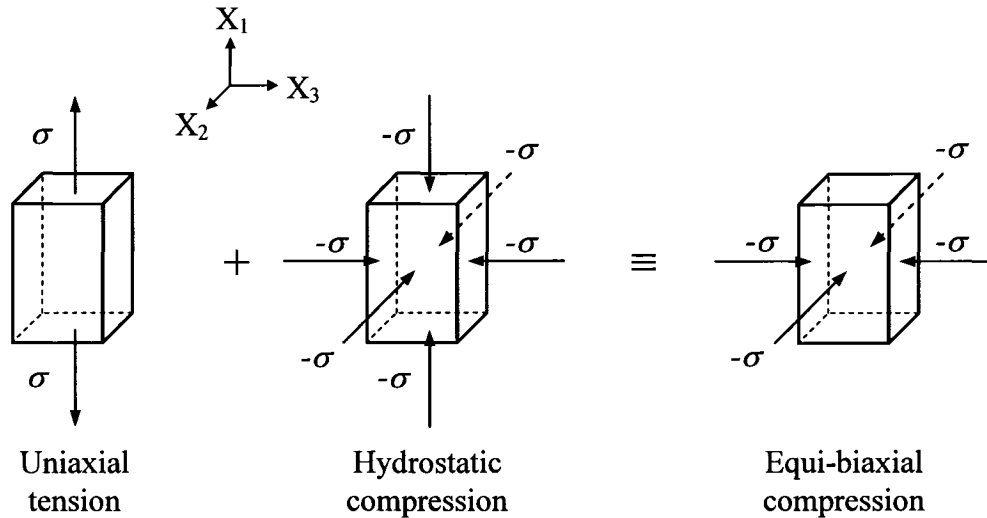


Fig. 13: Schematic representation demonstrating the equivalence between uniaxial tension and equi-biaxial compression ($\lambda_1 = \lambda$, $\lambda_2 = \lambda_3 = \lambda^{-1/2}$).

It is possible to characterise rubber in uniaxial compression by squeezing a cylindrical specimen between two platens, as described by Lobo and Bethard (2006). In order to maintain a state of uniaxial compression, there should be no friction between the platen and the rubber specimen; lubricants may be used to reduce this friction effect. Equi-biaxial extension, under the assumption of incompressibility, is a state of stress considered equivalent to uniaxial compression, as illustrated in Fig. 14. Although the equi-biaxial tension test is generally more expensive to perform (it requires more

equipment), when executed properly, it may be considered more accurate than a uniaxial compression test since there is no interference from such effects as friction.

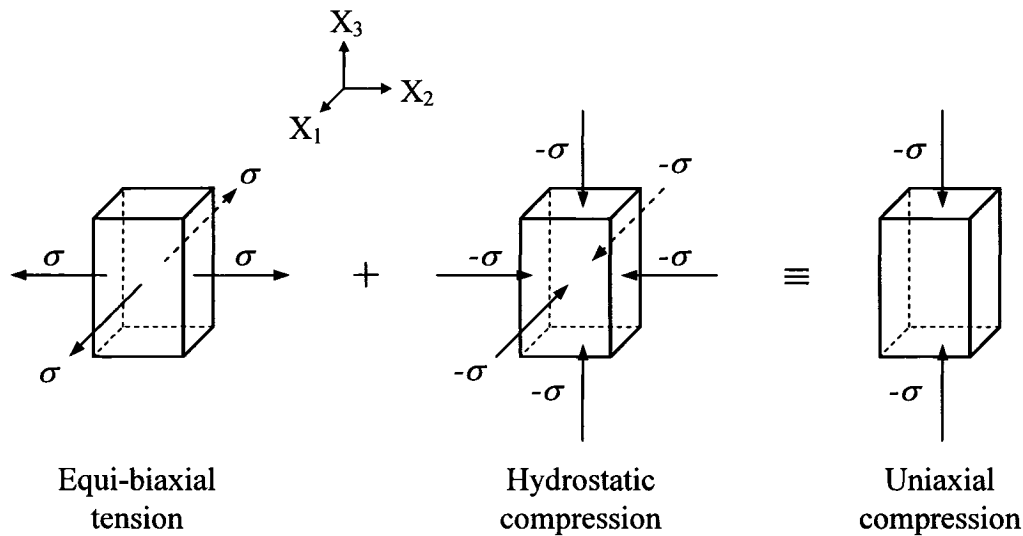


Fig. 14: Schematic representation demonstrating the equivalence between equi-biaxial extension and uniaxial compression ($\lambda_1 = \lambda_2 = \lambda$, $\lambda_3 = \lambda^{-2}$).

Again thanks to incompressibility, it can be shown, as done in Fig. 15, that a state of planar tension ($\lambda_2 = 1$, i.e. no deformations in the X_2 direction) may be equivalent to a state of pure shear. Rubber can therefore be tested in planar tension in order to obtain its behaviour in pure shear.

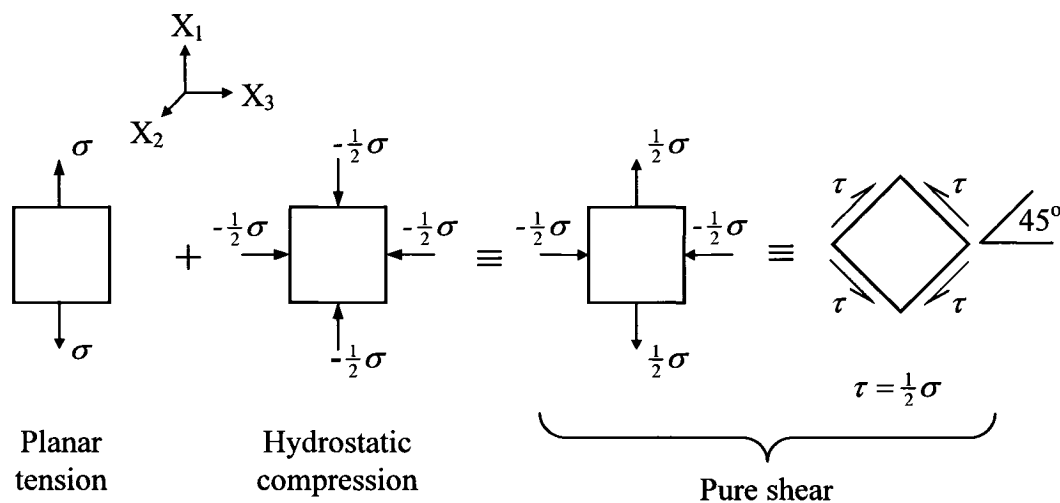


Fig. 15: Schematic representation demonstrating the equivalence between a state of planar tension test and a state of pure shear ($\lambda_1 = \lambda$, $\lambda_2 = 1$, $\lambda_3 = \lambda^{-1}$).

These states of stress (Figs. 13, 14 and 15) are said to be simple, in view of the fact that each state has a single independent variable, λ . The stretch ratios with respect to λ in all principal directions can be determined with Eq.(2.21).

The material used in this thesis, a hard carbon-black-filled rubber, was characterised by Axel Products Inc. in uniaxial tension, equi-biaxial extension and planar tension. The following section provides a description of how the data was obtained and how it is manipulated. The data is then fitted to hyperelastic models with curve-fitting tools available in ANSYS™.

3.1. Experimental procedure

The general procedure followed by Axel Products Inc. to achieve the three aforementioned states of simple stress is fundamentally the same. The testpieces are cut out of a 150x150 mm slab of rubber that is 1-2 mm thick. The loading is performed at a quasi-static strain rate of 0.01 s^{-1} ; this rate has been chosen to minimize thermal effects due to internal heat generation. Engineering stress is measured by dividing the applied load by the cross-section respective to the test being conducted. The strain measured is in the direction of the load, also respective to the test being conducted. Each sample is first loaded to 5% nominal (engineering) strain, then completely unloaded. This cycle is repeated 9 more times in order to precondition the testpiece. By the 10th cycle, the sample has stabilised and is considered to be preconditioned for 5% maximum strain. The same procedure is repeated on the same specimen for nominal strains of 10%, 15% and 25%. Three samples were tested in each state of simple stress. A sample of the collected nominal stress-strain data for a testpiece in uniaxial tension is given in Fig. 16. Note how this figure reproduces the combined behaviour shown in Figs. 6 and 8 of Section 2.1.

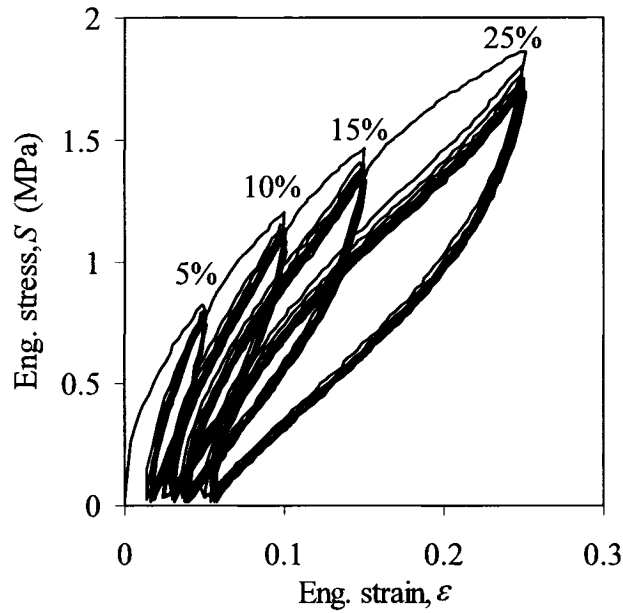


Fig. 16: Original data for the uniaxial tension test showing preconditioning at four different levels of strain: 5%, 10%, 15% and 25% nominal strain.

The last cycle for each maximum nominal strain, i.e. the 10th, 20th, 30th and 40th loading cycles, corresponds to a stabilized path for the respective 5%, 10%, 15% and 25% maximum nominal strains. These four preconditioned loading curves are clearly shown in Fig. 17 for the uniaxial tension test, in Fig. 18 for the planar tension test, and finally in Fig. 19 for the equi-biaxial extension test. Note in these figures that the stress is plotted as a function of the principal stretch measured in the direction of the load applied respective to the state of stress. Also note that the virgin stretch curve is exact up to 5% nominal strain; it is then approximated to the maximum stress-strain data point for each subsequent stretch cycles. For the virgin stretch path to be exact, a separate testpiece should be stretched up to the desired strain. Based on Figs. 5 and 6, one could expect the virgin stretch curve of Figs. 17, 18 and 19 to be slightly above the data for the 10%, 15% and 25% nominal strain cycles.

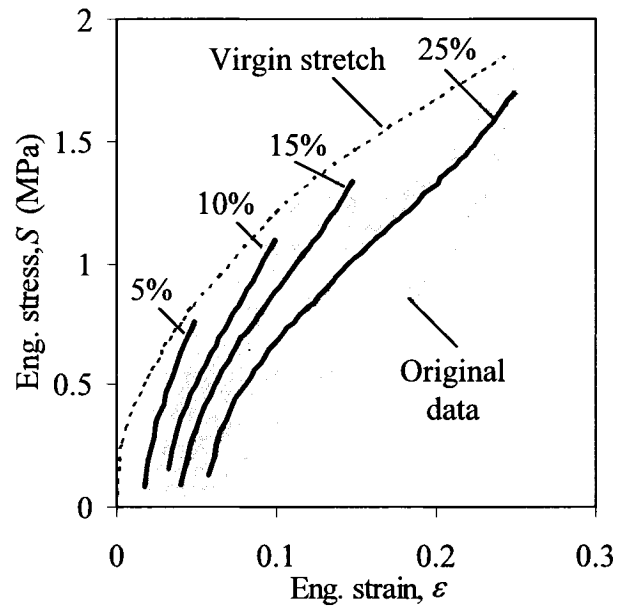


Fig. 17: The preconditioned loading cycles (dark continuous lines) extracted from the original data (grey lines) in uniaxial tension.

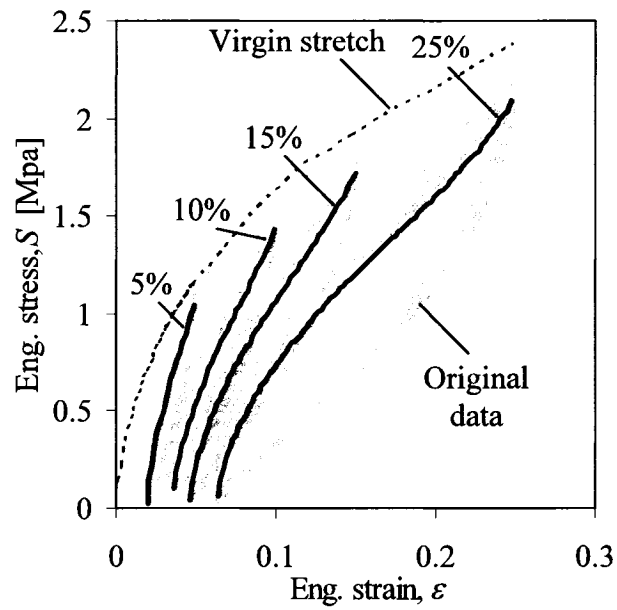


Fig. 18: The preconditioned loading cycles (dark full lines) extracted from the original data (grey lines) in planar tension.

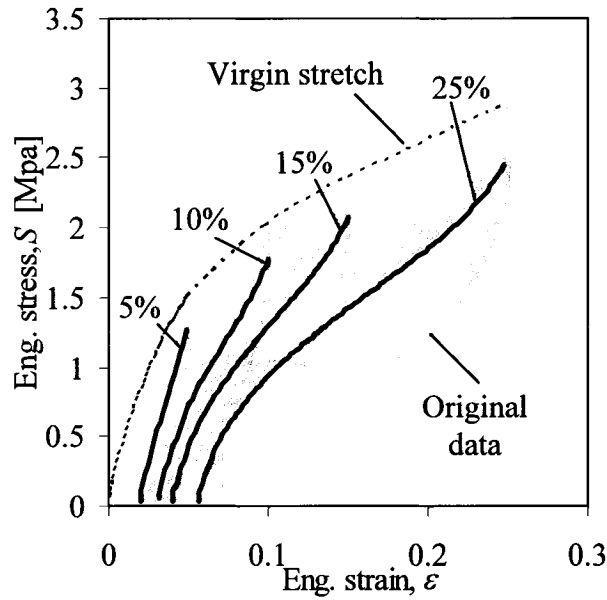


Fig. 19: The preconditioned loading cycles (dark continuous lines) extracted from the original data (grey lines) in equi-biaxial extension.

These stabilised loading paths show considerable unrecoverable strain when stress-free. Since purely elastic behaviour will be assumed, the preconditioned stress-strain curves are manipulated to eliminate the offset strain as follows. The offset strain for each preconditioned curve, ϵ_{offset} , is subtracted and all strain values are divided by $(\epsilon_{\text{offset}} + 1)$ to account for the larger stabilized gauge length. Similarly, all the stress values are multiplied by $(\epsilon_{\text{offset}} + 1)$ to account for the stabilized gauge cross-sectional area. Refer to Appendix B for a detailed description of the manipulation of stress and strain data. Following this operation, the usually small offset stress value is subtracted from the rest of the stress values in order to have zero stress at zero strain. Fig. 20 shows the four manipulated stress-strain curves for 5%, 10%, 15% and 25% nominal strain with the original virgin stretch of the uniaxial test data.

Finally, the number of data points is evenly reduced in order to provide an easily manageable file for the curve-fitting tool. The manipulated stress-strain characterisation data points are provided in Appendix C, for uniaxial tension, biaxial extension and planar tension.

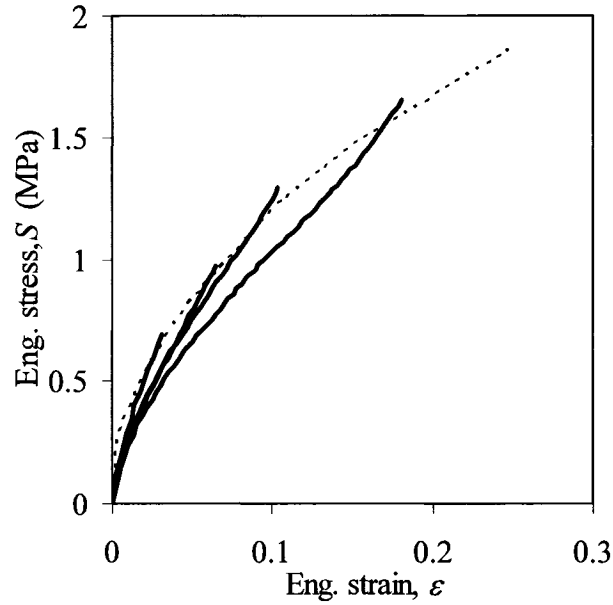


Fig. 20: Preconditioned curves, manipulated to eliminate the offset strain, for the uniaxial tension test.

The strain range characterised (0-25% engineering strain) is considered to be moderate with respect to the strain capacity of the rubber at hand. The stress-strain relationship of the material in uniaxial tension is illustrated in Fig. 21 for strain up to ~150%, clearly showing that the 0-25% range of strain is relatively small.

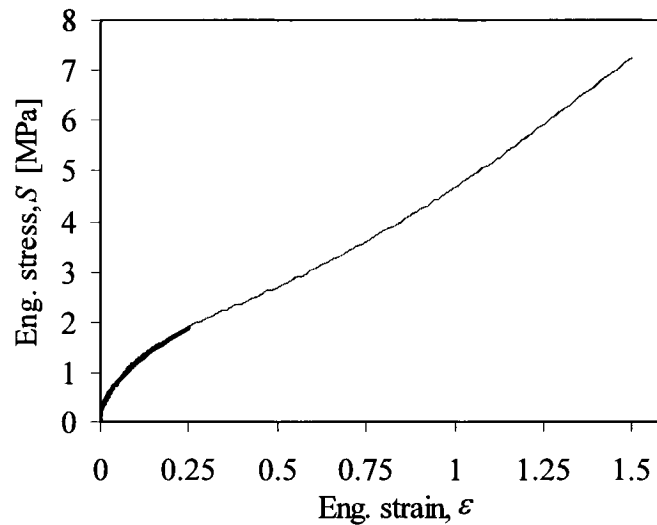


Fig. 21: Stress-strain response of rubber at hand up to ~150% engineering strain (grey line). The strain range of interest in this thesis is relatively moderate (black line)

3.1.1. Uniaxial tension test

The rubber specimen used in uniaxial tension is typically a bone-shaped specimen, usually cut out of a thin, 1-2 mm thick, sheet of rubber. The specimen's total length is around 115 mm, while the "test-section" is around 33 mm long. The test-section must have a larger length than its width and its thickness so that the deformations along the length may be assumed uniform. The "bone ends" of the specimen are about 25 mm wide, while the thinner "test-section" is approximately 6 mm wide. These dimensions can vary; what is important, though, is that the width and thickness of the specimen must thin evenly over the length of the test-section. The wider "bone ends" of the specimen are clamped in a stretch machine. Engineering stress is calculated by dividing the measured load by the initial gage cross-sectional area. Engineering strain is recorded with an optical strain gauge. A photograph of the experimental set-up for uniaxial tension is provided in Fig. 22. A quarter of the testpiece geometry from a FEA model is shown in Fig. 23 where the contours of the maximum principal strain, ε_1 , indicate uniform strain in the test-section.

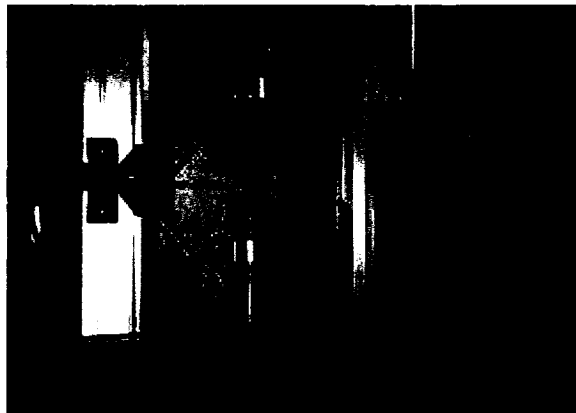


Fig. 22: Picture of the uniaxial tension test set-up, courtesy of Axel Products Inc.

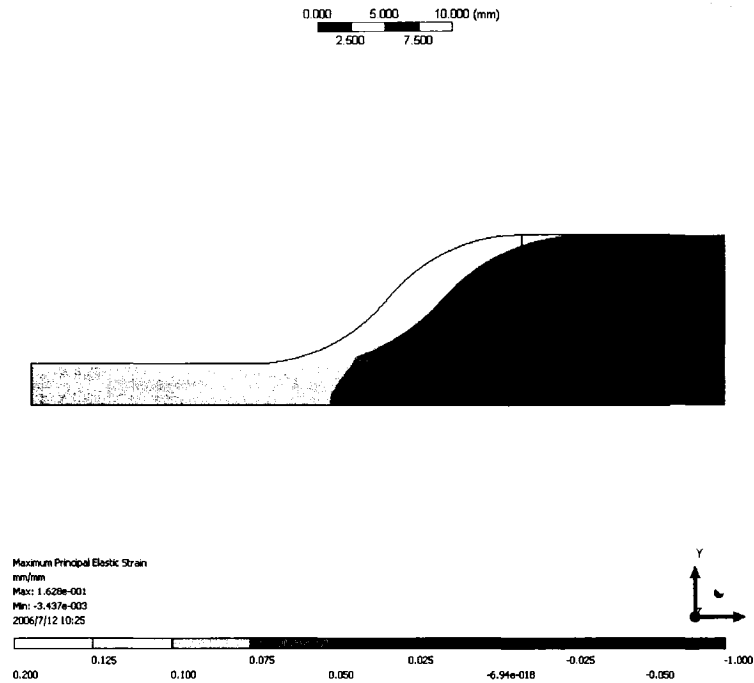


Fig. 23: Quarter model of a FEA simulation of the uniaxial tension test showing contours of the maximum principal strain, ϵ_1 .

3.1.2. Equi-biaxial extension test

A circular disc of 75 mm in diameter is cut out of a thin, 1-2 mm thick, sheet of rubber for the equi-biaxial extension test; 16 holes, 5 mm in diameter, are then cut, evenly distributed, around the disc, with a distance of 27.5 mm from the centre of the small holes to the centre of the disc. A radial slit is cut from the outside of the disc to each small hole such that sixteen tabs are created. These tabs are clamped on a special machine and stretched radially. The holes are there to prevent stress concentrations in the testpiece. Again, the given dimensional parameters can be varied as long as the thinning of the specimen is even over the measured section. The radial load must also be assumed evenly distributed around the circumference of the test-section. Radial engineering stress and radial engineering strain are measured. A photograph of the experimental set-up for equi-biaxial extension is provided in Fig. 24. One sixteenth of the testpiece geometry from a FEA model is shown in Fig. 25 where the contours of the maximum principal strain, ϵ_1 , indicate uniform distribution of radial strain, even though the load is applied at sixteen locations.

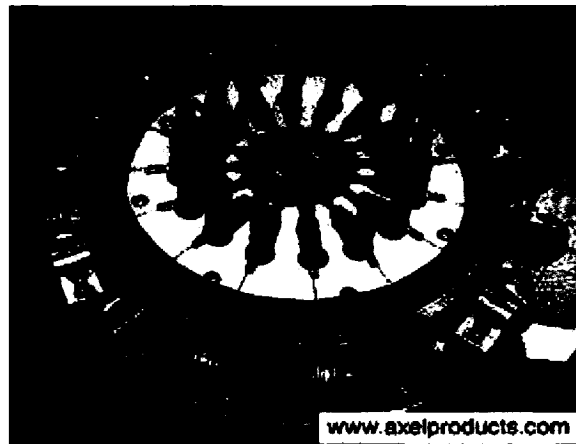


Fig. 24: Equal-biaxial tension test, courtesy of Axel Products Inc.

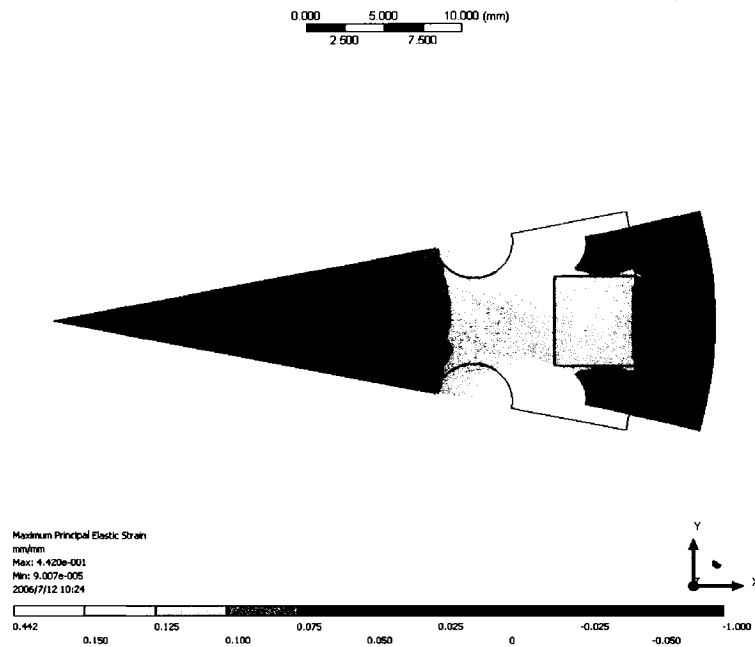


Fig. 25: FEA model showing one sixteenth of the equi-biaxial extension testpiece, the contours are of the maximum principal strain, ϵ_1 .

3.1.3. Planar tension test

A rectangular specimen is cut out of a 1-2 mm thick sheet of rubber. The specimen is clamped such that the free length (in the stretching direction) is much smaller than the width, so that the thinning occurs only in the thickness direction. A testpiece of 150 mm in width and 50 mm in length leaving 20 mm for the test-section (30 mm clamped) would

be an appropriate geometry. A picture of the experimental set-up for planar tension is provided in Fig. 26, while a quarter model of the FEA simulation is given in Fig. 27 where the contours of middle principal strain, ϵ_2 , show no deformation in the width direction, other than negligible end effects. It is emphasised that the stretch along the width of the test-section must be negligible for the results to be equivalent to pure shear, as described in Fig. 15.



Fig. 26: Planar tension test, courtesy of Axel Products Inc.

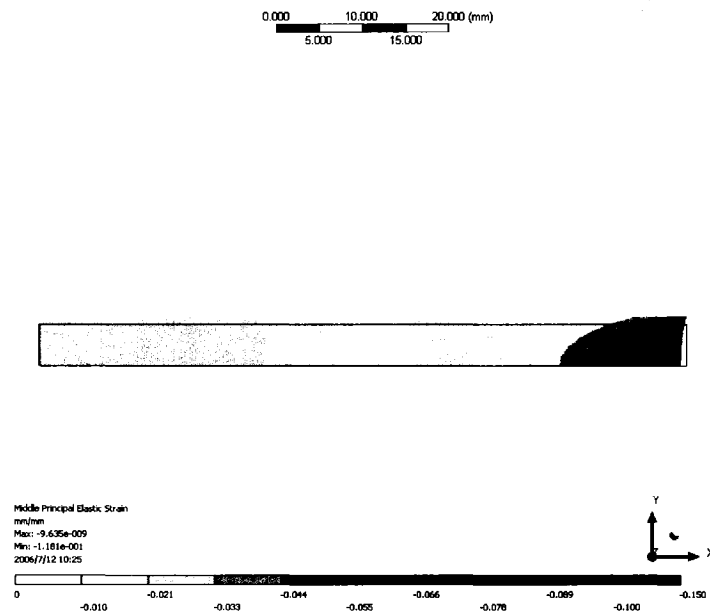


Fig. 27: Quarter FEA model of the planar tension test showing contours of the middle principal strain, ϵ_2 .

3.2. Curve-fitting

Just like “Young’s modulus” in linear elasticity is said to be a material property, the coefficients of a given hyperelastic model will also become, in some way, the material properties defining a rubber-like material. These coefficients are not measured directly but rather fitted to experimental characterisation data, such as the data described in Section 3.1. The discussion herein revolves around curve-fitting hyperelastic models to preconditioned characterisation data. The validity and limitations of doing so must also be discussed.

The procedure for fitting a hyperelastic model to characterisation data is similar in ANSYSTM Workbench 10.0 and classical ANSYSTM 10.0 interfaces; while more control is given in the classical version, Workbench is more convenient. One may notice that control over convenience is often what differentiates ANSYSTM classic from ANSYSTM Workbench. For example, ANSYSTM Workbench provides no control over the number of iterations performed or the truncation error during nonlinear curve-fitting, whereas ANSYSTM classic does. In either interface, all available hyperelastic models can be fitted to uniaxial tension data alone, to planar tension data alone[§], to equi-biaxial extension data alone, any combination of two of these states of stress or to all three states of stress simultaneously.

In the context of this project, the characterisation data is preconditioned to different levels of strain, so it is preferable to remain consistent to one level of preconditioning when fitting a hyperelastic model to multiple states of simple stress simultaneously. The curve-fitting module generates coefficients for the selected hyperelastic model. Graphical tools are available to visually compare the selected hyperelastic model predictions in the three states of simple stress to the characterisation data used in the curve-fitting.

[§] The Neo-Hookean model cannot be fitted to planar tension data alone (yet the first-order Yeoh model, which is exactly equivalent to the Neo-Hookean model, can be fitted to planar tension data).

Care must be taken when fitting characterisation data to hyperelastic models. Since the coefficients in the strain energy functions may be viewed as material constants, they have a certain physical meaning. This physical meaning is not considered by the curve-fitting tool which only concentrates on obtaining the best mathematical fit to the given data.

Certain hyperelastic models such as the Neo-Hookean, the Mooney-Rivlin and the Yeoh formulations of strain energy use linear curve-fitting methods, and their coefficients are obtained instantly. On the other hand, the Ogden and the Gent models rely on an iterative nonlinear curve-fitting method. For this reason and also due to the several coefficients involved, the adequate fitting of the Ogden model is highly dependent on the initial values proposed before the curve-fitting begins. Both linear and nonlinear curve-fitting methods rely on a least-squares minimisation function.

The (absolute) least squares method consists of fitting an equation to a set of data, such that the following least squares residual error function, E , is minimized:

$$E = \sum_{k=1}^m \left[S_m - \hat{S}(\lambda_m) \right]^2, \quad (3.1)$$

where, in the context of this work, S_m is the experimental value of stress at strain $\varepsilon_m = 1 - \lambda_m$, $\hat{S}(\lambda_m)$ is the stress predicted from the fitted hyperelastic model, also at strain $\varepsilon_m = 1 - \lambda_m$, and m is the number of data points considered in the curve-fit. This method is often preferred over other methods since it gives “[substantial] weight [to a data] point that is out of line with the rest of the data but will not allow that point to completely dominate the approximation.”** For further discussion on the method of least squares, refer to Burden and Faires (2001).

The least squares method can be normalised to obtain the normalised least squares residual error function, E_N , such that

$$E_N = \sum_{k=1}^m \frac{\left[S_m - \hat{S}(\lambda_m) \right]^2}{S_m^2}. \quad (3.2)$$

** Burden and Faires (2001), p.486.

In both interfaces (classic and Workbench), when performing a nonlinear curve-fit it is possible to choose between a normalised (E_N) or absolute (E) error norm. The normalised error norm treats all data points equally, whereas the absolute error norm gives more weight to the higher stress data points. In this work, the normalised error norm will be applied for the curve-fitting.

The normalised root-mean-squared error, E_{NR} , similar to what is known as the root-mean-squared error^{††}, may be used to obtain a more physical measure of mean residual error:

$$E_{NR} = \frac{\sqrt{E_N}}{v}, \quad (3.3)$$

where v is the number of data points used, m , minus the number of coefficients used in the hyperelastic model, n , such that

$$v = m - n. \quad (3.4)$$

The normalised root-mean-squared error, E_{NR} , can be used to evaluate the goodness of fit of a hyperelastic model with respect to the data being fitted. It can also be used to compare the goodness of fit with respect to other hyperelastic models fitted to other data. A value of E_{NR} closer to 0 indicates that the hyperelastic model has a better chance to predict the fitted data.

Please refer to Appendix D for a short demonstration on how to use the curve-fitting tool available in ANSYS™ Workbench 10.0.

3.2.1. General curve-fitting procedure in ANSYS™

In the following example, the uniaxial characterisation data preconditioned to 25% engineering strain is imported in ANSYS™ Workbench and fitted to a three parameter Mooney-Rivlin model. The resulting fit is shown in Fig. 28. It is clear from this figure that, although the model prediction in uniaxial tension fits the data quite well, the model predictions for planar tension have no physical meaning. Furthermore, knowing the qualitative behaviour of the rubber in equi-biaxial tension from Section 3.1, it is unlikely

^{††} <http://www.mathworks.com>, June 2006.

that this model provides an accurate prediction for the equi-biaxial data either. Note that the stresses are shown as a function of the principal strain in the direction of load respective to the state of stress.

The planar and equi-biaxial characterisation data, also preconditioned to 25% are imported into ANSYS™ in conjunction with the already imported uniaxial data. The three parameter Mooney-Rivlin hyperelastic model is then refitted, but this time to all three characterisation curves. The resulting fit is shown in Fig. 29. It is seen in this figure that the model no longer offers an accurate prediction for any of the characterisation curves. While the loss of physical meaning in this fit is less obvious, it is nonetheless clear that the characterisation curve for planar data never crosses the equi-biaxial data, while these curves do cross according to the model predictions. In either case, the Mooney-Rivlin model does not seem to provide physically meaningful fit to the hyperelastic data.

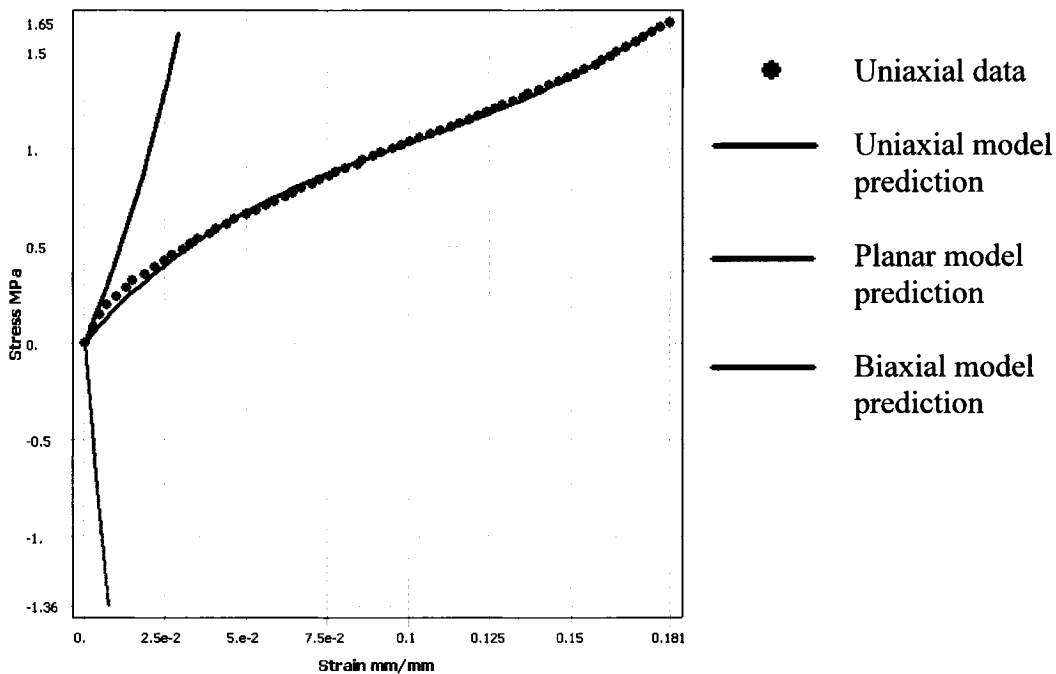


Fig. 28: Mooney-Rivlin model with three parameters fitted to the uniaxial tension data preconditioned to 25% strain; $C_{10} = -19.969$ MPa, $C_{01} = 23.257$ MPa and $C_{11} = 13.536$ MPa.

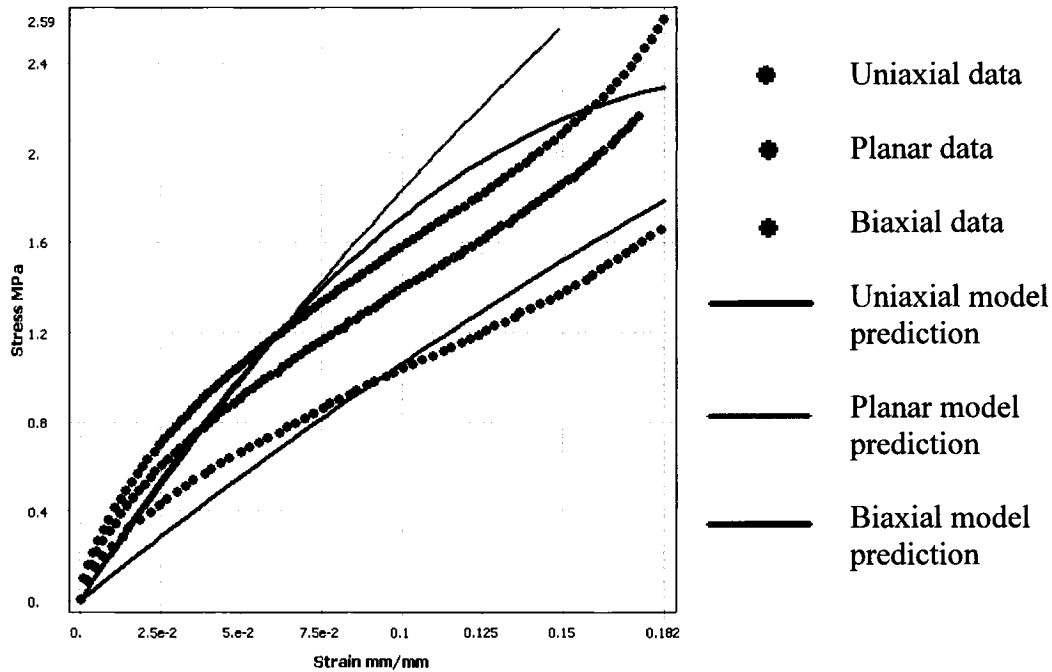


Fig. 29: Mooney-Rivlin model with three parameters fitted to the data preconditioned to 25% strain in all three states of simple stress simultaneously; $C_{10} = 2.2011$ MPa, $C_{01} = -0.27146$ MPa and $C_{11} = -0.36157$ MPa.

A similar procedure is undertaken here with a third-order Ogden model, first fitted only to the uniaxial characterisation data preconditioned to 25%, with the resulting fit shown in Fig. 30. Here the lack of control over the nonlinear curve-fitting process in Workbench greatly limits the quality of the curve fit; therefore the curve-fitting was done in ANSYSTM classic. The chosen initial conditions were: $\mu_1 = 100$ MPa, $\alpha_1 = 1$, $\mu_2 = 1$ MPa, $\alpha_2 = 4$, $\mu_3 = -1$ MPa and $\alpha_3 = -1$. These initial conditions, provided in the Advanced Structural Nonlinearities ANSYS training manual (2004), seem to generally work very well when curve-fitting the third-order Ogden to a single state of simple strain in ANSYSTM classic. Note that if initial conditions are not given when curve-fitting with a higher-order (second-order and up) Ogden model, the coefficients generated by the software will be equal ($\alpha_1 = \alpha_2 = \dots = \alpha_n = \alpha$ and $\mu_1 = \mu_2 = \dots = \mu_n = \mu$), such that the

resulting model will be equivalent to a first-order Ogden model ($\alpha_{equiv} = \sum_{i=1}^n \alpha_i = n\alpha$ and

$$\mu_{equiv} = \sum_{i=1}^n \mu_i = n\mu).$$

The model is then fitted to all three simple states of strain curves preconditioned to 25%, with the corresponding fit given in Fig. 31. It is clear from Fig. 30 that while the model prediction in uniaxial tension fits the corresponding characterisation curve the model predictions in planar and equi-biaxial tension do not (see Fig. 31 for the test data). On the other hand, fitting the third-order Ogden model to all three states of simple strain, as shown in Fig. 31 may have lost accuracy but remains close to the corresponding characterisation data.

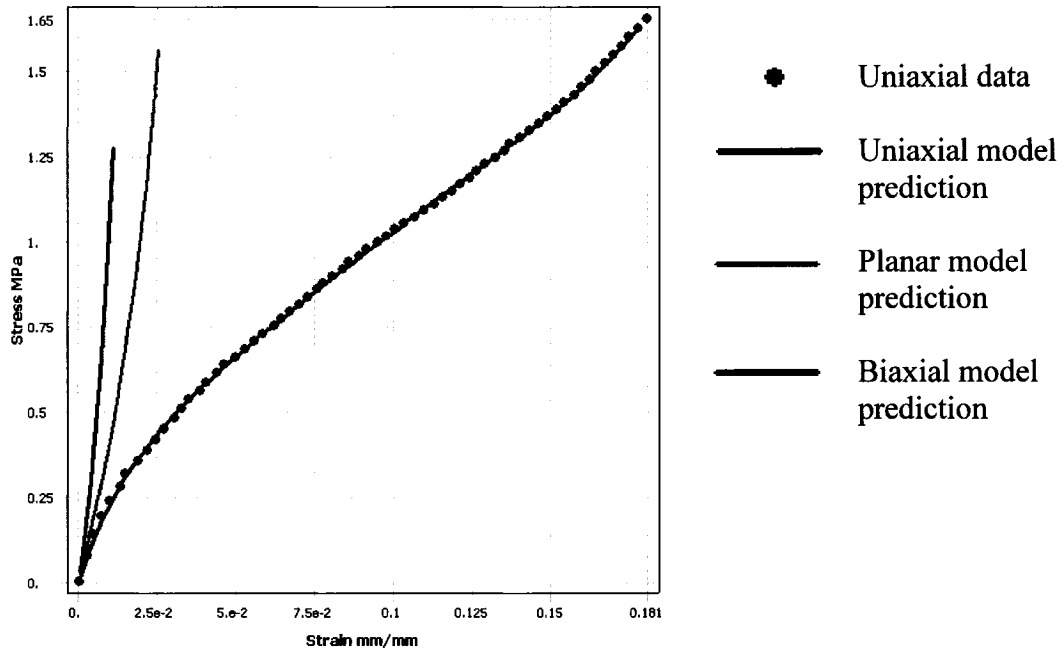


Fig. 30: Third-order Ogden model fitted to uniaxial tension data preconditioned to 25% strain; $\mu_1 = 196.78$ MPa, $\alpha_1 = 3.9680e-2$, $\mu_2 = -0.34627$ MPa, $\alpha_2 = -69.277$, $\mu_3 = -0.35077$ MPa and $\alpha_3 = 34.561$.

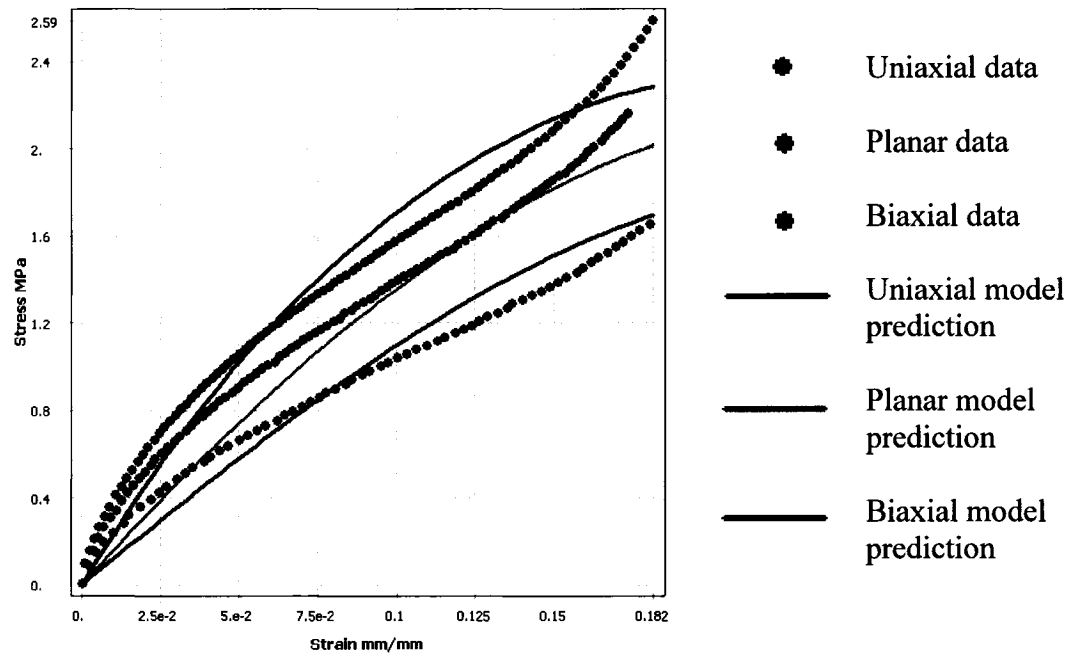


Fig. 31: Third-order Ogden model fitted to data preconditioned to 25% strain in all three states of simple stress simultaneously; $\mu_1 = 99.319$ MPa, $\alpha_1 = -1.2080e-2$, $\mu_2 = 18.853$ MPa, $\alpha_2 = 7.4442$, $\mu_3 = -16.875$ MPa and $\alpha_3 = 7.7678$.

The first-order Yeoh hyperelastic model (equivalent to the Neo-Hookean model) is fitted to the uniaxial tension data, then to the planar tension data and finally to the equi-biaxial tension data, all preconditioned to 25% engineering strain, in Fig. 32(a), Fig. 32(b) and Fig. 32(c), respectively. The procedure is repeated for the third-order Yeoh hyperelastic model in Fig. 33. Note that the characterisation data for all states of stress is shown in all figures for comparative purposes and that only one state of stress is used in the curve-fitting per figure.

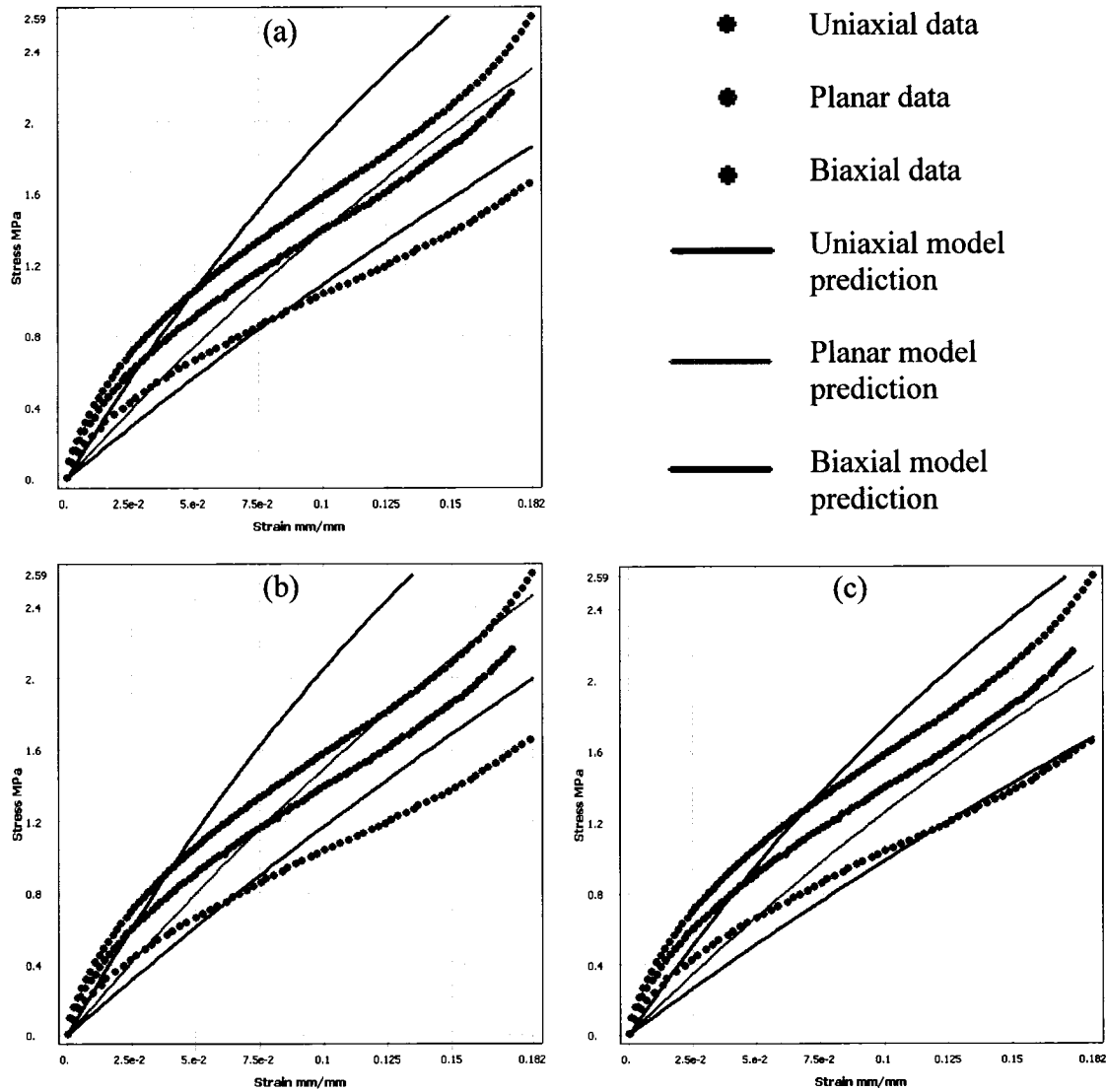


Fig. 32: First-order Yeoh hyperelastic model fitted to characterisation data preconditioned to 25% engineering strain in (a) uniaxial tension, (b) planar tension and (c) equi-biaxial extension. The coefficients are given in Table 2.

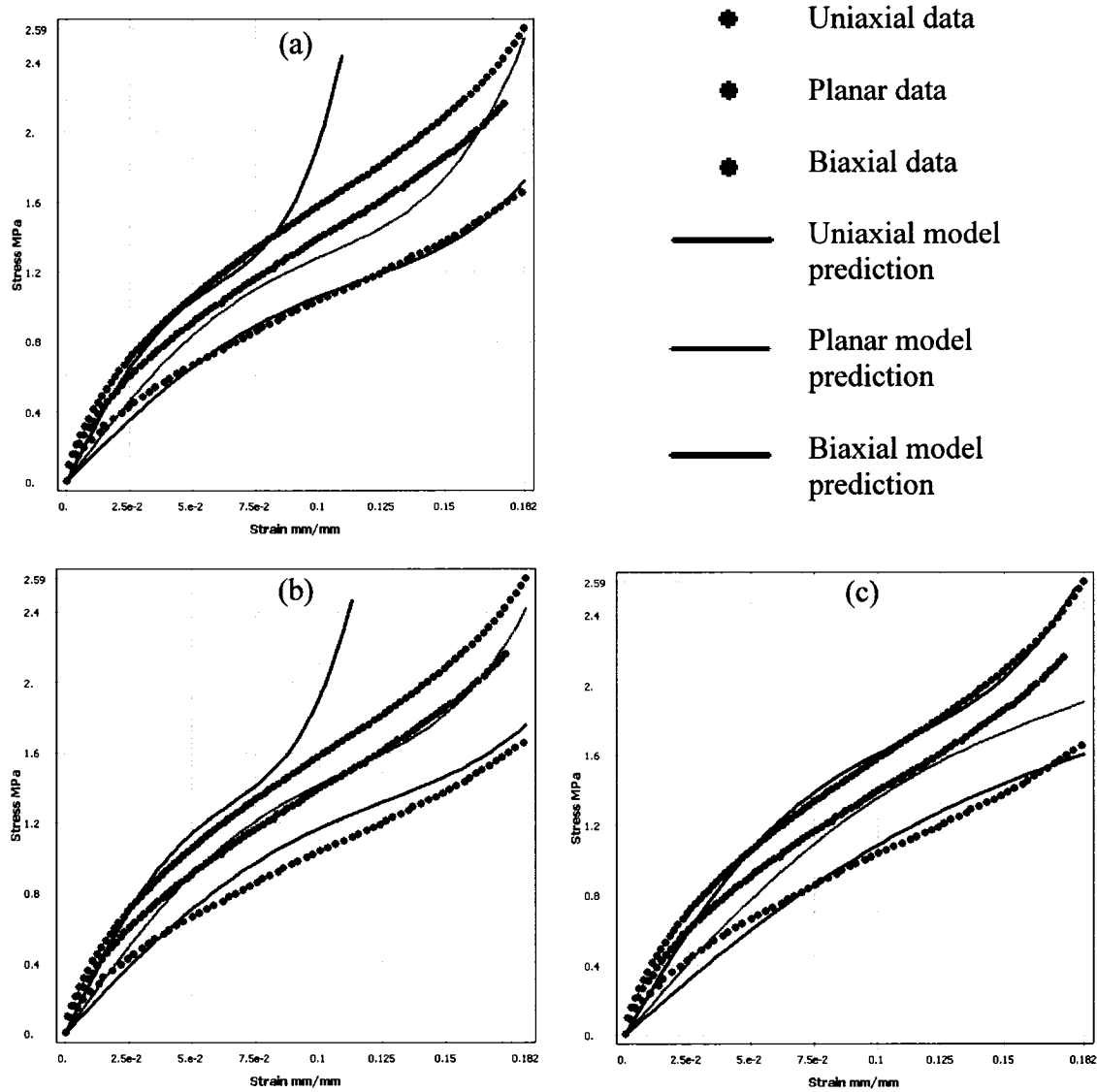


Fig. 33: Third-order Yeoh hyperelastic model fitted to characterisation data preconditioned to 25% engineering strain in (a) uniaxial tension, (b) planar tension and (c) equi-biaxial extension. The coefficients are given in Table 3.

The coefficients for the first-order Yeoh hyperelastic model fitted to the uniaxial tension data, then to the planar tension data and finally to the equi-biaxial tension data, for each level of preconditioning, are provided in Table 2 with corresponding normalised root-mean-squared error, E_{NR} , as defined in Eq.(3.3). Third-order Yeoh coefficients similarly obtained are given in Table 3, also with their corresponding normalised root-mean-squared error, E_{NR} . It can be shown that fitting the first- or third- order Yeoh model to all three states of simple strain, or any combination of two of these states of simple strain, at

the same time does not improve the fit. Furthermore, fitting a hyperelastic model to a single characterisation test may greatly reduce characterisation costs (as opposed to fitting a model to the three characterisation tests).

For these reasons and others discussed in the next section, the first- and third-order Yeoh models presented in Table 2 and Table 3 will be those of choice for the FEA simulations to come. Note that the normalised root-mean-squared errors given in these tables were calculated with respect to the data points used for curve fitting only. For example, the error of 2% given in Table 3 for the third order Yeoh hyperelastic model fitted to the uniaxial characterisation data preconditioned to 25% corresponds to the error between predicted and measured data in uniaxial tension only. Thus, the error between the predictions and measured data for this model in planar and equi-biaxial tension, shown in Fig. 33(a), is not accounted for. The first-order Yeoh hyperelastic model was preferred to the Neo-Hookean one in this case, since the curve-fitting tools in ANSYSTM (versions 9.0 and 10.0) do not allow fitting the Neo-Hookean model to planar tension data only.

Table 2: First-order Yeoh hyperelastic model coefficients (C_{10}) fitted to single characterisation curves as indicated with corresponding normalised root-mean-squared error, E_{NR}

Level of preconditioning (engineering strain)	C_{10} for first-order Yeoh model, $W = C_{10}(I_1 - 3)$, fitted to					
	Uniaxial data		Planar data		Equi-biaxial data	
	C_{10}	E_{NR}	C_{10}	E_{NR}	C_{10}	E_{NR}
Virgin stretch	6.0*	17%	6.4*	9%	5.0*	8%
5%	4.4540	5%	5.7862	6%	3.8087	2%
10%	3.0844	4%	3.5601	3%	2.8071	2%
15%	2.6408	3%	2.9170	3%	2.2595	3%
25%	1.9930	3%	2.1417	2%	1.7970	3%

*Coefficients determined manually

Table 3: Third-order Yeoh hyperelastic model coefficients (C_{10} , C_{20} and C_{30}) fitted to single characterisation curves as indicated with corresponding normalised root-mean-squared error, E_{NR}

Level of preconditioning (engineering strain) and state of strain	Third-order Yeoh coefficients $W = C_{10} (I_1 - 3) + C_{20} (I_1 - 3)^2 + C_{30} (I_1 - 3)^3$			
Uniaxial	C_{10}	C_{20}	C_{30}	E_{NR}
Virgin stretch	5.8715	-510.34	30206	29%
5%	6.0170	-1031.2	1.5700e5	2%
10%	4.2379	-203.38	8223.9	2%
15%	3.6862	-72.220	1150.1	1%
25%	2.4501	-11.900	63.999	2%
Planar	C_{10}	C_{20}	C_{30}	E_{NR}
Virgin stretch	5.7481	-322.58	13 822	15%
5%	8.4155	-1712.7	2.5912e5	3%
10%	4.8679	-204.33	7258.6	2%
15%	4.1748	-76.766	1086.7	2%
25%	2.6307	-11.037	51.477	2%
Equi-Biaxial	C_{10}	C_{20}	C_{30}	E_{NR}
Virgin stretch	4.4696	-67.847	953.81	13%
5%	4.3845	-135.17	6621.9	1%
10%	3.7282	-44.598	483.00	1%
15%	3.0045	-16.05	76.383	3%
25%	2.1445	-3.105	5.4358	2%

3.2.2. Limitations of the hyperelastic models

A compilation, based mainly on the author's own experience, of advantages and disadvantages of the hyperelastic models discussed in this work is presented in Table 4.

Table 4: Advantages and disadvantages of selected hyperelastic models

	Advantages	Disadvantages
Neo-Hookean	- Acceptable at low strain for unfilled rubber.	- Does not capture stiffening near elongation limit (higher order models are required).
Mooney-Rivlin	- Good fit to a single state of simple stress with higher order models (5 terms or more)	- Use with caution when fitting; possibility of losing physical meaning in other states of stress.
Ogden	- Good fit to a single state of simple stress with higher order models (3 rd order and higher)	- Computationally more expensive (eigenvalues are required).
Yeoh	- Often uniaxial characterisation data is sufficient to represent behaviour of unfilled rubber in other states of strain. - Higher order ($N > 2$) Yeoh models capture stiffening well.	
Gent	- Captures stiffening well by defining an elongation limit with J_m .	- The elongation limit term, J_m , introduces a singularity and may cause instabilities.

All these models share a common flaw: they all fail to capture large initial softening, typical of modern carbon-black-filled rubber, without losing physical meaning at higher strain. Most of the scientists and engineers who have proposed these models worked very

hard to represent the stiffening of rubber near its elongation limit. Unfortunately, none of these models seem to capture the considerable softening of filled rubber at moderate strain, unless they compromise their accuracy elsewhere. Thus, in most cases, the coefficients obtained by curve-fitting these models to experimental characterisation data fail to either capture the initial modulus or the softening that soon follows at moderate strain. In any case, the work done by the hyperelastic model (area below the stress-strain curve, i.e. the strain energy) will not match the work done by the actual rubber compound. And the models that may capture the full behaviour of rubber in one state of simple strain, will lose physical meaning in other states of strain.

One of the problems with the hyperelastic models fitted to the characterisation data at hand is that while a relatively acceptable fit may be obtained in one state of strain, the fit is not necessarily good in the other states of strain. Taking the models proposed in Fig. 32 it can be observed that, depending on which state of simple strain the model was obtained with, the predictions for the other states of strain are not as good. This issue is addressed in the next chapter with the biaxiality test, proposed to assist in determining which characterisation data should be prioritised in the curve-fitting for any given simulation.

Another problem arises from the fact that these models are fitted to preconditioned data. Choosing which preconditioned curve is best for a given analysis may not necessarily be easy, or even possible; different parts of a structure may undergo different levels of preconditioning. As seen in Table 2 where the first-order Yeoh coefficient, C_{10} , is proportional to the initial shear modulus of the material (see Table 1), there is a distinctive reduction in stiffness as the hyperelastic model is fitted to higher levels of preconditioning. In order to simulate the effect of preconditioning in a FE analysis, a preconditioning iteration is proposed, the details of which are proposed in the next chapter as well.

Third-order hyperelastic models are tricky to use with preconditioned characterisation data. The nonlinear behaviour of higher-order models is generally meant to predict the

stiffening of rubber often observed near the elongation limit of the material. The stiffening observed in the preconditioned curves of the material at hand is due to the Mullins effect (a similar effect can be observed in Fig. 7) and is considered a local nonlinearity, as opposed to the global stiffening often observed in rubber stretched to its elongation limit. When a preconditioned material is stretched beyond the strain level it was preconditioned at, another nonlinearity occurs, and the stress-strain behaviour suddenly falls back on to the virgin stretch path. Instead of predicting this behaviour, currently available hyperelastic models will continue stiffening which results in highly inaccurate predictions. When modelling the behaviour of preconditioned rubber with hyperelastic models it may be desirable to simply use a first-order model rather than risk getting unexpected results as soon as the strains in the FEA exceed the strain level at which the characterisation data was preconditioned for.

For example, take a third-order Ogden model fitted to the uniaxial tension characterisation data preconditioned to 15% engineering strain, as shown in Fig. 34 (due to the data manipulations, the characterisation data stops at a value just a little above 10% engineering strain). The normalised root-mean-squared error for this model with respect to the fitted data points (0-10% engineering strain) is $E_{RN} = 0.3\%$, i.e. this is an excellent fit. Yet, comparing this model to the data points beyond the level of preconditioning the normalised root-mean-squared error (0-15% engineering strain) jumps to 29%. The analytical solution for the third-order Ogden model in uniaxial tension to a nominal strain of 15%, predicts a nominal stress of $S = 5.65$ MPa (off the scale of the figure). But according to the characterisation data, the rubber would simply fall back on to the virgin stretch path with a nominal stress of $S = 1.70$ MPa. The residual error for this particular data point is 233%.

On the other hand, a simple first-order Yeoh model may not have as good of a fit as the third-order Ogden model to the data preconditioned to 15% engineering strain ($E_{RN} = 3\%$) yet, if the strain exceeds the level of preconditioning, the model prediction remains an acceptable fit with $E_{RN} = 6\%$ for the 0-15% engineering strain data points shown in the figure. While the first-order Yeoh model may not capture the full local nonlinearity of

the preconditioned rubber, for a nominal strain $\varepsilon = 0.15$, the nominal stress predicted is $S = 2.04$ MPa, which corresponds to 20% residual error at that specific data point. Using the first-order model allows to overshoot the strain level that the characterisation data was preconditioned for without losing too much accuracy.

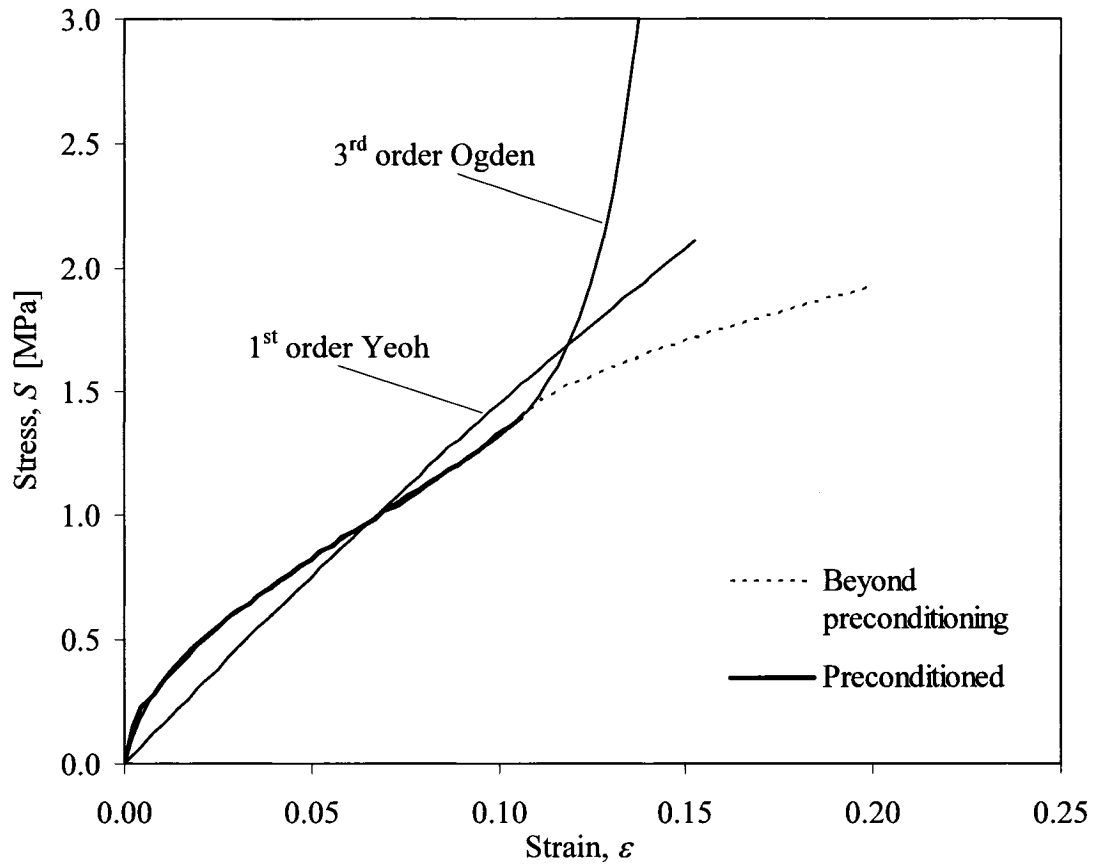


Fig. 34: Uniaxial tension data preconditioned to 15% (thick continuous line) then stretched beyond maximum preconditioning strain (dotted line). Ogden model: $\mu_1 = 208.41$ MPa, $\alpha_1 = 0.05305$, $\mu_2 = -0.40443$ MPa, $\alpha_2 = -123.08$, $\mu_3 = -0.4075$ MPa and $\alpha_3 = 61.4723$. 1st order Yeoh model: $C_{10} = 2.6408$ MPa.

Chapter 4: Hyperelasticity in ANSYSTM

In the first section of this chapter, the general FEA options relative to this work, including element types, element technology, element size and nonlinear solution options are discussed.

It has become clear from the previous chapters that hyperelastic models are limited in predicting the complex behaviour of rubber. One of these limitations is addressed here where an iterative method is proposed to approximate the effect of preconditioning with hyperelastic models. This method will be referred to as the preconditioning iteration. Furthermore, in order to provide insight on the dominant state of strain in a given simulation and hence to assist in selecting the appropriate characterisation data for curve fitting, a biaxiality test is proposed.

The procedure applied when conducting FEA simulations with the preconditioning iteration is also described in this chapter. The application of the preconditioning iteration and the biaxiality test will become more obvious in Chapters 5 and 6 where they are applied to FEA models and compared to experimental results.

4.1. Selection and validation of finite element analysis options

It is difficult to establish standardised methods for finite element analysis, although there is an independent not-for-profit organisation called the National Agency for Finite Element Methods and Standards (NAFEMS) whose purpose is to do just that.^{††} Efforts are also apparently being made by the American Society of Mechanical Engineers (ASME) to standardise finite element methods [see Schwer (2006)]. While standards do exist, each analysis must be treated differently. This section briefly discusses the FEA options chosen for this work.

^{††} <http://www.nafems.org/>

4.1.1. Element type and technology

Several types of elements are currently available in ANSYSTM: from one-dimensional truss and beam elements, to two-dimensional elements with plane-strain, plane-stress, or axisymmetric options, to three-dimensional solid and shell elements; there are often several choices of elements for one given type of analysis. All element types (and more) are extensively documented in the Release 10.0 Documentation for ANSYS (2005). Dufour (2003) also provides an interesting review of the structural element types available in the ANSYSTM software.

Two types of three-dimensional solid elements are used in this work: an 8-node linear hexahedral element and a 10-node quadratic tetrahedral element, known as the SOLID185 and SOLID187 elements, respectively, in the Release 10.0 Documentation for ANSYS (2005). A schematic representation of these two element types is provided in Fig. 35.

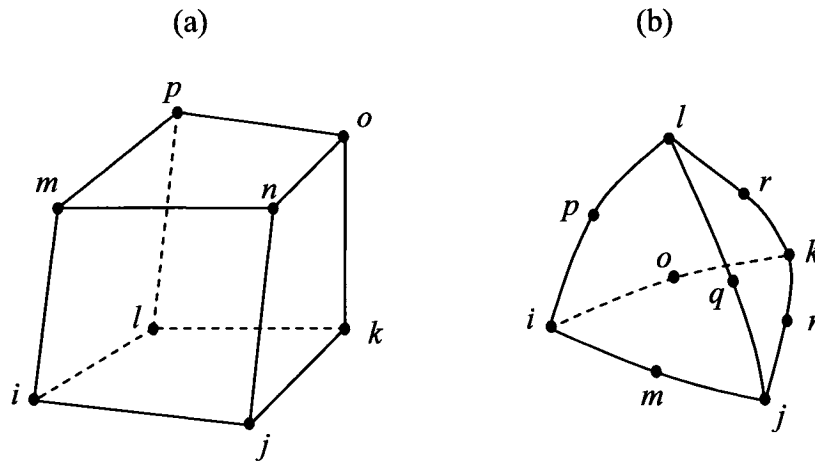


Fig. 35 : (a) 8-node linear hexahedral element (SOLID185), (b) 10-node quadratic tetrahedral element (SOLID187).

When meshing geometry, elements must respect certain shapes in order for them to provide acceptable results. Fortunately, software packages such as ANSYSTM automatically perform shape testing on elements and issue warnings if the default shape limits are exceeded. These limits are determined by the software developers and they

depend on the element type. Refer to Section 13.7 of the Theory Reference in the Release 10.0 Documentation for ANSYS (2005) for details on shape testing.

The algorithms currently used to automatically mesh geometries with tetrahedral elements are very robust; thus these elements are often employed to mesh complicated geometries. On the other hand, in certain cases, such as for dynamic impact simulations, hexahedral elements are often required. There are now meshing tools that facilitate hexahedral meshing of complicated geometry (notably the blocking technique available in AI EnvironmentTM software). The quadratic tetrahedral, SOLID187, element type is considered reliable enough for the purposes of this work.

Although it is not the case in this work, it is possible to have models that have quadratic tetrahedral SOLID187 elements on one side of a coincident face and linear hexahedral SOLID185 elements on the other side. This is made possible with a morphed version of the SOLID187 element that has a four sided base at the interface without mid-side nodes such that it becomes compatible with the SOLID185 element sharing the same face.

4.1.2. Element technology and formulation

While the degrees of freedom in an element are usually calculated at the nodes, the strains and stresses are calculated at Gauss points; these are called integration points. The number of integration points solved for in an element depends on the element's technology and user-specified options.

Two technologies related to element integration are considered here: the \bar{B} method (a.k.a. B-bar or selective reduced integration) and the URI method (uniform reduced integration). Both methods help prevent shear and/or volumetric locking when a material is incompressible or nearly incompressible. Using the URI method on an 8-node hexahedral element requires only one integration point and is therefore more efficient than the \bar{B} method. On the other hand, the URI method may cause mechanical (a.k.a. hourglass or zero-energy) modes. This happens when an element deforms to a shape that requires no work with respect to the integration point(s). Two mechanical modes are

shown in Fig. 36 for a two-dimensional linear element; note that these modes are similar for three-dimensional elements. Hourglassing can be controlled by introducing hourglass stiffness but it must be monitored. It is important that the artificial energy in an element due to hourglass stiffness remains small with respect to the internal energy of the same element. The Release 10.0 Documentation for ANSYS (2005) recommends as a guideline that “the hourglassing energy should not exceed 10% of the internal energy”.

The SOLID185 and SOLID187 elements are an appropriate choice since they are said to have “[...] hyperelasticity, [...] large deflection, and large strain capabilities. [They] also [have] mixed formulation capability for simulating deformations of nearly incompressible elastoplastic materials, and fully incompressible hyperelastic materials.”^{§§} The mixed formulation, referred to as the mixed u-P formulation, adds an additional hydrostatic pressure degree of freedom and is thus very appropriate for incompressible materials.

The reader is referred to the Element Reference section in the Release 10.0 Documentation for ANSYS (2005) for more information on integration methods and element technologies.

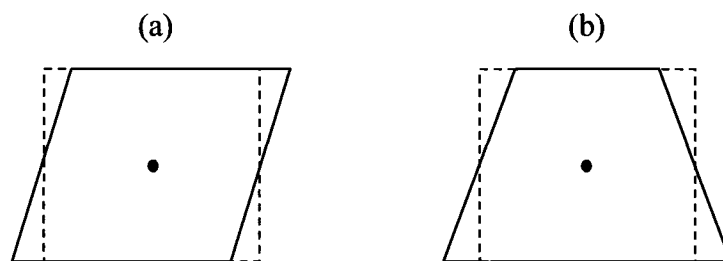


Fig. 36 : Hourglassing in two-dimensional linear elements showing: (a) a parallelogram type hourglass mode and (b) a trapezoid type hourglass mode. The original element shape is represented with a dashed line (---) while the hourglass mode is represented with a continuous line (—), the integration point is shown in the middle of each element.

4.1.3. Element size

The size of elements used in a FEA differs for every simulation and every load case. In order to determine the most appropriate element size for a given analysis, a convergence

^{§§} Release 10.0 Documentation for ANSYS (2005)

test must be performed where the element size is refined until the difference between the results from one analysis to the next is negligible. Refinement is also necessary where large deformation gradients are present. Element size convergence tests are conducted on both simulations presented in this work, in Chapters 5 and 6.

4.1.4. Nonlinear solution control

Nonlinear structural static simulations in ANSYSTM are solved using the Newton-Raphson iterative method. In this method, a certain number of substeps must be solved in order to obtain the final result. Substeps are solved with Newton-Raphson iterations such that the substep has converged when the convergence criterion is satisfied. A default convergence criterion exists but may be changed if desired. In this work the default convergence criterion is used. If a substep does not converge after a certain number of Newton-Raphson iterations, the solution will stop. The reader is referred to the Release 10.0 Documentation for ANSYS (2005) for further information on convergence criteria for structural nonlinear static analysis and how to troubleshoot when a simulation is not converging.

Substeps are a fraction of the total load; each substep consists of a load increment such that, when the final substep is solved, the total load has been applied. The number of substeps in an analysis may be controlled by defining the initial number of substeps, the minimum number of substeps and the maximum number of substeps. Alternatively, substeps can be seen as fictitious time increments (fictitious since it is a static analysis and thus there are no time-dependent variables such as viscosity and momentum). Thus, one can also choose to control the initial time increment, the minimum time increment and the maximum time increment of a nonlinear static analysis in ANSYSTM.

4.1.5. Finite element analysis validation with analytical solutions

In order to ensure that the FEA software used in this work, ANSYSTM, provides satisfactory results, a single linear hexahedral element is given hyperelastic material properties, stretched in the three states of simple strain, and then compared to the analytical solution. A third-order Yeoh model fitted to the uniaxial characterisation data

preconditioned to 25% engineering strain is tested. While it is important to do this test, it will not be extensively discussed here for the simple reason that, in all three states of simple strain, the ANSYSTM solver predicts the exact analytical solution up to the numerical order of precision of the software, which by default in ANSYSTM consists of eight significant figures. Double precision could be activated in which case the ANSYSTM solver would predict the exact analytical solution up to sixteen significant figures.

4.2. Modelling preconditioning

In simple loading cases it may be acceptable to assume that all parts of a structure have been preconditioned to the same level of strain, as could be the case for cylindrical rubber bearings in seismic isolation systems which are mainly subjected to compressive or tensile loads and are not expected to bend. On the other hand, structures are more often than not subjected to loads (such as bending loads) that will lead to different levels of strain and thus different levels of preconditioning.

A method is proposed in this section to approximate the effects of strain-induced stress-softening in a static FEA simulation using hyperelastic models. It is assumed that the material is or acts like a carbon-filled rubber at moderate strain. In other words, deformations are small enough that the range of deformation still remains in the softening stage of the material (such as in Fig. 21).

A first analysis of the finite element model to the desired deformation must be performed with a hyperelastic model that captures the qualitative behaviour of the rubber; i.e. the deformations are acceptable but not necessarily the stresses (or the predicted loads). Due to the moderate (see Fig. 21) range of strain (0-25% engineering strain), a first-order Yeoh model would be an appropriate hyperelastic model for this purpose.

The results of the first FEA simulation are then post-processed and the elements are classified according to their average maximum principal strain. Next, the elements are assigned new material properties; the hyperelastic model of the element is changed such

that it is fitted to a level of preconditioning according to the strain range in which it is classified, as shown in Table 5. These ranges of strain represent the levels at which the characterisation data was preconditioned after it has been manipulated (as described in Appendix B) and converted to Hencky strain with the use of Eqs. (2.10) and (2.14).

Note that the offset strains for the characterisation data preconditioned to 5%, 10%, 15% and 25% engineering strain in uniaxial tension will be different from the respective offset strains in the biaxial test and again for the planar tension test. Nonetheless, they differ very little; so, for the purpose of the preconditioning routine, the preconditioned strain values, once manipulated and converted to Hencky strain, in all three states of simple strain are assumed to be the same; thus, the data preconditioned to 5% engineering strain becomes preconditioned to $\sim 3\%$ Hencky strain. Similarly, the data preconditioned to 10%, 15% and 25% engineering strain becomes preconditioned to $\sim 6\%$, $\sim 10\%$ and $\sim 18\%$ Hencky strain, respectively.

The use of first- and third-order Yeoh hyperelastic models with the preconditioning iteration will be discussed in the next two chapters.

Table 5: Classification of elements according to their maximum principal strain

Classification	Corresponding preconditioned data
$\bar{\epsilon}_1 \leq 0.005$	Virgin initial stiffness
$0.01 < \bar{\epsilon}_1 \leq 0.03$	5%
$0.03 < \bar{\epsilon}_1 \leq 0.06$	10%
$0.06 < \bar{\epsilon}_1 \leq 0.10$	15%
$0.10 < \bar{\epsilon}_1$	25%

It could be argued that the material constants for preconditioned strain values could be interpolated and that a different hyperelastic model could be assigned to each individual element for a more accurate solution. This was not done since, as will be seen in the

following chapters, the results are accurate enough that it probably would not be efficient to try to improve them by assigning interpolated material properties to all the elements. Furthermore this method is merely an artificial way of simulating a material behaviour that would probably be much better modelled with a constitutive material law that accounted for the Mullins effect.

4.3. Biaxiality test

It has been proven difficult to obtain one set of coefficients for a hyperelastic model that would fit well in all three simple states of strain. A compromise may be necessary for a globally acceptable fit. Otherwise, there is acceptable behaviour in one strain state but not in the other two. For simple loading scenarios, it is merely a matter of carefully selecting the hyperelastic model that best fits the dominant state of strain. However, in the context of FEA models under multi-axial loads, the aforementioned lack of accuracy may lead to false results.

Since the material is assumed incompressible, the deformation of an element of rubber has only two independent variables. The maximum principal stretch, λ_1 , and the minimum principal stretch, λ_3 , will be conveniently chosen as the two independent variables in the context of the biaxiality test.

Let us define the biaxiality ratio, α , as the ratio of the minimum principal stretch, λ_3 , to the maximum principal stretch, λ_1 :

$$\alpha = \frac{\lambda_3}{\lambda_1}, \quad (4.1)$$

where $\lambda_1 \geq 1$ and $\lambda_3 \leq 1$ always holds for incompressible materials. The value of α lies somewhere between 0 and 1, and will only equal 1 if there is no deformation. Note that the biaxiality ratio evaluates the state of deformation in an element, irrespectively of the state of stress.

Due to incompressibility, the biaxiality ratio of an element will have an upper boundary when in uniaxial extension, and a lower limit when in equi-biaxial extension, for which

the respective biaxiality ratios are $\alpha_U = \lambda_1^{-3/2}$ and $\alpha_B = \lambda_1^{-3}$. Any other state of deformation lies somewhere in-between the upper limit, α_U , and the lower limit, α_B , including the state of planar deformation, with biaxiality ratio $\alpha_P = \lambda_1^{-2}$, which is somewhere in-between.

The following biaxiality ratios are arbitrarily identified, in this case through a simple thirds rule:

$$\alpha_{U-P} = \frac{2}{3} \alpha_P + \frac{1}{3} \alpha_U, \quad (4.2)$$

$$\alpha_{B-P} = \frac{2}{3} \alpha_P + \frac{1}{3} \alpha_B. \quad (4.3)$$

The five newly defined biaxiality ratios are plotted against the maximum principal stretch, λ_1 , in Fig. 37.

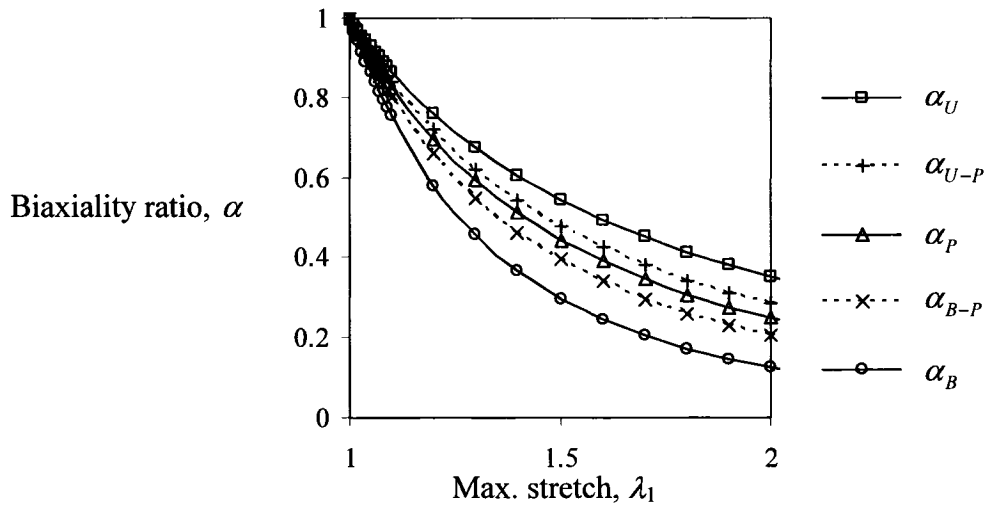


Fig. 37: Defined biaxiality ratios plotted against the maximum principal stretch, λ_1 . It is assumed that the biaxiality ratio of any incompressible element will have a value between α_B and α_U .

Applying the biaxiality test to a FEA simulation requires that a first analysis of the model be conducted to the desired deformation. The results are then post-processed and the elements are classified into three regions of dominant deformation, as defined in Table 6. A region of dominant uniaxial extension between α_U and α_{U-P} , a region of planar

deformation between α_{U-P} and α_{B-P} , and a region of equi-biaxial extension between α_{B-P} and α_B .

It may be desirable to work with the logarithmic biaxiality ratio, $\bar{\alpha}$, which is defined as

$$\bar{\alpha} = \ln(\alpha) = \ln\left(\frac{\lambda_3}{\lambda_1}\right) = \varepsilon_3^n - \varepsilon_1^n. \quad (4.4)$$

The logarithmic biaxiality ratio, $\bar{\alpha}$, is fundamentally the same as the biaxiality ratio, α , but becomes particularly useful when working with software packages such as ANSYS™, since the principal logarithmic strains are readily available.

Table 6: Classification of elements according to their biaxiality ratio

Region of dominant strain	Biaxiality ratio
Uniaxial	$\alpha_U > \alpha > \alpha_{U-P}$
Planar	$\alpha_{U-P} \geq \alpha \geq \alpha_{B-P}$
Equi-biaxial	$\alpha_{B-P} > \alpha > \alpha_B$

The biaxiality ratio will be applied to FEA simulations and discussed in the next two chapters.

4.4. FEA procedure and methodology

The flow chart shown in Fig. 38 describes the generalised procedure undertaken in this thesis to perform FEA simulations with the preconditioning iteration.

The first step is to build the FEA model and apply the boundary conditions. A hyperelastic model is then selected to represent the elastic behaviour of the rubber. As will be discussed later, the hyperelastic model coefficients are quite arbitrary. A first analysis is then conducted on the FEA model; it is critical that the desired displacement be achieved in this step.

Branching off to the right, below the first analysis in the flow chart in Fig. 38, the preconditioning iteration can begin. The average maximum principal Hencky strains are retrieved from the results file of the first analysis. It is emphasised that for the preconditioning iteration to be accurate, the desired deformation field must be attained in the first analysis while the loads and stresses calculated in the first analysis are irrelevant. These results may be at any substep of the analysis provided the appropriate value of displacement is achieved. The elements of the analysis can then be classified according to their strain range as defined in Table 5. The hyperelastic model attributed to each group of classified elements will depend on the available characterisation data or can also be determined from the biaxiality test.

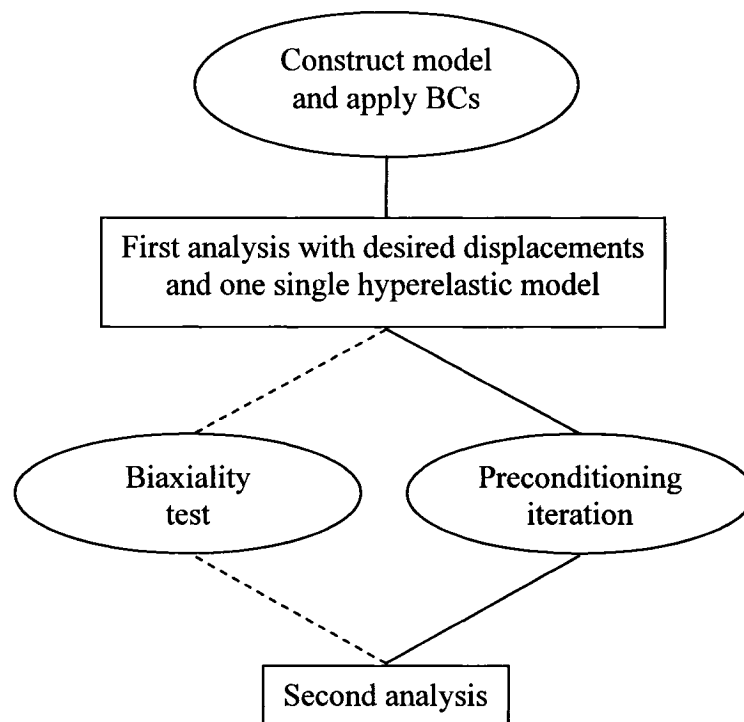


Fig. 38: Flow chart describing the procedure to follow in order to perform a FEA simulation with the biaxiality test and preconditioning iteration

The biaxiality test can be performed following the first analysis of the FEA model (left branch below first analysis in the flow chart from Fig. 38). The biaxiality test requires

the average maximum and average minimum principal strain in every element from the results file of the first analysis. The dominant state of strain for a FEA simulation determined by the biaxiality test may assist in selecting the appropriate characterisation data (state of simple stress) to be fitted to a hyperelastic model.

Chapter 5: Bending of a Cantilevered Plate

This chapter examines the problem of cantilevered rubber plate under bending. While quite simple, bending problems will have different levels of preconditioning and may demonstrate different states of biaxiality, making it an ideal candidate for the preconditioning iteration and the biaxiality test.

It is well known that the convex surface of a bending plate is in tension while the concave surface is in compression. Larger deformations occur near the surfaces of the plate rather than near the neutral axis^{***}. If subjected to cyclic loading, the properties of the rubber plate may change along the thickness, making the bending plate an ideal subject for the preconditioning iteration. Furthermore, “end effects” effects are expected along the width of the plate with dominantly uniaxial loads (tension or compression) at the extremities and dominantly under planar loading at mid-width of the plate, putting the biaxiality test to trial.

An experimental bench-test of a bending cantilevered rubber plate was conducted to provide validation data for FEA simulations where the preconditioning iteration and the biaxiality ratio are tested.

5.1. Experimental bench-test

A description of the experimental set-up used to apply a bending load to a cantilevered rubber plate is presented here. The experimental results are then given and briefly discussed.

5.1.1. Experimental set-up and procedure

A rubber plate made of the characterised material was used for this experiment. The plate was clamped horizontally and a steel bar was laid across the free end of the plate from which weights were hung; a schematic representation is provided in Fig. 39. The

^{***} Note that in the case of a bending plate made of a rubber-like material, the neutral axis is not necessarily at mid-thickness.

steel bar was rigid and used to evenly distribute the load along the width of the plate. The geometry of the plate with respect to the coordinates given in Fig. 39 is given in Table 7, along with the position of the displacement gauge and the width of the rigid bar.

The same weights were used in the same order for each load set. The total load when all the weights were hung was 92.26 N (corresponding to a mass of 9.4 kg). The plate was loaded and unloaded, and then reshaped manually until it was straight again. This procedure was repeated several times in order to precondition the material before the recorded load sets were conducted.

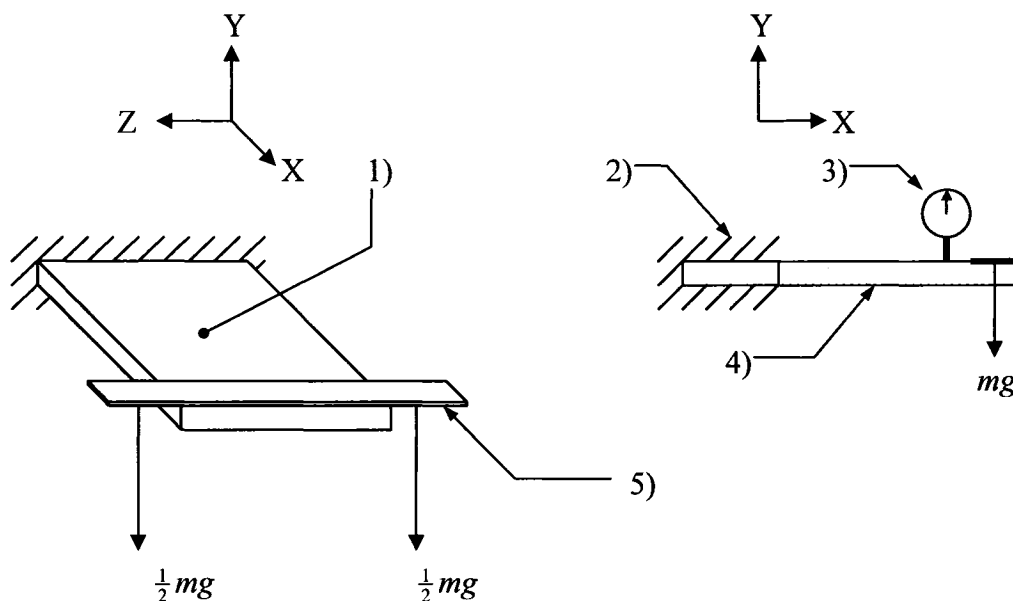


Fig. 39: Schematic representation of the experimental bench test of a cantilevered rubber plate subjected to a bending load, mg . The labels indicate the 1) rubber plate, 2) clamped section, 3) displacement gauge, 4) free section and 5) rigid steel bar.

Table 7: Geometric parameters for the bending cantilevered rubber plate bench test

Total length (X-axis)	201.5 mm
Free length (X-axis)	125.3 mm
Width (Z-axis)	151.0 mm
Thickness (Y-axis)	16.25 mm
Position of displacement gauge along length, from free edge	25.3 mm
Width of rigid bar (X-axis)	12.3 mm

After each load increment, a 2 minute interval was taken before measuring the displacement to let the viscous (creep) effects take place. Particularly at the beginning of the two minute interval, the displacement gauge indicated continuous change in position at a relatively high rate (this rate could not be measured with the available equipment). The dial of the displacement gauge would then slow down and by the end of the two minutes would have stopped or nearly stopped. Since the load was hanging from strings at the free end of the plate, care had to be taken to ensure the load would not swing; otherwise the swinging would induce jumps in the creeping effect observed on the displacement gauge dials. Since the experiments were meant to be quasi-static (and thus strain rate and other time dependent effects were undesirable), the swinging of the load was avoided during the recorded experiments.

5.1.2. Results from experimental bench-test

Four load sets were recorded following the preconditioning of the material. The applied load and corresponding displacement measured from the displacement gauge for the first two load sets are shown in Fig. 40. In the first load set, only the loading (not the unloading) was recorded, the plate was then reshaped and the gauge reset for the second load set. In the second load set, the loading and unloading process was recorded. Load set 3 was conducted immediately after load set 2 without resetting the gauge or reshaping the plate, which explains the residual displacement seen in Fig. 41. While the gauge was not reset nor was the plate reshaped for load set 4, there was a pause between the end of load set 3 and the beginning of load set 4 (approximately one hour). This allowed the plate to recover in shape a little more during the pause, explaining why the measurement taken at the end of load set 3 (completely unloaded) indicated a greater displacement than at the beginning of load set 4 (still no load).

The hysteretic behaviour and residual strain observed in Fig. 41, while very interesting, are not predictable with currently available hyperelastic models, which only predict purely elastic behaviour, and hence only the loading paths of the first two load sets will be considered in the FEA simulations presented in Section 5.2.

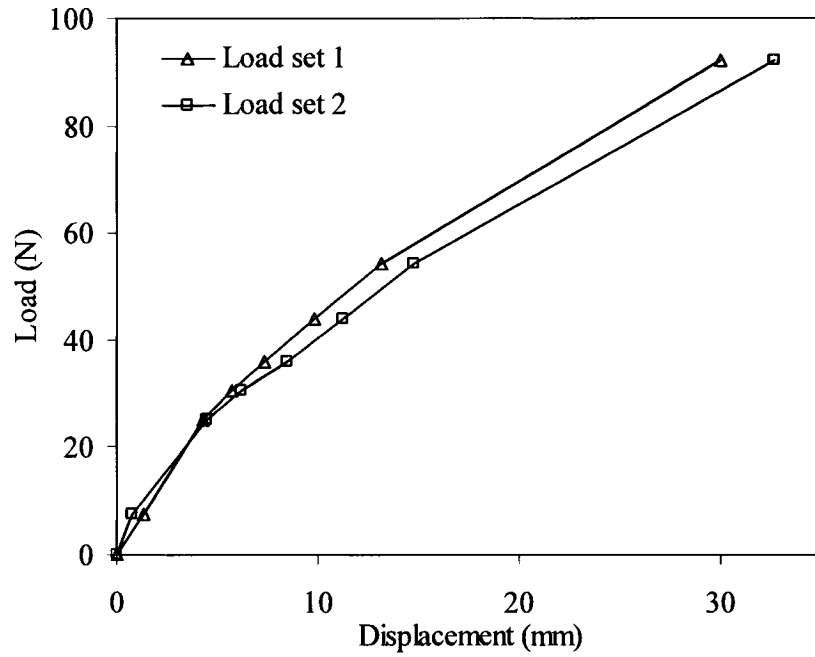


Fig. 40: Loading paths only for load sets 1 and 2 of the bending cantilevered plate experiment.

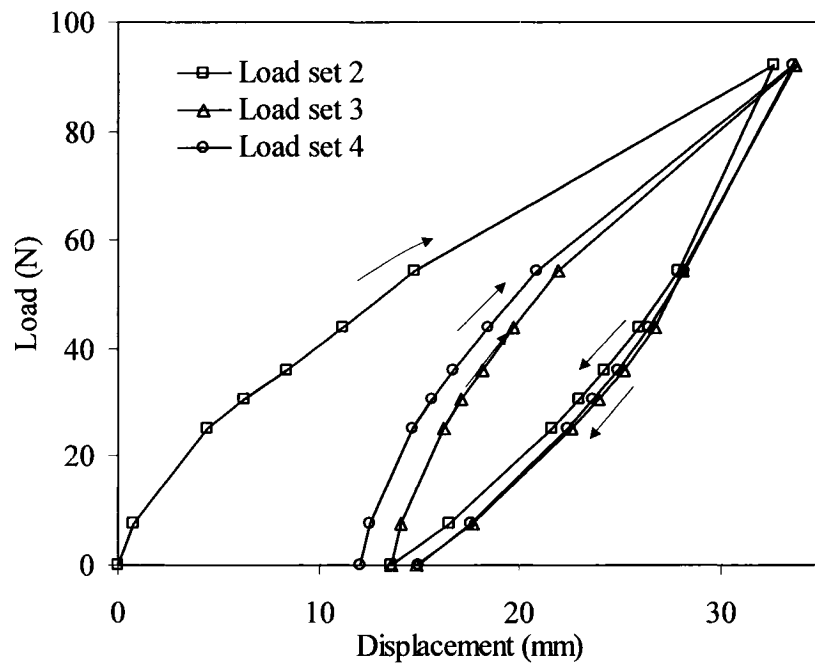


Fig. 41: Loading and unloading paths for load sets 2, 3 and 4 of the bending cantilevered plate experiment. The arrows indicate whether it is a loading or unloading path.

5.2. Finite Element Simulations

This section describes the FEA simulations that were performed to predict the results obtained in the experiments of the bending cantilevered rubber plate. Some predictions are presented from simulations using a single hyperelastic model. The biaxiality test is conducted on the FEA model and discussed. The preconditioning iteration is then applied to the simulation. This second iteration is shown to greatly improve the results predicted by FEA.

5.2.1. Finite element simulation problem definition

The symmetrical half of the cantilevered plate is modelled in the FEA software ANSYS™, as shown in Fig. 42. The nodes on the symmetry face of the model are given “sliding-only” boundary conditions (in this case, only displacements in the Z -direction are fixed). The nodes on the top and bottom surface of the section of the plate that is clamped, as defined in Table 7, are given a “zero displacement” boundary condition. A virtual displacement gauge is set on the top surface of the plate right at the symmetry edge (centred along the width); its position along the length is that given in Table 7. The gauge is modelled with a free node that has a frictionless and no separation contact with the plate. Furthermore, the node is not permitted to move in the Z - and X -directions. This way, the gauge node is displaced vertically along a fixed axis while not interfering with the plate by sliding along its surface, such as a real displacement gauge would (or at least with very little interference).

A contact region, the size of the steel bar used to load the plate, is created in ANSYS™. The deformations in the steel are neglected and the contact is thus modelled as a rigid one. A force load is applied to the rigid bar via a pilot node. The load is applied such that the force always acts in the Y -direction such as to simulate the act of gravity on a weight suspended from the rigid bar.

Given that the analysis type is nonlinear static, each substep solved for by the ANSYS™ solver represents a linear increment of the load until the final load is achieved. Retrieving the results obtained at all the substeps solved for in the static analysis provides

a load-history of the simulation that can be compared to the quasi-static load-history from the experiments.

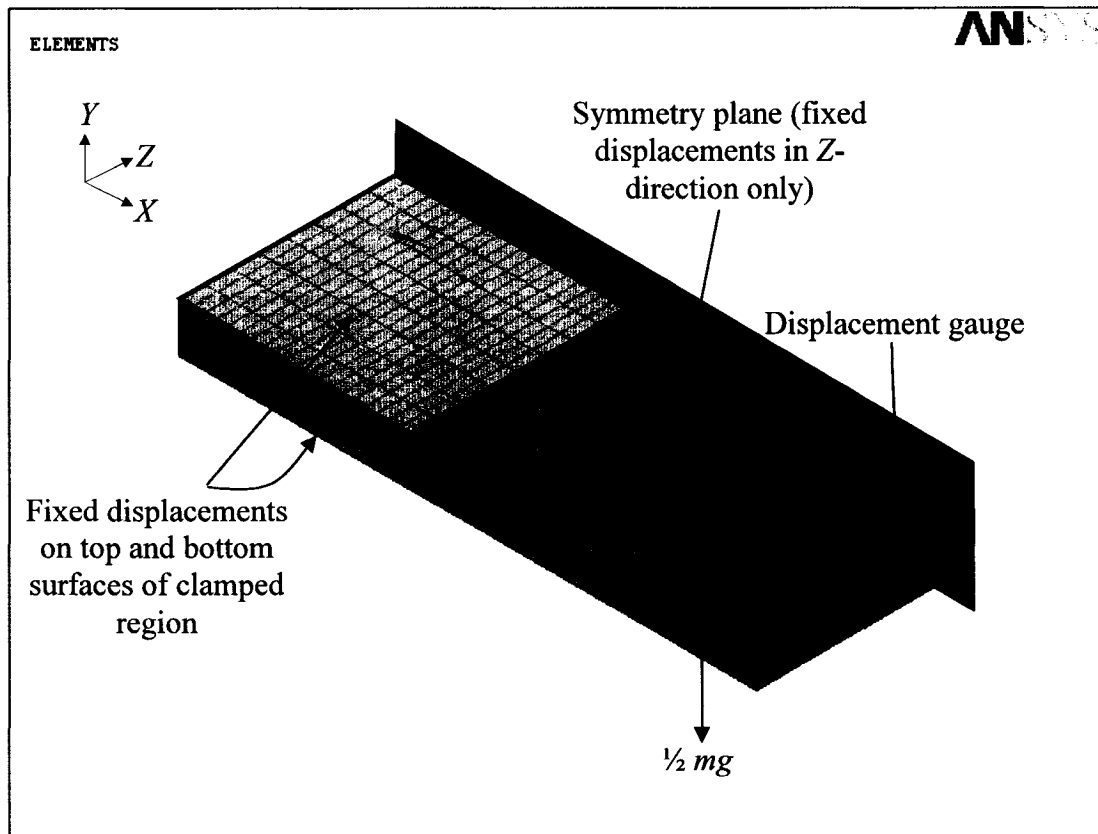


Fig. 42: FEA model with boundary conditions for the bending cantilevered plate.

Since in this analysis linear hexahedral SOLID185 elements were used and that the uniform reduced integration method was applied to reduce computation time, an hourglass stiffness factor of 50 was used to avoid hourglassing. As discussed in Section 4.1.2., the hourglass stiffness factor must have a high enough value to avoid the propagation of mechanical modes (a.k.a. hourglassing) due to reduced integration, and a low enough value such that the artificial energy that it incurs in each element does not exceed a fraction of the same element's total internal energy. Although the ratio of artificial energy to internal energy in certain elements between the clamped surfaces may exceed 5%, this will be considered acceptable since these elements have little influence in the results.

The element size was determined by solving the FEA model with a coarse mesh then by refining the elements until convergence in the results was observed. The convergence test shown in Fig. 43 was performed with a first-order Yeoh hyperelastic model fitted to the characterization data preconditioned to 10% engineering strain. In this figure the final deformation of the displacement gauge is shown with respect to the number of elements used along the thickness (curve with circles). The percent change in final displacement from one element size to the next is also shown on the same figure using the secondary vertical axis on the right-hand side of the figure (curve with squares). The number of elements along the width and the element size along the length were refined at the same time as the number of divisions along the thickness. The element size convergence obtained with 8 elements along the width (with the corresponding element sizes along the length and width) is acceptable for the purpose of this work and will be used for all further simulations of the bending cantilevered plate. This corresponds to a total of 3264 8-noded hexahedral elements.

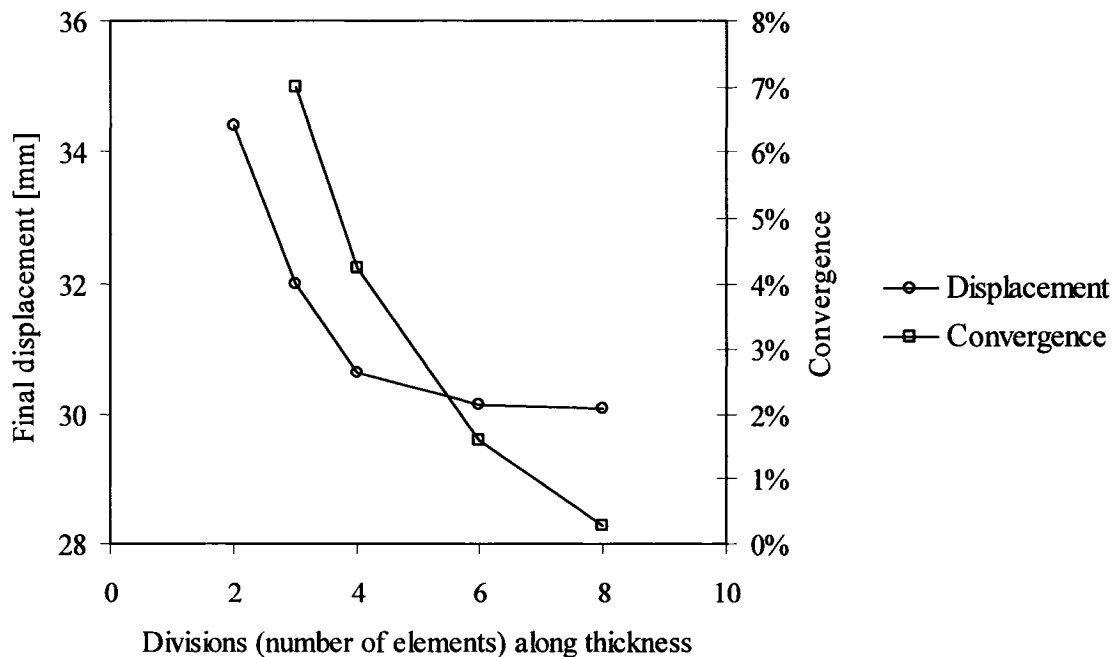


Fig. 43: Effect of refining the mesh in the FEA of the bending cantilevered plate modelled here with a first-order Yeoh hyperelastic model fitted to the planar characterisation data preconditioned to 10% engineering strain.

5.2.2. FEA results using a simple hyperelastic model for the rubber

Several FEA simulations were conducted using different hyperelastic models with different coefficients. These coefficients were determined by fitting the hyperelastic models to a single characterisation curve at a time. The following results were obtained with first- and third-order Yeoh hyperelastic models, the coefficients for which are listed in Table 2 and Table 3 of Section 3.2.1. It is recalled that the first-order Yeoh model is equivalent to the Neo-Hookean model.

Figs. 44, 45 and 46 show FEA predictions solved with first-order Yeoh hyperelastic models, each respectively fitted to the uniaxial, planar and equi-biaxial tension characterisation data preconditioned to 5%, 10% and 15% engineering strain. Keep in mind that the points represent experimental data while the continuous lines represent the FEA results.

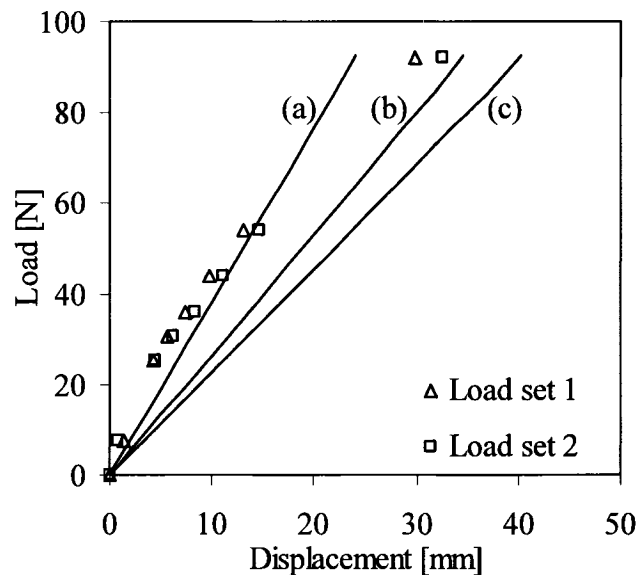


Fig. 44: FEA predictions with a first-order Yeoh hyperelastic model fitted to the uniaxial tension characterisation data preconditioned to (a) 5%, (b) 10% and (c) 15% engineering strain.

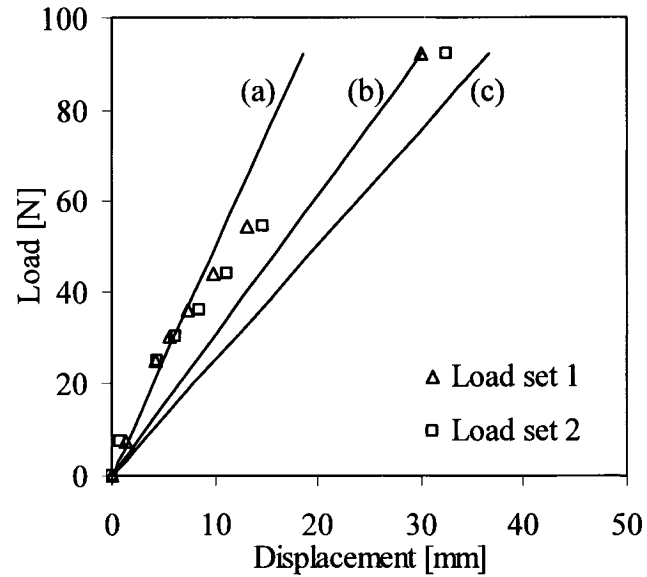


Fig. 45: FEA predictions with a first-order Yeoh hyperelastic model fitted to the planar tension characterisation data preconditioned to (a) 5%, (b) 10% and (c) 15% engineering strain.

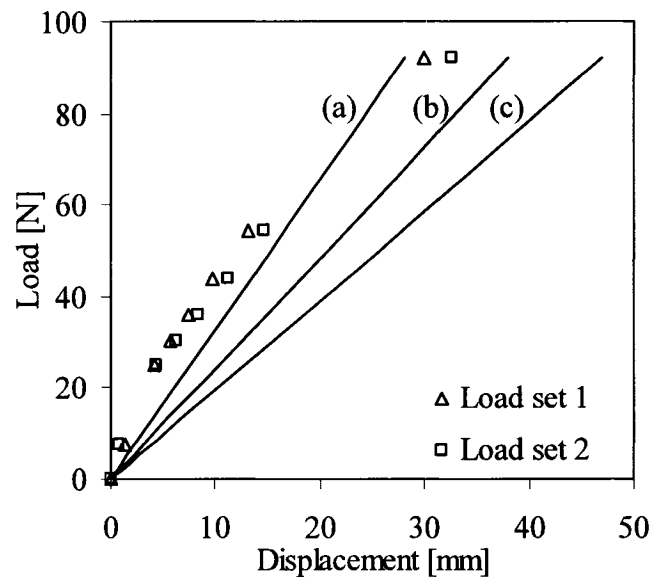


Fig. 46: FEA predictions with a first-order Yeoh hyperelastic model fitted to the equi-biaxial extension characterisation data preconditioned to (a) 5%, (b) 10% and (c) 15% engineering strain.

All the results predicted with the first-order Yeoh hyperelastic model show a relatively linear load-displacement response, regardless of the characterisation curve they were

fitted to or, mathematically speaking, regardless of the value of the hyperelastic coefficient, C_{10} . Due to the nonlinear nature of the experimental results, the predictions obtained with the first-order Yeoh hyperelastic model agree with the experiments only over a certain range of load. For example, the FEA prediction with the first-order Yeoh fitted to the 5% planar data (Fig. 45) is relatively good for roughly the first third of the total load while the 5% uniaxial fit (Fig. 44) shows good prediction for roughly the second third of the total load. The last third of the total load is not predicted by any of the simulations, although both the 10% planar fit (Fig. 45) and the 5% equi-biaxial fit (Fig. 46) come pretty close to the experimentally measured displacement at the final load. Unfortunately, none of these observations lead to a preferred characterization test for a first-order Yeoh hyperelastic model.

The FEA results obtained with the third-order Yeoh hyperelastic model clearly show nonlinear load-displacement behaviour. Fig. 47 shows two FEA predictions solved with a third-order Yeoh hyperelastic models, each respectively fitted to the uniaxial tension characterisation data preconditioned to 5% and 10% engineering strain. The predictions using a third-order Yeoh model fitted to the uniaxial characterisation data preconditioned to 5% engineering strain agree very well with the early load-displacement stage of the experiment up to a displacement of around 15 mm. At this point the FEA results predict sudden stiffening that was not observed in experiment. The load required to bend the plate to the final displacement measured in experiment would be several orders of magnitude greater than in the experiment. As discussed in Section 3.2.2, this is due to the fact that the third-order hyperelastic material fitted to data preconditioned to 5% engineering strain behaves as if it had reached its elongation limit. In practice, when rubber is stretched beyond its level of preconditioning, the stress-strain behaviour falls back on to the virgin stretch path of the material. At low to moderate levels of strain, this has a considerable softening effect.

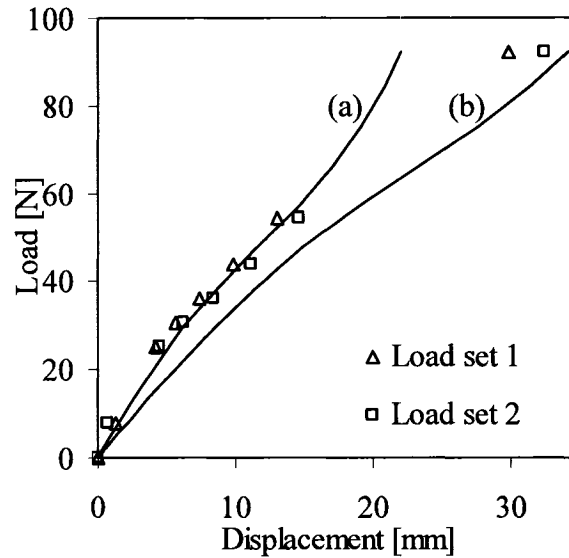


Fig. 47: FEA predictions with third-order Yeoh hyperelastic models fitted to the uniaxial tension characterisation data preconditioned to (a) 5% and (b) 10% engineering strain, as labelled in the figure.

Fig. 48 shows two FEA predictions solved with a third-order Yeoh hyperelastic models each respectively fitted to the planar tension characterisation data preconditioned to 5%, 10% and 15% engineering strain. In this case, the third-order Yeoh model fitted to the data preconditioned to 10% engineering strain show the best agreement with the experiments. Fig. 49 shows two FEA predictions solved with a third-order Yeoh hyperelastic model, each respectively fitted to the equi-biaxial extension characterisation data preconditioned to 5%, 10% and 15% engineering strain. These results show the least nonlinearity of all the results obtained with third-order Yeoh hyperelastic models.

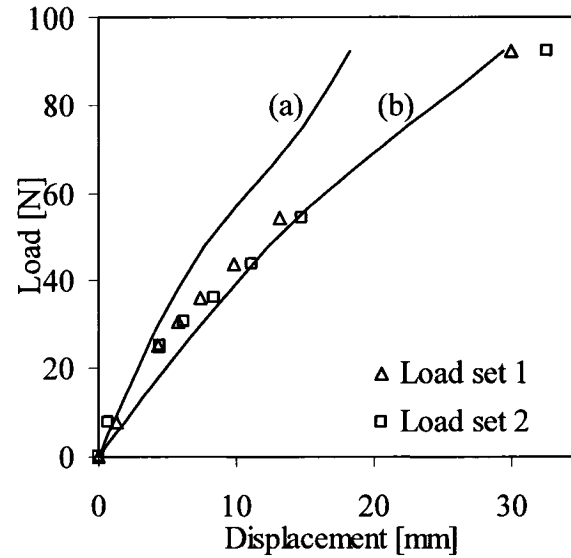


Fig. 48: FEA predictions with third-order Yeoh hyperelastic models fitted to the planar tension characterisation data preconditioned to (a) 5% and (b) 10% engineering strain, as labelled in the figure.

While some of the results obtained with the third-order Yeoh models are arguably in good agreement with the experiments, it is still not clear which level of preconditioning, the 5% or the 10% one, or which state of simple strain should be used to obtain the hyperelastic coefficients. Furthermore, it would not be appropriate to assume that all the elements in this type of analysis, particularly across the thickness and near the clamped edge, undergo the same level of preconditioning. Hence, choosing one level of preconditioning over another to curve-fit the hyperelastic model may seem quite arbitrary. The preconditioning iteration and the biaxiality test will be applied to the FEA models in the following two sections, in an attempt to solve some of these issues.

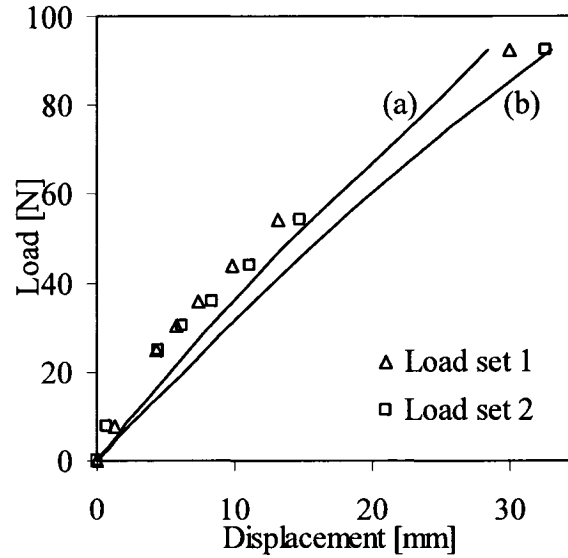


Fig. 49: FEA predictions with third-order Yeoh hyperelastic models fitted to the equi-biaxial extension characterisation data preconditioned to (a) 5% and (b) 10% engineering strain.

5.2.3. Preconditioning iteration applied to the bending cantilevered plate

As mentioned before, it is well known that the material nearest the neutral axis of a bending plate will deform very little, whereas the top and bottom surfaces will undergo the largest strains. During cyclic loading, the plate will be preconditioned to different states of maximum strain, meaning that it will show different stress-strain behaviour across its thickness. The preconditioning iteration requires that a previous FEA simulation be conducted where the desired maximum deformation has been attained.

Due to the nature of the boundary conditions (applied load rather than imposed displacement), the results from the FEA simulations where the final predicted gauge displacement is closest to that measured in the experiments will be used for the preconditioning iteration. Three simulations are selected for the purpose of the preconditioning iteration; they are listed in Table 8. In order to facilitate reference to the hyperelastic models used in these simulations, they are given labels. Accordingly, Y1ST_10P refers to a first-order Yeoh model (Y1) fitted to the uniaxial tension, or simple tension (ST), characterisation data preconditioned to 10% engineering strain (10P). Similarly, Y1PT_10P refers to a first-order Yeoh model (Y1) fitted to the planar tension

(PT) characterisation data preconditioned to 10% engineering strain (10P) and Y3PT_10P refers to a third-order Yeoh model (Y3) fitted to the planar tension (PT) characterisation data preconditioned to 10% engineering strain (10P).

Table 8 also lists the final displacements predicted by the three selected FEA simulations associated to the defined labels and compares them to the displacements measured in the first and second load sets of the experiment.

As described in Section 4.2, the elements are classified according to their average maximum principal strain which is retrieved from the results of a first FEA simulation. The elements are grouped according to their strain range as defined in Table 5. All elements within the same strain range are given the same hyperelastic model fitted to a characterisation curve preconditioned to a level of strain in accordance to Table 5. To remain consistent, all the hyperelastic models used in a given preconditioning iteration are fitted to the data from the same characterisation test.

Table 8: Hyperelastic models used in the first FEA simulation to be used in the preconditioning iteration

Label	Curve-fitting options			Final gauge displacement [mm]		
	Model order	State of strain	Preconditioning level (eng. strain)	FEA prediction	Load set 1	Load set 2
Y1ST_10P	First	Uniaxial	10%	34.6	30.0	32.6
Y1PT_10P	First	Planar	10%	30.1	30.0	32.6
Y3PT_10P	Third	Planar	10%	29.3	30.0	32.6

The classification of elements from the FEA results obtained with the hyperelastic models Y1ST_10P, Y1PT_10P and Y3PT_10P, from Table 8, is illustrated in Figs.50, 51 and 52, respectively. Since the final deformations from these results vary slightly, it is expected that the distribution of elements in the different strain ranges varies slightly as

well. As seen in Fig. 50, where the Y1ST_10P hyperelastic model was used in the first analysis, the preconditioning iteration classification associates 12 elements to the $0.06 < \bar{\varepsilon}_1 \leq 0.10$ strain range, indicating that these elements will be given a hyperelastic model fitted to the characterisation curves preconditioned to 15% engineering strain. In contrast, the preconditioning iteration classification, illustrated in Figs. 51 and 52, indicate that no elements from the FEA results obtained with the Y1PT_10P nor the Y3PT_10P hyperelastic models show maximum principal Hencky strains greater than $\bar{\varepsilon}_1 = 0.06$.

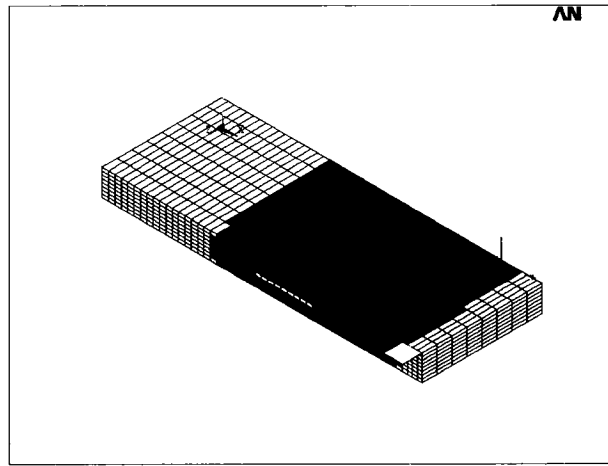


Fig. 50: Classification of elements according to their level of maximum principal strain for a simulation solved with the Y1ST_10P hyperelastic model. White: $0 < \bar{\varepsilon}_1 \leq 0.005$; light grey: $0.005 < \bar{\varepsilon}_1 \leq 0.03$; dark grey: $0.03 < \bar{\varepsilon}_1 \leq 0.06$; black: $0.06 < \bar{\varepsilon}_1 \leq 0.10$.

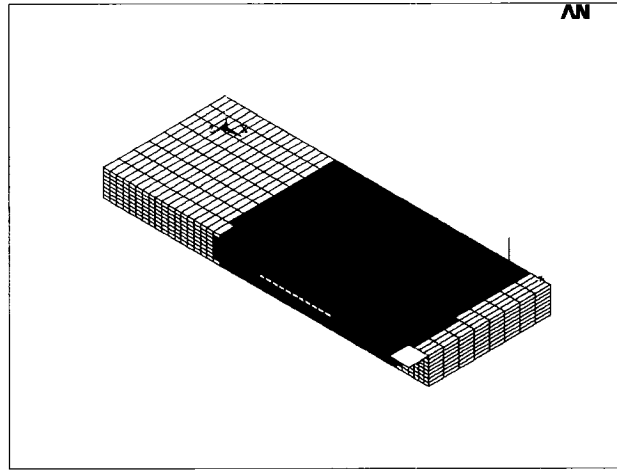


Fig. 51: Classification of elements according to their level of maximum principal strain for a simulation solved with the Y1PT_10P hyperelastic model. White: $0 < \bar{\epsilon}_1 \leq 0.005$; light grey: $0.005 < \bar{\epsilon}_1 \leq 0.03$; dark grey: $0.03 < \bar{\epsilon}_1 \leq 0.06$.

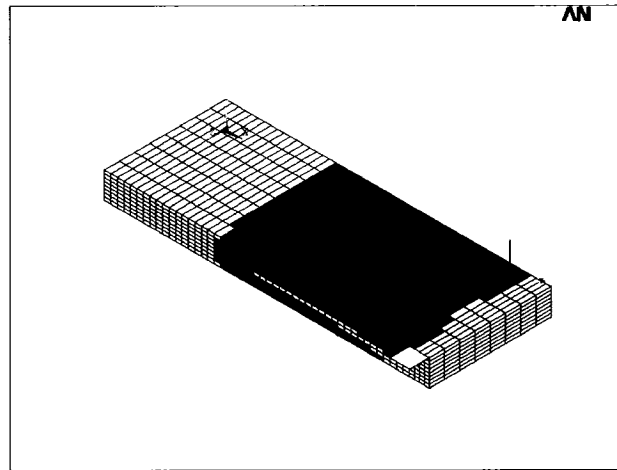


Fig. 52: Classification of elements according to their level of maximum principal strain for the simulation solved with the Y3PT_10P hyperelastic model. White: $0 < \bar{\epsilon}_1 \leq 0.005$; light grey: $0.005 < \bar{\epsilon}_1 \leq 0.03$; dark grey: $0.03 < \bar{\epsilon}_1 \leq 0.06$.

The load-displacement predictions shown in Fig. 53 are obtained from the preconditioning iteration with hyperelastic models fitted to the uniaxial tension characterisation data. The elements were classified prior to the second iteration according to the first FEA simulation solved with the Y1ST_10P, the Y1PT_10P and the

Y3PT_10P hyperelastic models as indicated in the figure. The preconditioning iteration is repeated in a similar fashion with hyperelastic models fitted to the planar tension and equi-biaxial extension data in Figs. 54 and 55 respectively. All three figures (Figs. 53, 54 and 55) seem to indicate that the choice of the first analysis (obtained with Y1ST_10P, Y1PT_10P or Y3PT_10P) has little influence on the results of the second iteration. On the other hand, the choice of characterisation data for the second iteration seems to play a more important role.

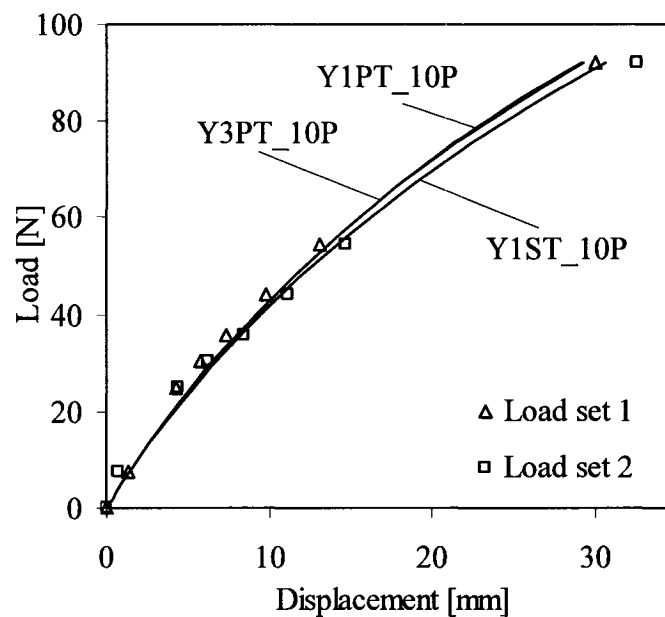


Fig. 53: Predictions from the preconditioning iteration with first-order Yeoh hyperelastic models fitted to the uniaxial characterisation data for the second iteration. The FEA predictions are identified according to the hyperelastic model used in the first analysis.

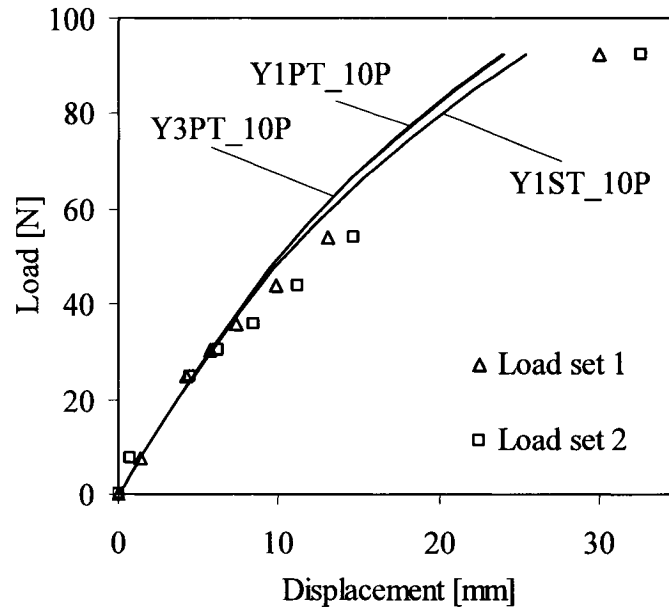


Fig. 54: Predictions from the preconditioning iteration with first-order Yeoh hyperelastic models fitted to the planar characterisation data for the second iteration. The FEA predictions are identified according to the hyperelastic model used in the first analysis.

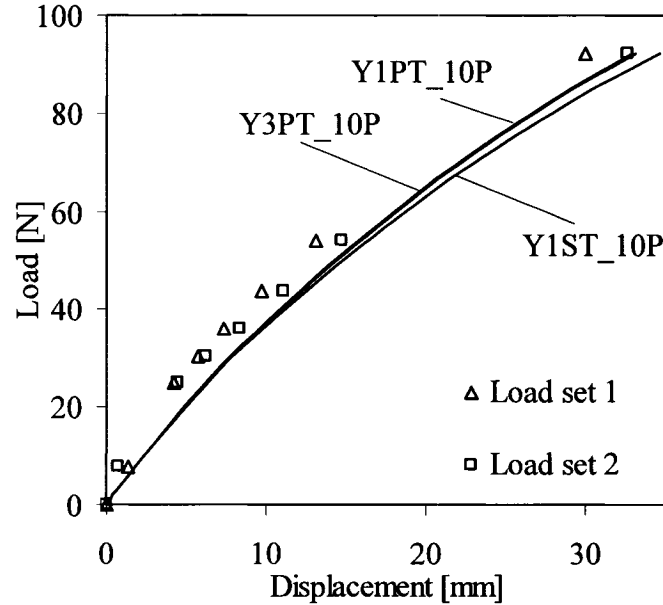


Fig. 55: Predictions from the preconditioning iteration with first-order Yeoh hyperelastic models fitted to the equi-biaxial characterisation data for the second iteration. The FEA predictions are identified according to the hyperelastic model used in the first analysis.

It may be observed that the FEA results predicted from the preconditioning iteration are the most accurate when the hyperelastic models used are fitted to the uniaxial characterisation data. This observation is evident when comparing the results obtained from the preconditioning iteration in the same figure, as done in Fig. 56. For the sake of the discussion, the elements in these preconditioning iterations were classified according to the results of the first analysis where the Y1PT_10P hyperelastic model is used. The preconditioning iteration with hyperelastic models fitted to the planar tension characterisation data shows a slightly stiffer response while the results obtained with the hyperelastic models fitted to the equi-biaxial characterisation data show a slightly softer response with respect to the experimental measurements. This is expected; a quick look at the first-order Yeoh coefficients in Table 2 shows stiffer models when fitted to planar data and softer models when fitted to equi-biaxial data (since the coefficients are proportional to the initial stiffness of the model, refer to Table 1, Section 2.3.).

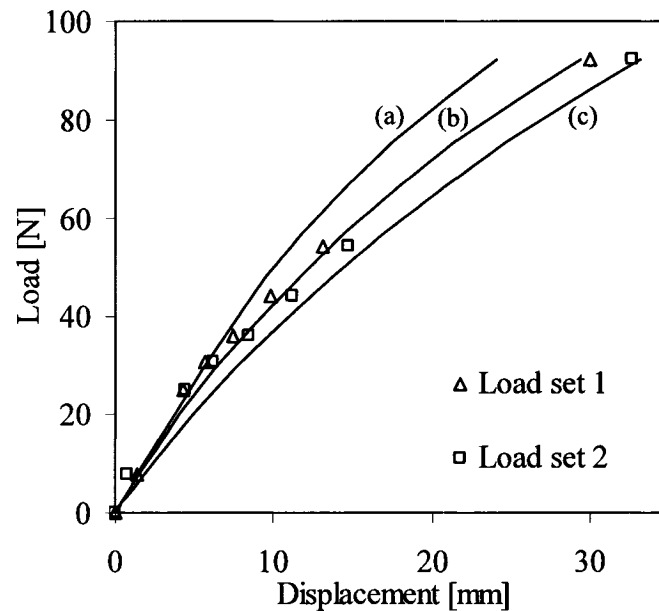


Fig. 56: FEA predictions following the preconditioning iteration where the elements were classified according to the strains from the first analysis with the Y1PT_10P hyperelastic model. The first-order Yeoh hyperelastic models used in the preconditioning (second) iteration were fitted to the (a) planar tension, (b) uniaxial tension and (c) equi-biaxial extension characterisation data.

The accuracy of the results obtained with first-order Yeoh models in the preconditioning iteration indicates that the third-order Yeoh hyperelastic formulation is not necessary to capture the nonlinear response of the system. Simply capturing the softening of the material due to preconditioning effects, even if the local nonlinearity at different preconditioning levels is not fully captured with a first-order hyperelastic model, proves to be enough to predict the nonlinear response of the bending cantilevered plate.

5.2.4. Biaxiality test applied to the bending cantilevered plate

The biaxiality test is meant to be conducted on the results of a FEA simulation in order to provide information on the dominant state(s) of simple strain in the analysis. To remain consistent with the previous section (preconditioning iteration), the biaxiality test will be performed on the results of the simulations obtained using the Y1ST_10P, Y1PT_10P and Y3PT_10P hyperelastic models^{†††}. The biaxiality ratio of every element may be determined by post-processing the results of the selected simulations. The elements are then classified into the three regions of dominant deformation, as defined in Table 6 from Section 4.3; a region of dominant uniaxial extension between α_{U-P} and α_U , a region of planar deformation between α_{B-P} and α_{U-P} , and a region of equi-biaxial extension between α_B and α_{B-P} .

The elements that are between the clamped surfaces barely deform at all during the analysis and contribute very little to the results. Furthermore, the biaxiality ratios obtained from these elements are likely to be incorrect due to their possibly high ratio (>5%) of artificial energy to internal energy induced by the hourglass stiffness factor, as discussed in Section 5.2.1. and even earlier in Section 4.1.2. Therefore, the biaxiality ratios of the elements between the clamped surfaces minus the first row^{†††}, as shown in Fig. 57, will be neglected, i.e. 2120 of the 3264 elements are considered for the biaxiality test.

^{†††} As defined in Table 8.

^{†††} A row of elements between the clamping surfaces, along the width of the plate, is kept in the biaxiality test since they are likely to have non-negligible levels of strain.

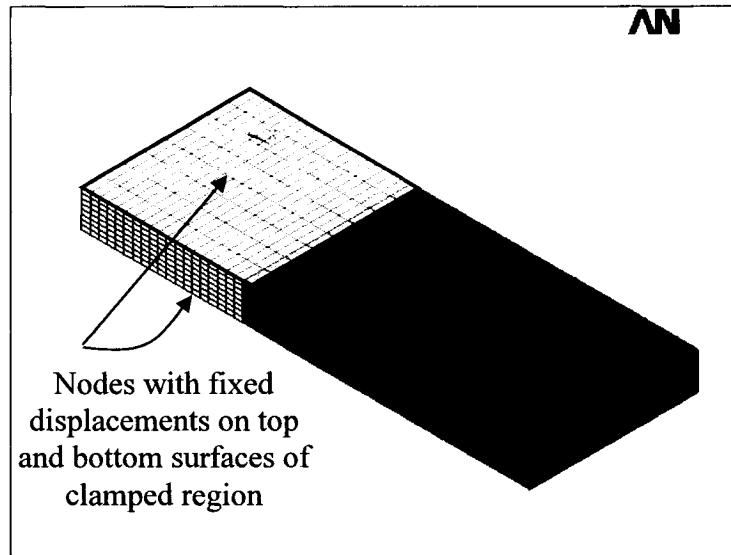


Fig. 57: The elements not between the clamped surfaces plus the first row under the clamped surfaces (shown in grey) are submitted to the biaxiality test. The elements in white are neglected in the biaxiality test.

The biaxiality test was performed on the FEA results for different loads and thus different displacements. The distribution of the elements in the three regions of dominant deformation as the gauge displacement increases is shown in Fig. 58. The plate was loaded beyond the deformation measured in the experiments, simply to see if and how the distribution changed at higher displacement. These results were obtained with a first-order Yeoh hyperelastic model fitted to the planar characterisation data preconditioned to 10% engineering strain. Fig. 58 shows very little change in the distribution of elements in the three regions of dominant deformation as the plate bends.

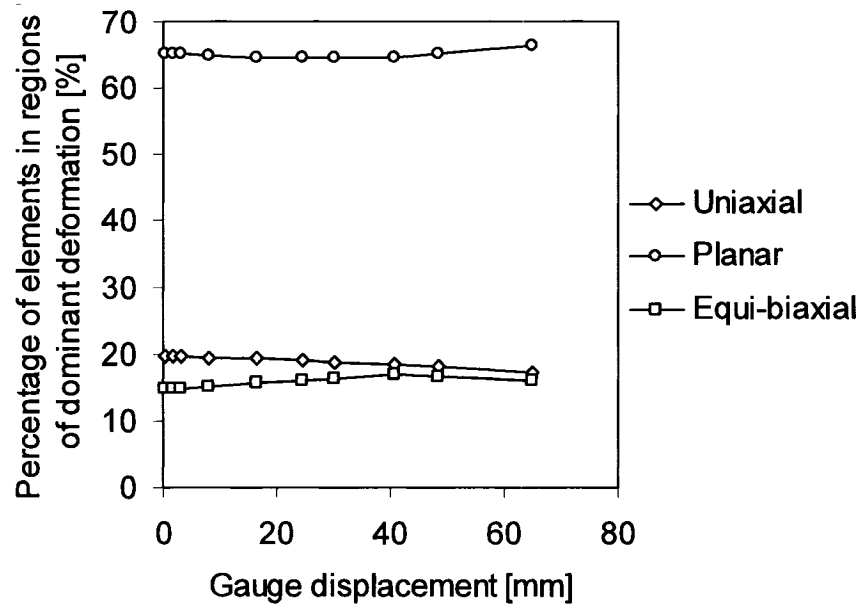


Fig. 58: Distribution of elements in the three regions of dominant deformation defined in the biaxiality test as a function of the predicted gauge displacement. These results were obtained with a first-order Yeoh hyperelastic model fitted to the planar characterisation data preconditioned to 10% engineering strain.

The distribution of elements predicted by the biaxiality test in the three regions of dominant deformation obtained with the three different hyperelastic models used is listed in Table 9. It is seen in this table that these distributions change very little from one hyperelastic model to the next.

If the plate was infinitely wide, all deformations would be expected to be planar and thus the biaxiality ratios of every element would equal to α_p . But when considering a plate of finite width, regions of dominantly uniaxial (above neutral axis) and dominantly equi-biaxial (below neutral axis) extension will appear near the ends, as shown in Fig. 59.

Table 9: Distribution of elements in the three regions of dominant deformation determined by the biaxiality test

Hyperelastic models (labels defined in Table 8)	FEA gauge displacement [mm]	Number of elements in regions of dominant deformation [%]		
		Uniaxial	Planar	Equi-biaxial
Y1ST_10P	34.6	19	65	16
Y1PT_10P	30.1	19	65	16
Y3PT_10P	29.3	20	64	16

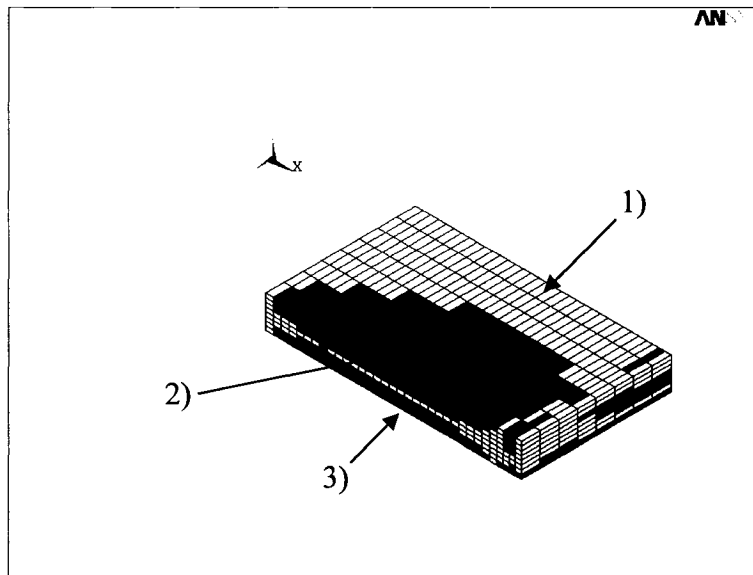


Fig. 59: Distribution of elements in the regions of dominant strain shown on the symmetrical half of the cantilevered plate subjected to a bending load at its free end; 1) region of dominantly planar deformations, 2) region of dominantly uniaxial deformation and 3) region of dominantly equi-biaxial deformation. A first-order Yeoh hyperelastic model was used fitted to the planar characterisation data preconditioned to 10% engineering strain.

The FEA predictions from the preconditioning iteration are all very close (within 10% of the experimental measurements) regardless of the simple state of strain the models are fitted to, as seen in Figs. 53, 54 and 55; nonetheless, the predictions with the hyperelastic models fitted to uniaxial data are perhaps the best in this particular case.

While the biaxiality test indicates that the majority of the elements in this analysis are in the region of dominant planar deformation, the hyperelastic models obtained with the planar tension data are the stiffest (refer to Table 2). No hyperelastic model can precisely represent all states of strain simultaneously; for a given level of preconditioning the fit to planar data is stiffest, the fit to biaxial data is softest, and the fit to uniaxial data is in-between. Using the uniaxial data to fit the hyperelastic models for the preconditioning iteration in simulations where all three states of dominant deformation (defined by the biaxiality ratio) are present may be the best compromise. Maybe if the plate were made much wider (such as to approach a state of plane strain, with negligible side effects) the preconditioning iteration fitted to planar data would provide a better prediction.

One may argue that even better agreement may be obtained if each dominant region of strain had hyperelastic models fitted to the corresponding characterisation data. In other words, the elements in the region of dominant uniaxial deformation would be fitted to the uniaxial tension characterisation data, the elements in the region of dominantly planar deformation would be fitted to the planar tension characterisation data, and the elements in the region of dominantly biaxial deformation would similarly be fitted to the equibiaxial extension characterisation data. On the other hand, characterising rubber in three states of simple stress can be very expensive. A cost-savings alternative would be to use only one characterisation test in a FEA simulation to predict the behaviour of the material, in which case the work presented herein provides a reference on how to choose the appropriate characterisation test for a given analysis.

Chapter 6: Transverse Deflection of a Guide Lug

This chapter addresses the elastic behaviour of a standard rubber guide lug subjected to a transverse load. While the problem of the bending cantilevered plate may be considered simple, that of a guide lug subjected to a deflection load is slightly more complex. Tension, compression and shear are expected to be present, but it is more difficult to anticipate where exactly. Furthermore, the deformation of a guide lug is a problem more likely to be encountered in an industrial context.

Rubber tracks are widely used in the power-sports (e.g. snowmobiles) and agricultural (e.g. tracked vehicles made by Caterpillar, John Deere or AGCO) industries; they can also be found in municipal (e.g. sidewalk snow removal vehicles namely used in Montreal) and alpine (e.g. trail grooming) applications. Tracks are usually sprocket-driven or friction-driven. Sprocket-driven tracks are similar to gear mechanisms; a sprocket engages rubber drive lugs on the inner side of the track. On the other hand, friction-driven tracks rely strictly on the friction between a smooth metal cylinder and the inner surface of a rubber track.

Tracks may be subjected to transverse loads that would potentially cause them to derail from the vehicle. While the drive lugs of a sprocket-driven track may also be used to prevent derailment, rubber guide lugs on the inner side of friction-driven tracks are often present, simply to ensure the track stays in place.

Experiments were conducted on a rubber guide lug made of the same rubber that was characterised previously. FEA simulations of the guide lug were performed and their predictions are compared to the experiments. The preconditioning iteration and biaxiality test are also applied to this problem.

Although (drive or guide) lugs are rarely reinforced with other materials, rubber tracks are often reinforced in the mid-layer, a.k.a. carcass, between the lugs and the treads (“ribbed” or “toothed” surface that is shaped to grip the ground). Since only the rubber

behaviour is of interest in this work, the experiments to be described were conducted on guide lugs with no reinforced carcass.

6.1. Experimental bench-test

A description of the experimental set-up used to apply a transverse deflection load to a guide lug is presented herein. The experimental results are then given and briefly discussed.

6.1.1. Experimental set-up

The test-section comprised the inner side of a track with several guide lugs. A top view of the experimental set-up is illustrated in Fig. 60. The specimen was clamped down on either side of the tested guide lug by two metal plates. The two metal plates were held down by two metal bars.

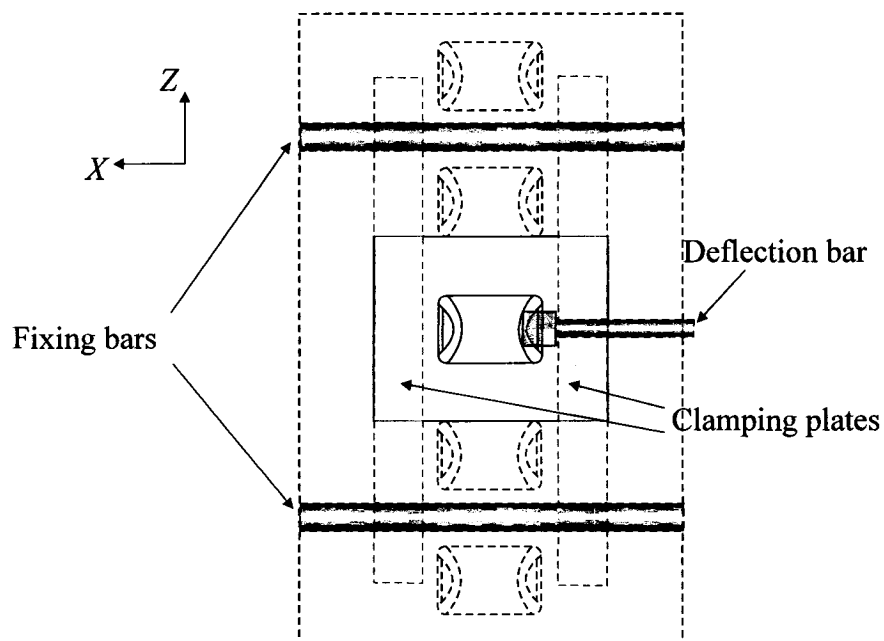


Fig. 60 : Illustration of the experimental set-up for the guide lug deflection test. The dashed lines (---) delimit components that are not directly represented in the FEA model. The continuous lines (—) delimit the geometry that is modelled in the finite element analysis. Note that this illustration is not necessarily to scale.

The geometry of the guide lug is described in more detail in Fig. 61 and the corresponding dimensions are listed in Table 10. The geometry described in Fig. 61 and Table 10 also is the geometry used in the FEA model.

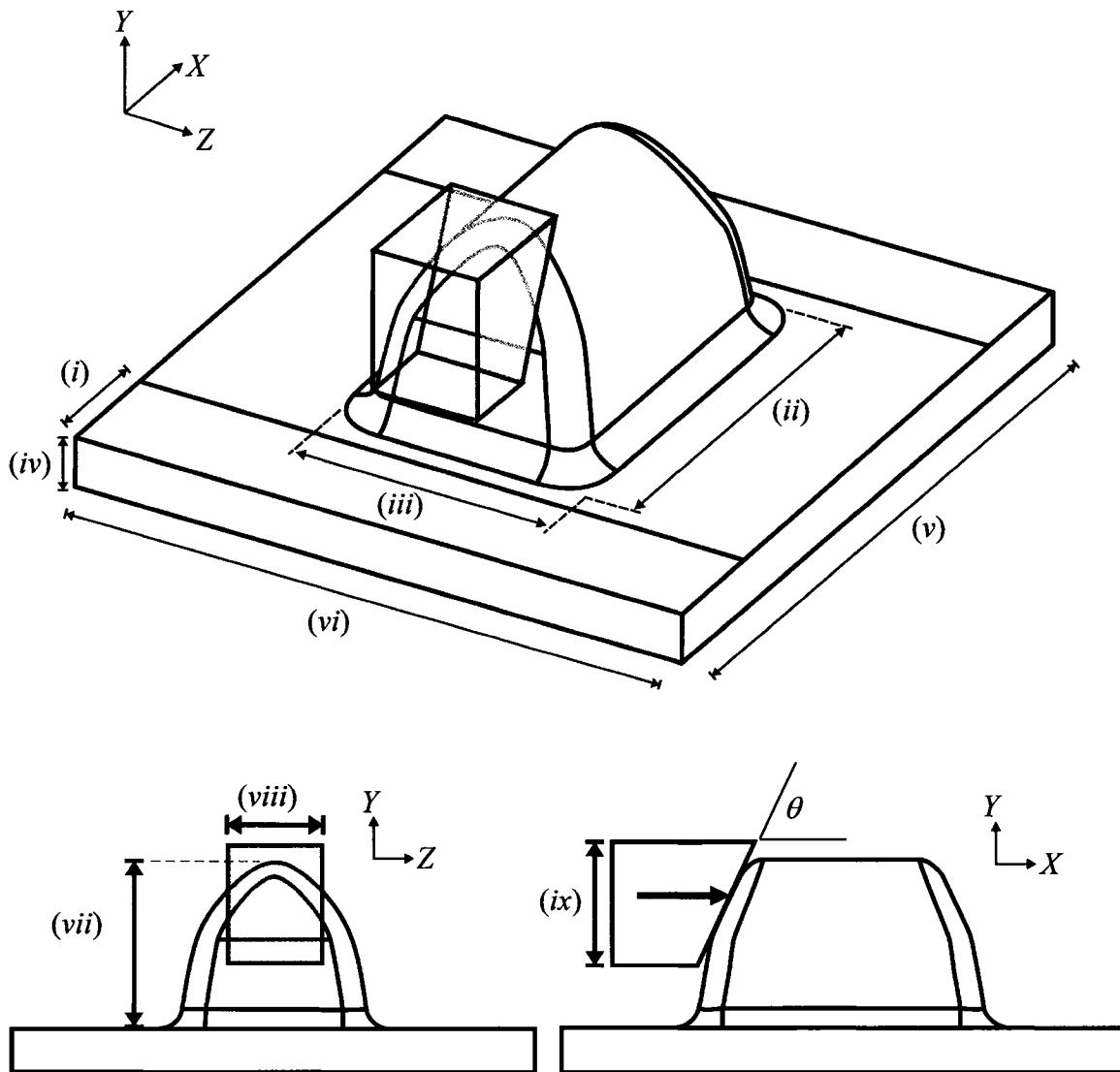


Fig. 61: Schematic representation of the guide lug and pushing block used to deflect the guide lug transversally (X-direction). The labelled dimensions are defined in Table 10.

Table 10 : Guide lug dimensions as labelled in Fig. 61

(i) Clamping width	50.40 mm
(ii) Guide lug length	175.6 mm
(iii) Guide lug width	123.3 mm
(iv) Base thickness	23.18 mm
(v) Base length	181.5 mm
(vi) Base width	195.9 mm
(vii) Guide lug height	88.90 mm
(viii) Deflection bar width	50.80 mm
(ix) Deflection bar height	63.50 mm
Deflection bar angle, θ	65°

The experimental procedure consisted of applying an incremental transverse deflection to the guide lug through a *deflection bar*, as shown in Figs. 60 and 61. A load cell allowed the reading of the reaction force on the deflection bar. Displacement gauges were used to measure the displacement of the deflection bar and of the opposite side of the guide lug, as shown in Fig. 62. A few other displacement gauges were positioned around the bench test to ensure the assumptions made to simplify the FEA model would hold.

Here the displacement imposed by the deflection bar was constant and the resulting reaction force was measured with the load cell. Therefore, rather than creep effects, relaxation effects were observed. In other words, the readings on the displacement gauges would remain constant immediately after a displacement increment, while the load cell indicated a continuous change in the reading of the reaction force on the deflection bar immediately after a displacement was imposed. Two-minute intervals were taken between the displacement increments before measuring the corresponding

load, in order to let relaxation effects take place. The displacement increments were assumed small enough to approximate quasi-static loading.

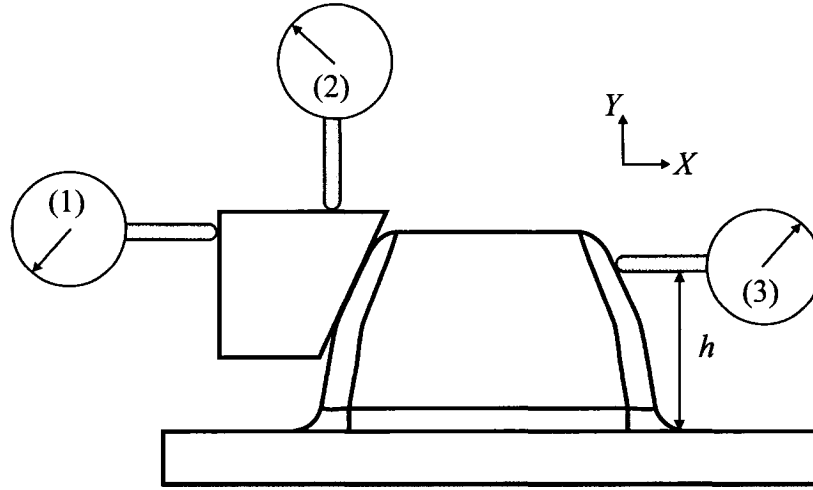


Fig. 62: Position of the displacement gauges used in the guide lug deflection experiments. Displacement gauge (1) measured the X -direction displacement of the deflection bar while displacement gauge (2) measured its displacement in the Y -direction. Displacement gauge (3) measured the X -direction displacement of the side of the guide lug opposite to the deflection bar. Displacement gauge (3) was centered in Z with respect to the guide lug geometry and positioned at a height $h = 71$ mm from the base of the guide lug.

6.1.2. Results from experimental tests

Each “load cycle” consisted of applying incremental displacements to the deflection bar until the desired transverse displacement was obtained. The unloading was not recorded in these experiments. The relaxation effects were not recorded either, only the reaction force value two minutes after each displacement increment was imposed. The displacement gauges and load cell were zeroed after each load cycle. Four transverse deflection load cycles were performed on the guide lug. The load measured at the load cell is plotted against the horizontal displacement of the deflection bar for each cycle in Fig. 63.

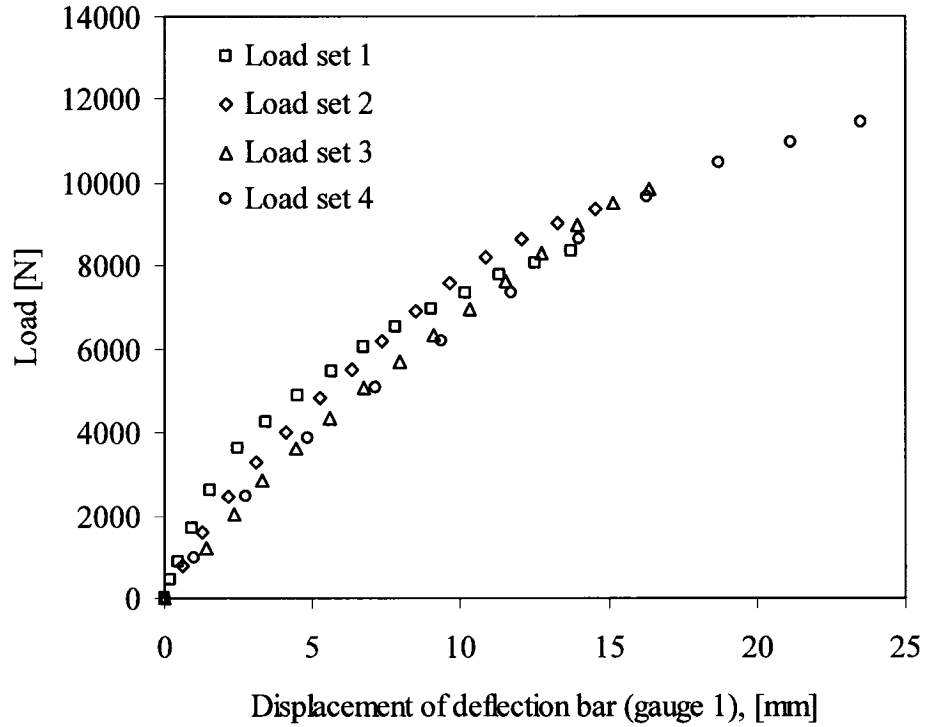


Fig. 63: Experimental results showing the load-displacement path of the deflection bar for the 1st, 2nd, 3rd, and 4th loading cycles (no unloading recorded).

It is worth mentioning that the relaxation effects were important; the two-minute interval taken following each displacement increment before reading the load cell was determined arbitrarily. A compromise had to be made between pressing on with the experiment without excessive delay and letting relaxation effects take place. The two-minute interval seemed like an appropriate compromise. Immediately following each displacement increment, the load cell would show a high rate of change, i.e. a high rate of relaxation, making it practically impossible to accurately read a value of load. By the end of the two minutes, the relaxation rate had slowed down to the point of being barely perceptible on the load cell.

The vertical displacement of the deflection bar, measured with the second displacement gauge, is plotted against its horizontal displacement in Fig. 64. This vertical displacement is attributed to the bending of the deflection bar as it is applying load to the

guide lug. Load sets 1 and 2 seem to follow the same, nearly linear, vertical versus horizontal displacement path, while load sets 3 and 4 have a slightly different, yet still nearly linear, path. This difference could be due to rearrangements in the experimental set up between load set 2 and 3.

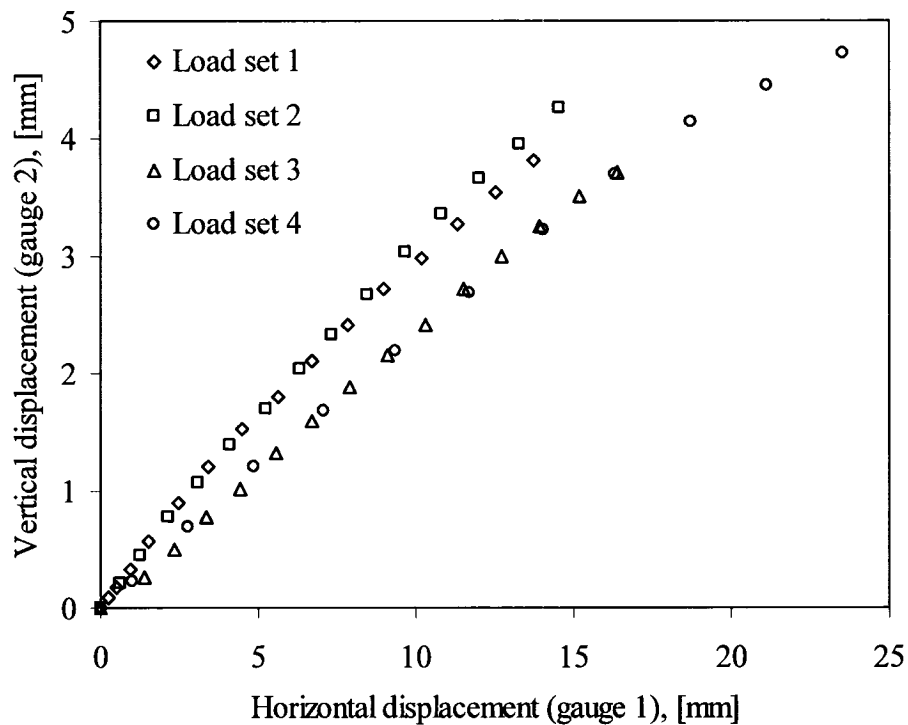


Fig. 64: Vertical (gauge 2) vs. horizontal (gauge 1) displacement of the deflection bar.

The displacement of the opposite end of the guide lug was also monitored with a third displacement gauge, the results of which are presented in Fig. 65. These measurements are quite linear as well and seem to follow the same path from one load set to the next.

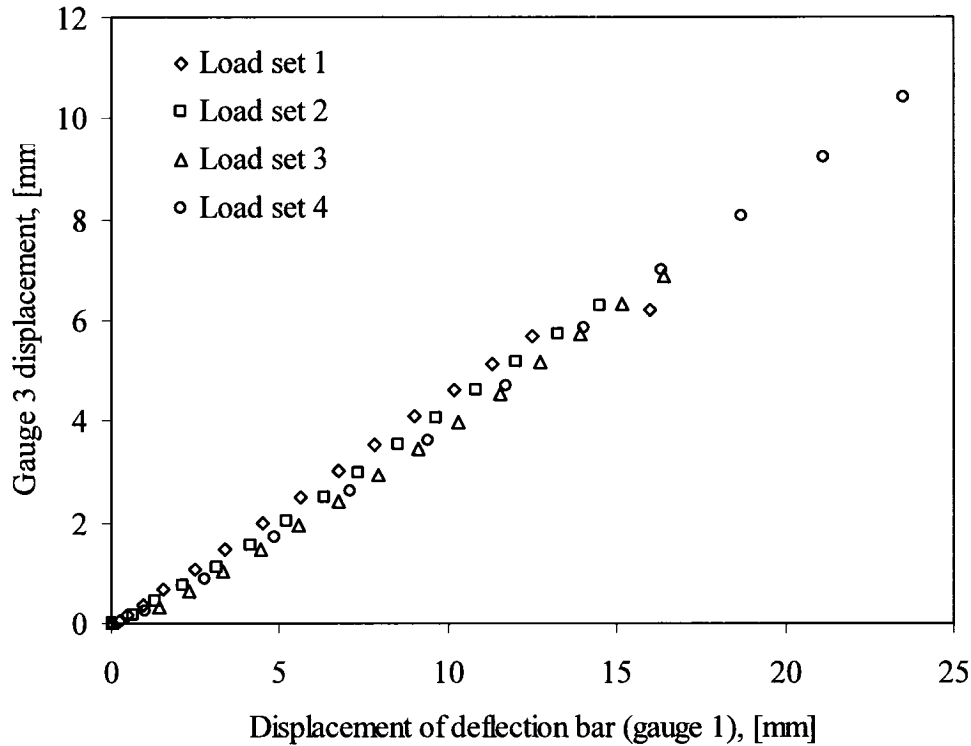


Fig. 65: Displacement measured at the third displacement gauge (from Fig. 62) vs. the horizontal displacement of the deflection block (second displacement gauge).

6.2. Finite Element Simulations

This section describes how the finite element model was built. Results with hyperelastic models fitted to a single state of simple strain are presented first. The biaxiality test and the preconditioning iteration are then applied to the simulation. The FEA results with and without the preconditioning iteration are compared to the experimental results.

6.2.1. Finite element simulation problem definition

As mentioned in the previous section, the geometry for the finite element model is based on that shown in Fig. 61 with parameter details in Table 10.

SOLID187 quadratic tetrahedral elements, available in ANSYS™ 8.0 and later versions, were used to mesh the guide lug geometry in this FEA model. The symmetrical half of the meshed guide lug with its boundary conditions is shown in Fig. 66(a) and Fig. 66(b).

The nodes on the top surfaces, indicated as fixed supports in the figure, are fixed in all degrees of freedom to simulate the clamping condition from the experiment. A symmetry face is determined in the XY -plane at the centre of the guide lug in the Z -direction. This symmetry plane is implemented in the FEA model to reduce computation time. The surface of the deflection bar that is in contact with the guide lug is modelled with a rigid contact in ANSYS™. The displacement of the deflection bar is controlled by a pilot node; one single node controls the displacements of all the other nodes in the rigid contact element. Using a pilot node facilitates the retrieval of reaction forces when post-processing the results.

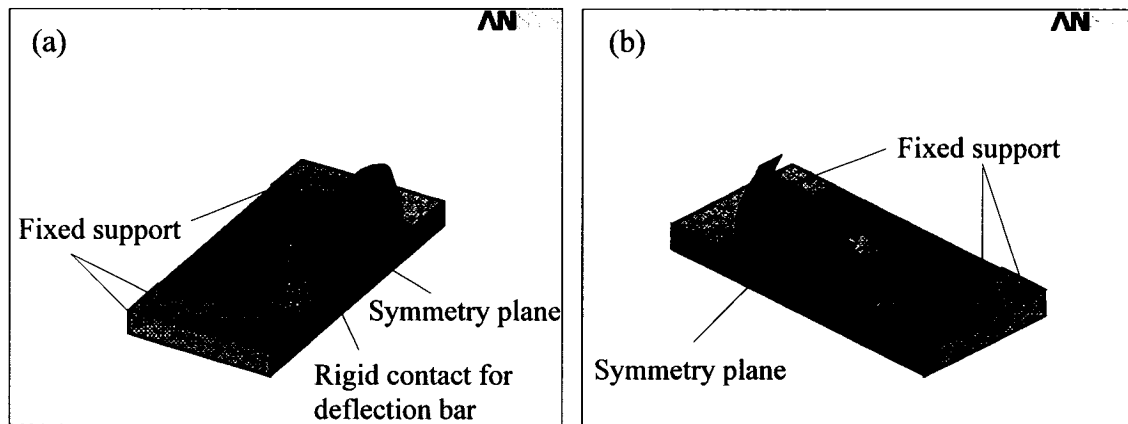


Fig. 66: Meshed guide lug and boundary conditions applied to designated faces.

A displacement is applied to the pilot node that controls the position of the rigid contact modelling the deflection bar and the corresponding reaction force is calculated. The fixed displacement includes a horizontal and vertical components resulting from a linear approximation of the measurements shown in Fig. 64. FEA simulations are conducted for the second, third and fourth load steps. The first experimental load step is not compared to FEA predictions, since in this load set the material still seems to be in the process of being preconditioned.

A contact node is used to simulate displacement gauge 2 (refer to Fig. 62); it is free to slide without friction on the surface of the guide lug and free to move in the X -direction but its displacement is fixed in the Y - and Z -directions. Its X -displacement is monitored

and thus provides a measurement similar to that read by the experimental gauge. It is emphasized that it is constrained to move in a single axis while remaining in contact with the guide lug, yet it does not interfere with the deflection of the guide lug.

A global element size of 18 mm was used in the FEA results presented here with a total of 4907 10-noded tetrahedral elements. The size of the guide lug elements near the contact surface of the displacement block were reduced to one third of the global element size for the model. The global element size of the model was determined with a convergence test similar to the one in the previous chapter. The analysis is run with different element sizes and the final predicted loads for the imposed displacement for each simulation are compared. Fig. 67 shows the final resulting force in the *X*-direction applied by the displacement block with respect to the element size. This convergence test was performed with a first-order Yeoh hyperelastic model fitted to the planar characterization data preconditioned to 10% engineering strain. The accuracy of the predicted load with respect to the experimental results is not considered here.^{§§§} It is observed that, while the load predicted may not seem to converge as nicely as it did for the bending plate analysis, the change in load prediction from one mesh refinement to the next always remains small and is therefore acceptable.

Stress concentrations are expected to occur on the surface of the guide lug in contact with the edges of the displacement block. Although refining the mesh often leads to improved results in FEA simulations, refining the mesh near areas with stress concentration can lead to the opposite effect and may even cause divergence of the solution. It is often acceptable to leave a coarser mesh near stress concentrations, particularly if they do not affect the results of interest in the analysis. A global element size of 18 mm was chosen in order to have a mesh that is refined enough while remaining computationally efficient. The refinement at the surfaces in contact with the deflection bar was determined also to improve the accuracy of the results without encountering divergence issues likely due to stress concentrations.

^{§§§} The element size convergence depends only a converging load from one element refinement to the next. The FEA predictions will be compared to the experimental data in Sections 6.2.2 and 6.2.3.

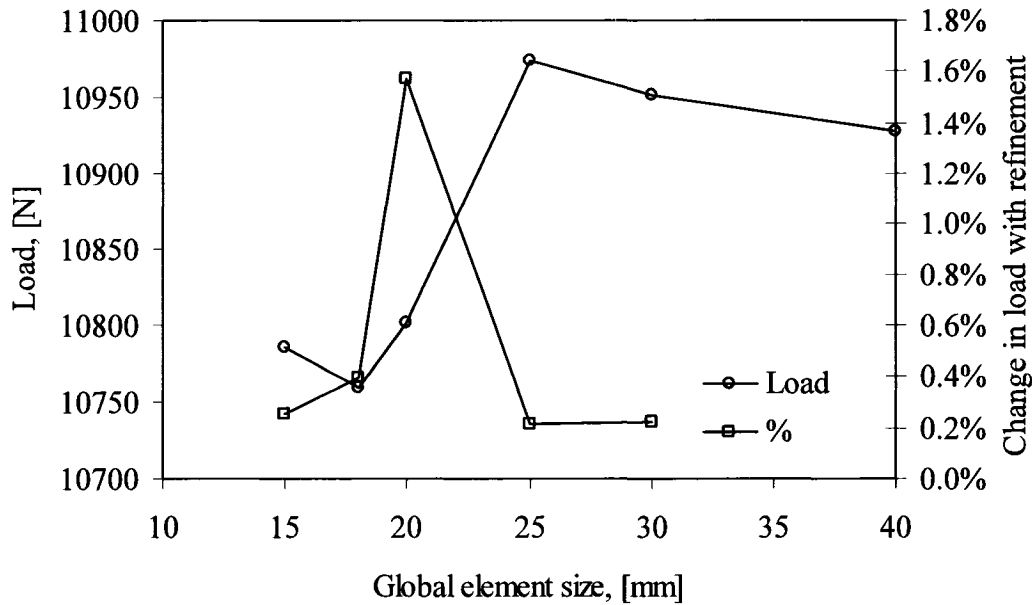


Fig. 67: Effect of refining the mesh in the FEA of the bending cantilevered plate modelled here with a first-order Yeoh hyperelastic model fitted to the planar characterisation data preconditioned to 10% engineering strain. Note that the percent change in load was calculated starting with the results from a global element size of 40 mm.

6.2.2. FEA results using a single hyperelastic model for the rubber

The displacement of the deflection bar along with its reaction force is retrieved from every substep in order to provide a force-displacement path. The substeps are controlled, obviously to allow the solution to converge, but also to keep track of the load history of the guide lug.

FEA results obtained using a first-order Yeoh model fitted to uniaxial characterization data preconditioned to 5% engineering strain as well as a third-order Yeoh model fitted to planar characterization data preconditioned to 10% engineering strain are shown in Fig. 68. The FEA prediction with the first-order hyperelastic model shows a response that slightly stiffens as the deflection increases. This type of response is expected for any analysis performed with a first-order Yeoh hyperelastic model; changing the coefficient

would simply change the initial slope of the response curve. The FEA prediction with the third-order Yeoh hyperelastic model shows sudden stiffening to excessive loads several orders of magnitude greater than the load measured in experiment (not shown in the figure for visual scaling purposes). The use of any other third-order Yeoh hyperelastic model would have a similar qualitative behaviour. In either case (first- or third-order hyperelastic models), there is no qualitative agreement with the experimental measurements.

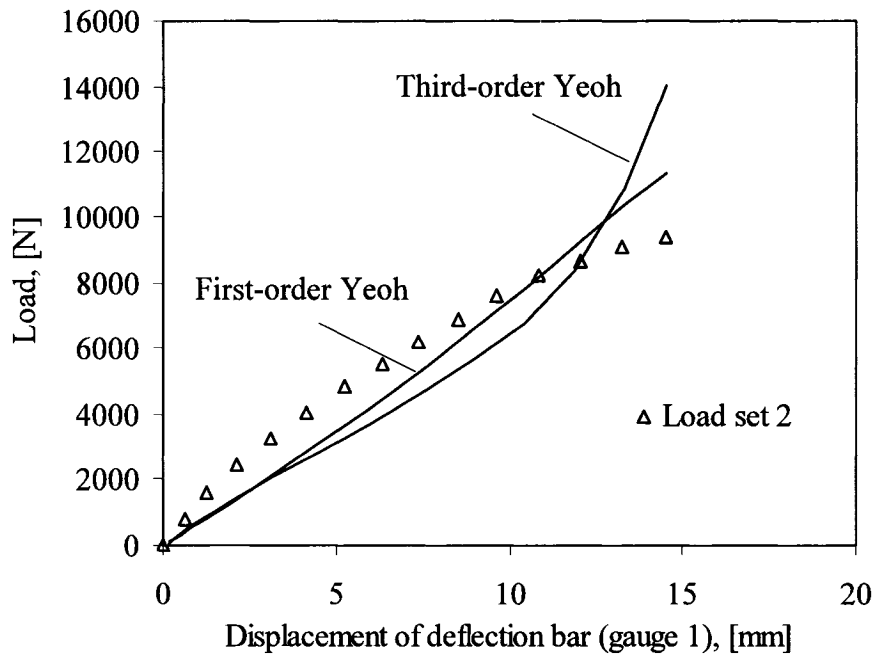


Fig. 68: Load-displacement predictions from the FEA model of the deflection of a guide lug compared to the experimental measurements. The first-order Yeoh model was fitted to uniaxial characterization data preconditioned to 5% engineering strain while the third-order Yeoh model fitted to planar characterization data preconditioned to 10% engineering strain.

6.2.3. Preconditioning macro applied to the bending cantilevered plate

The preconditioning iteration is applied next to the results of selected FEA simulations obtained with a single hyperelastic model. The average maximum principal Hencky strain of every element is retrieved and the elements are grouped according to the ranges defined in Table 5 of Section 4.2. Each group of elements within a given range are attributed the same hyperelastic model fitted to a preconditioned curve again as defined in

Table 5 of Section 4.2. Distributions of the different strain ranges are provided in Fig. 69, these are sensibly the same, regardless of the first-order hyperelastic model used in the first analysis.

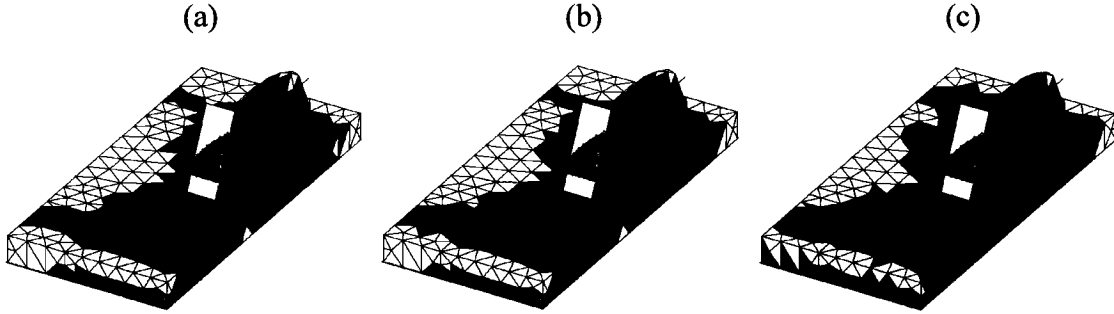


Fig. 69: Classification of elements according to their level of maximum principal strain for (a) load set 1, (b) load set 2, (c) load set 3. White: $0 < \bar{\epsilon}_1 \leq 0.005$; light grey: $0.005 < \bar{\epsilon}_1 \leq 0.03$; grey: $0.03 < \bar{\epsilon}_1 \leq 0.06$; dark grey: $0.06 < \bar{\epsilon}_1 \leq 0.10$; black: $\bar{\epsilon}_1 > 0.10$.

The load-displacement paths obtained with the preconditioning iteration are shown in Figs. 70, 71 and 72, for load sets 2, 3 and 4, respectively. The most important observation to be made here is the drastic improvement in qualitative and quantitative predictions of the preconditioning iteration with respect to the experimental measurements, as opposed to the results obtained with a single hyperelastic model. Therefore modelling the effect of preconditioning is critical in this particular analysis.

The preconditioning iteration seems to best predict the experimental measurements of load set 2 when the first-order Yeoh hyperelastic model is fitted to the planar characterisation data. On the other hand, experimental load sets 3 and 4 are best predicted when the first-order Yeoh hyperelastic model is fitted to the uniaxial characterisation data. This again, raises unanswered questions with respect to the conclusions that can be reached from the biaxiality test.

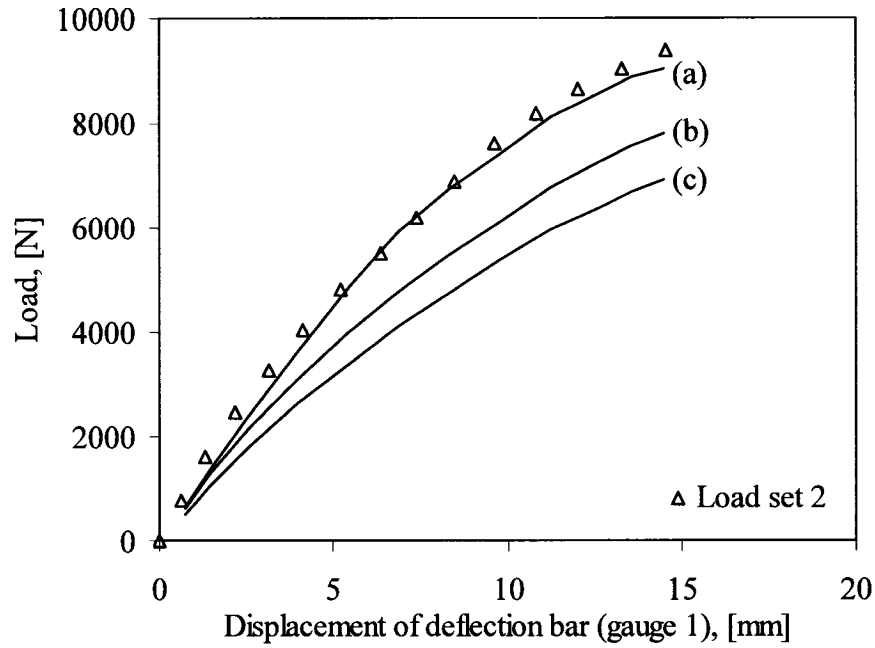


Fig. 70: Load-displacement path for load set 2 from the preconditioning iteration with first-order Yeoh models fitted to (a) planar tension data, (b) uniaxial tension data, and (c) equi-biaxial extension data, for the second iteration.

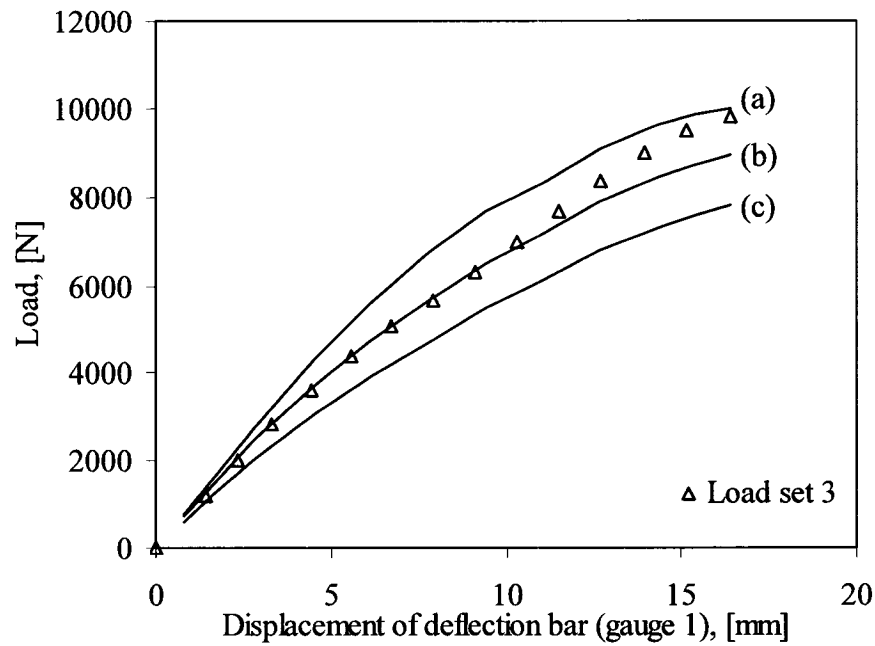


Fig. 71: Load-displacement path for load set 3 from the preconditioning iteration with first-order Yeoh models fitted to (a) planar tension data, (b) uniaxial tension data, and (c) equi-biaxial extension data, for the second iteration.

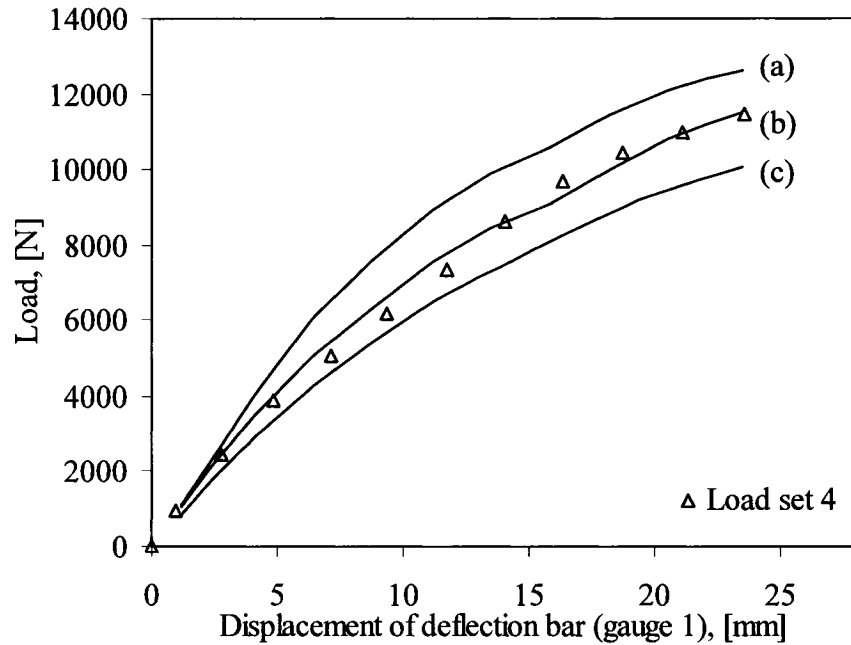


Fig. 72: Load-displacement path for load set 4 from the preconditioning iteration with first-order Yeoh models fitted to (a) planar tension data, (b) uniaxial tension data, and (c) equi-biaxial extension data, for the second iteration.

6.2.4. Biaxiality test applied to the deflecting guide lug problem

The biaxiality test is conducted on the results of selected FEA simulations used in Section 6.2.2. 3810 of the 4907 elements of the guide lug model are considered for the biaxiality test, as shown in Fig. 73, in an attempt to capture a more relevant distribution of elements in the regions of dominant deformation, since these elements will undergo the most strain.

The fact that displacements are imposed as boundary conditions allows for a more thorough comparison of the distribution of elements in the dominant regions of deformation defined by the biaxiality test for different hyperelastic models. It was observed that the biaxiality test distributes the elements in the exact same way when the FEA results are obtained with a first-order Yeoh hyperelastic model, regardless of the characterisation data it is fit to, provided the imposed displacement remains consistent.

Table 11 lists the different distributions of the biaxiality test obtained from FEA simulations with first-order Yeoh models for the different load sets from the experiments.

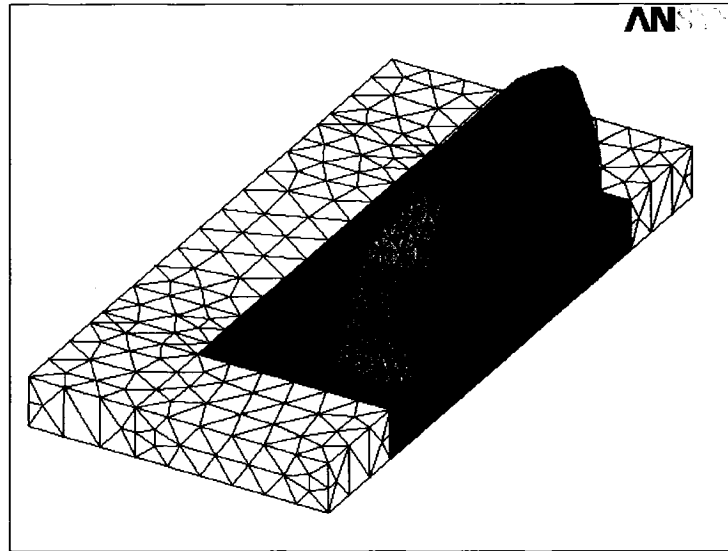


Fig. 73: 3810 elements (in grey) of the 4907 elements in the model are considered for the biaxiality test.

Table 11: Percentage distribution of elements in the three regions of dominant deformation defined by the biaxiality ratio when the FEA simulation is conducted with first-order Yeoh models

Load set	Number of elements in regions of dominant deformation [%]		
	Uniaxial	Planar	Equi-biaxial
2	17	31	52
3	16	31	53
4	16	31	53

Fig. 74 provides a view of the distribution of the elements in the regions of dominant deformation. Visually, there is very little change in the biaxiality test distributions from one load set to the next.

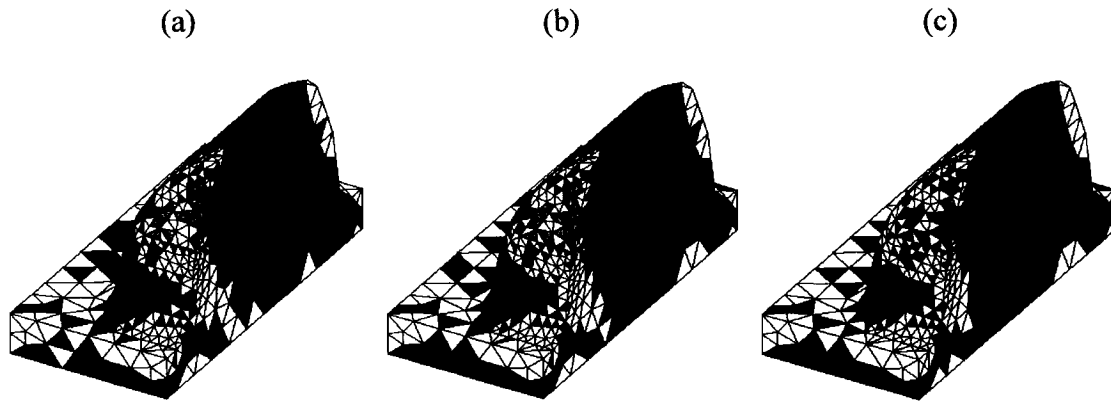


Fig. 74: Distribution of elements in the regions of dominant deformation for (a) load set 1, (b) load set 2 and (c) load set 3. Black: Region of dominant uniaxial tension; white: Region of dominant planar tension; grey: Region of dominant equi-biaxial tension.

On the other hand, the distribution of elements obtained by applying the biaxiality test to the results of FEA simulations with third-order Yeoh hyperelastic models changes, albeit very little, when fitted to different characterisation data curves. Some of these distributions are compared in Table 12. While slightly different from the distributions obtained with the first-order Yeoh models, again, there is no major change in regions of dominant deformation.

Fig. 75 provides a visualisation of the evolution, from load set 2 through 4, of the distribution of elements in the three regions of dominant deformation defined by the biaxiality test, applied here to the FEA results obtained with a third-order Yeoh model fitted to planar characterisation data preconditioned to 10% engineering strain. While the distribution of elements in the regions of dominant deformation varies little from a first-order Yeoh model to a third-order Yeoh model, there is a distinctive difference between the visual distribution, when comparing Fig. 74 and Fig. 75. The distribution of elements in Fig. 75 seems more distinctive as opposed to many scattered elements from different regions of dominant deformation in Fig. 74.

Table 12: Percentage distribution of elements in the three regions of dominant deformation defined by the biaxiality ratio when the FEA simulation is conducted with third-order Yeoh models

Third-order Yeoh curve-fitting options		Applied load set	Dominant regions [%]		
State of strain	Preconditioning level (eng. strain)		Uniaxial	Planar	Equi-biaxial
Planar	10%	2	20	31	49
Planar	10%	3	29	29	42
Uniaxial	10%	4	21	27	52
Planar	10%	4	21	27	52
Equi-biaxial	10%	4	18	30	52

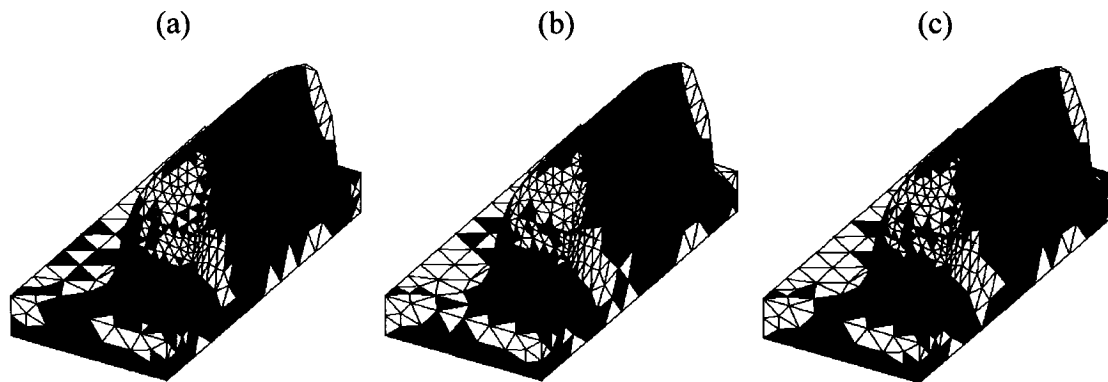


Fig. 75: Distribution of elements in the regions of dominant deformation obtained with third-order Yeoh hyperelastic models fitted to planar characterisation data preconditioned to 10% for (a) load set 1, (b) load set 2 and (c) load set 3. Black: Region of dominant uniaxial tension; white: Region of dominant planar tension; grey: Region of dominant equi-biaxial tension.

While the majority of elements in this analysis (deflection of the guide lug) are in the region of dominant equi-biaxial deformation, the other two regions of dominant deformation (uniaxial and planar) are definitely present and arguably in regions where there is higher strain. It is noted that the region of largest deformation ($\bar{\epsilon}_1 > 0.10$) in Fig. 69 in the previous section, in the area below the contact with the deflection bar, coincides

with the region of dominantly uniaxial tension seen in Fig. 74 or Fig. 75. Following a similar reasoning as in Section 5.2.4, it is proposed that applying the preconditioning iteration with hyperelastic models fitted to the uniaxial tension data would provide the best compromise capable of capturing the behaviour of the rubber in an analysis sharing all three regions of dominant deformation.

With this knowledge now in mind, it would have been possible to save on characterisation costs by only testing the rubber in uniaxial tension. On the other hand, one could use different hyperelastic models for the different regions of dominant deformation such that the hyperelastic models are fitted to the appropriate characterisation data. As discussed in Section 5.2.4, while this alternative may deserve investigation, the potential gain in numerical agreement with experiment is small compared to the increase in characterisation cost.

Chapter 7: Conclusion

A review of the general mechanics of rubber was undertaken in this work which led to a better understanding of the assumptions implied in using hyperelastic models to predict the behaviour of this particular material. The methods employed to quasi-statically characterise a rubber compound in uniaxial, planar and equi-biaxial tension were discussed. Limitations of the hyperelastic models with respect to the characterisation data were identified while applying the curve-fitting tools available in ANSYSTM.

The following conclusions were drawn from curve-fitting preconditioned data:

- Currently available hyperelastic models used on their own fail to accurately predict uniaxial, planar and equi-biaxial tension data simultaneously (when considering the carbon-black-filled rubber characterised in this work).
- While higher-order hyperelastic models (such as third-order Yeoh or third-order Ogden models) may provide a better fit to the local nonlinearity of preconditioned data, they are highly inaccurate at strains that exceed the preconditioned strain level data they were fitted to.
- First-order hyperelastic models (such as the Neo-Hookean or first-order Yeoh) do not capture the local nonlinearity of preconditioned data, yet maintain an acceptable level of accuracy when at strains that exceed the preconditioned strain level data they were fitted to.

The difficulty in obtaining coefficients for a hyperelastic model that would predict the characterisation data accurately in all three states of simple stress simultaneously led to the development of the biaxiality test. Similarly, the considerable amount of softening of the rubber at hand due to preconditioning (the Mullins effect) and the failure of hyperelastic models to predict such behaviour led to the development of the preconditioning iteration.

Experimental bench tests were conducted to provide validation data for FEA simulations; they consisted of a cantilevered plate subjected to a bending load at its free end as well as

a rubber guide lug subjected to a transverse deflection. FEA models of the experimental bench tests were analysed in ANSYSTM. The preconditioning iteration and biaxiality test were applied to these simulations.

The following conclusions may be drawn from using the preconditioning iteration:

- The preconditioning iteration provides a successful alternative to predict the effect of preconditioning with hyperelastic materials.
- It is shown that accounting for the global behaviour of rubber which is the effect of strain-induced stress-softening with several, relatively linear, hyperelastic models (such as the first-order Yeoh model) in the preconditioning iteration is more important than using a single hyperelastic model that captures the local nonlinearity of a single preconditioned characterisation data curve.

The following conclusion may be drawn from the biaxiality test:

- In FEA simulations where the three dominant states of strain are present, fitting the hyperelastic models to the uniaxial tension data may be an acceptable compromise.

In light of these conclusions, potential leads for future work may be identified; they are listed as follows:

- Investigate the validity of the preconditioning iteration at higher strain levels (in light of Fig. 21).
- Account for strain rate effects (viscoelastic behaviour) and unrecoverable strain.
- Implement Dorfmann and Ogden's (2003) strain-energy-based pseudo-elastic theory, or a similar model, in ANSYSTM to predict Mullins effects and preconditioning.

It is clear from the characterisation data that the rubber at hand exhibits behaviour that cannot be predicted with hyperelastic models currently available in ANSYSTM. One of the major issues is the softening behaviour of the material due to the Mullins effect. This is addressed with the preconditioning iteration where elements are attributed hyperelastic

models according to their maximum principal strain, such that a static FEA simulation with common hyperelastic formulations artificially reproduces (without a constitutive material law) the effect of preconditioning. Using an appropriate constitutive relation to model the unrecoverable strain, the considerable hysteresis as well as the strain-induced stress-softening seen in the characterisation data would be most desirable.

References

- ANSYS, 2004. Training Manual: Advanced Structural Nonlinearities. First Edition. ANSYS Release 8.0. SAS IP, Inc.
- ANSYS, 2005. Release 10.0 Documentation. SAS IP, Inc.
- ANSYS, 2006. World Cup Workshops.
- Arruda, E.M., Boyce, M.C., 1993. A three-dimensional constitutive model for the large stretch behaviour of rubber elastic materials. *Journal of Mechanics and Physics of Solids* 41(2), 389-412.
- Bettinali, F., Dusi, A., 2004. Laminated rubber bearings for seismic applications. In *Mechanics and Thermomechanics of Rubberlike Solids*. Saccomandi, G., Ogden, R. W. (eds). Springer Wien, NY, 233-252.
- Dick, J.S., 2004. How to Improve Rubber Compounds: 1500 Experimental Ideas for Problem Solving. Hanser, Munich.
- Dorfmann, A., Ogden, R.W., 2003. A pseudo-elastic model for loading, partial unloading and reloading of particle reinforced rubber. *International Journal of Solids and Structures* 40, 2699-2714.
- Dufour, P., 2003. ANSYS Tips: Picking an Element Type for Structural Analysis. Belcan Engineering Group Inc.
- Freed, A.D., 1995. Natural strain. *Journal of Engineering Materials and Technology* 117(4), 379-385.
- Gent, A.N., 1996. A new constitutive relation for rubber. *Rubber Chemistry and Technology* 69, 59-61.
- Johnson, P.S., 2001. *Rubber Processing: An Introduction*. Hanser Publishers, Munich; Hanser Gardner Publications, Cincinnati.
- Lobo, H., Bethard, T. Practical Issues in the Development and Implementation of Hyperelastic Models. Datapoint Testing Services, <http://www.testpaks.com>, 2006.
- Mase, G.T., Mase, G.E., 1999. *Continuum Mechanics for Engineers* (2nd Edition). CRC Press, New-York.
- Muhr, A.H., Gough, J., Gregory, I.H., 1999. Experimental determination of model for liquid silicone rubber: Hyperelasticity and Mullins effect. *Proceedings of the First European*

- Conference on Constitutive Models for Rubber, Muhr, A.H., Dorfmann, A. (eds) Vienna, 181-187.
- Müller, I., Strehlow, P., 2004. Rubber and Rubber Balloons, Paradigms of Thermodynamics, Lecture Notes in Physics, 637. Springer-Verlag, Berlin.
- Mullins, L., 1969. Softening of rubber by deformation. Rubber Chemistry Technology 42, 339-362.
- Ogden, R.W., 1972a. Large deformation isotropic elasticity – on the correlation of theory and experiment for incompressible rubberlike solids. Proceedings of the Royal Society of London. Series A, Mathematical and Physical Sciences. 326(1567), 565-584.
- Ogden, R.W., 1972b. Large deformation isotropic elasticity – on the correlation of theory and experiment for compressible rubberlike solids. Proceedings of the Royal Society of London. Series A, Mathematical and Physical Sciences. 328(1575), 567-583.
- Ogden, R. W., 2004. Elasticity and inelasticity of rubber. In Mechanics and Thermomechanics of Rubberlike Solids. Saccomandi, G., Ogden, R. W. (eds). Springer Wien, NY, 135-185.
- Rivlin, R.S., 1948a. Large elastic deformations of isotropic materials. I. Fundamental concepts. Philosophical Transactions of the Royal Society of London, Series A, Mathematical and Physical Sciences 240(822), 459-490.
- Treloar, L.R.G., 1943. The elasticity of a network of long-chain molecules. I. Transactions of the Faraday Society 39, 36-41
- Treloar, L.R.G., 1944. Stress-strain data for a vulcanized rubber under various types of deformation. Transactions of the Faraday Society 40, 59.
- Treloar, L.R.G., 1975. The Physics of Rubber Elasticity (3rd ed.), Oxford University Press, Oxford.
- Sears, F.W., 1955. Thermodynamics, the Theory of Gases, and Statistical Mechanics. Addison-Wesley, Cambridge, MA.
- Schwer, L.E., 2006. ASME standards committee on verification and validation in computational solid mechanics. Proceedings of the Ninth Pan-American Congress on Applied Mechanics. Eischen J.W., Galindo G.M., (eds.), Mérida, Mexico, pp.86.
- Yeoh, O.H., 1990. Characterization of elastic properties of carbon-black-filled rubber vulcanizates. Rubber Chemistry and Technology 63, 792-805.

Yeoh, O.H., 1996. Phenomenological theory of rubber elasticity. In *Comprehensive Polymer Science*, Allen, G. (ed.). Elsevier, Oxford, Chapter 12.

Appendices

Appendix A: Strain energy derivation

The following derivation constitutes something of an exercise compiling pieces of previously achieved work, a great part of which may be found in *Mase and Mase (1999)*. It is nonetheless instructive as it provides the origin of the so-called hyperelastic models. The strain energy function is originally derived from the 1st law of Thermodynamics expressed as

$$\frac{D}{Dt}(K+U) = P + Q, \quad (\text{A.1})$$

where K is kinetic energy, U is internal energy, P is mechanical power and Q is the rate at which thermal energy is added to the body. The kinetic energy, internal energy, mechanical power and rate of added thermal energy may be expanded as follows:

$$K = \int_V \frac{1}{2} \rho v_i v_i dV, \quad (\text{A.2})$$

$$U = \int_V \rho u dV, \quad (\text{A.3})$$

$$P = \int_V \rho b_i v_i dV + \int_S t_i v_i dS, \quad (\text{A.4})$$

and

$$Q = \int_V \rho r dV - \int_S q_i n_i dS, \quad (\text{A.5})$$

respectively, where ρ is density, v_i is velocity defined by $\frac{\partial x_i}{\partial t}$, the overdot indicates $\frac{\partial}{\partial t}$, u

is internal energy per unit mass, b_i is a body force vector, t_i is a traction vector, r is the generated heat per unit mass by internal sources, q_i is a heat flux vector (in to the body) per unit surface area, and n_i is the previously defined unit vector normal to the surface.

Eq.(A.1) may thus be rewritten as

$$\int_V \rho (v_i \dot{v}_i + \dot{u}) dV = \int_V \rho b_i v_i dV + \int_S t_i v_i dS + \int_V \rho r dV - \int_S q_i n_i dS. \quad (\text{A.6})$$

Recall Gauss's theorem for surface integrals

$$\int_S A_{ij} n_j dS = \int_V A_{ij,j} dV, \quad (\text{A.7})$$

where the expression $A_{ij,j}$ is in Einstein notation and indicates a partial derivative with respect to x_j :

$$A_{ij,j} = \frac{\partial A_{ij}}{\partial x_j}. \quad (\text{A.8})$$

Neglecting thermal effects, substituting the traction vector t_i in to Eq.(2.23), applying Gauss's theorem and with a little manipulation Eq.(A.6) becomes

$$\int_V (\sigma_{ji,j} + \rho b_i - \rho \dot{v}_i) v_i dV + \int_V (\sigma_{ji} v_{i,j} - q_{i,i} + \rho r - \rho \dot{u}) dV = 0. \quad (\text{A.9})$$

The *local equation of motion* [defined by Mase and Mase (1999)] is identified as

$$\sigma_{ji,j} + \rho b_i = \rho \dot{v}_i, \quad (\text{A.10})$$

reducing Eq.(A.9) to

$$\dot{u} = \frac{1}{\rho} \sigma_{ji} v_{i,j}, \quad (\text{A.11})$$

since the volume integral is arbitrary. Assuming that the only change in internal energy is caused by strain, and defining the strain energy, W , such that $W = \rho_o u$, where ρ_o is the density at the reference state, Eq.(A.11) becomes

$$\dot{u} = \frac{1}{\rho_o} \frac{\partial \rho_o u}{\partial t} = \frac{1}{\rho_o} \frac{\partial W}{\partial t} = \frac{1}{\rho} \sigma_{ji} v_{i,j}. \quad (\text{A.12})$$

Applying the principle of conservation of mass and recalling Eq. (2.22), Eq.(A.12) may be expressed with the volumetric parameter, J , via

$$\frac{\partial W}{\partial t} = J \sigma_{ji} v_{i,j}. \quad (\text{A.13})$$

Manipulating the left-hand side of Eq.(A.13), it is shown that

$$\frac{\partial W}{\partial t} = \frac{\partial W}{\partial F_{ip}} \frac{\partial F_{ip}}{\partial t} = \frac{\partial W}{\partial F_{ip}} \frac{\partial v_i}{\partial X_p} = \frac{\partial W}{\partial F_{ip}} \frac{\partial v_i}{\partial x_j} \frac{\partial x_j}{\partial X_p} = \frac{\partial W}{\partial F_{ip}} F_{jp} v_{i,j}. \quad (\text{A.14})$$

Substituting the result of Eq.(A.14) back into Eq.(A.13) leads to

$$\left(J^{-1} F_{jp} \frac{\partial W}{\partial F_{ip}} - \sigma_{ji} \right) v_{i,j} = 0. \quad (\text{A.15})$$

It is obvious that one possible solution to Eq.(A.15) is the following:

$$\sigma_{ij} = J^{-1} F_{ip} \frac{\partial W}{\partial F_{jp}}. \quad (\text{A.16})$$

On the other hand, it can be shown (Mase and Mase, 1999) that

$$\frac{\dot{J}}{J} = v_{i,i}, \quad (\text{A.17})$$

meaning that, when the material is incompressible, the change in volume, \dot{J} , is null; thus $v_{i,i} = 0$, which leads to another possible solution for Eq.(A.15) expressed as follows:

$$\delta_{ij} v_{i,j} = 0, \quad (\text{A.18})$$

and this can be viewed as an internal constraint on the deformation gradient. Eqs.(A.15) and (A.18) may be combined to yield

$$J^{-1} F_{jp} \frac{\partial W}{\partial F_{ip}} - \sigma_{ji} = p \delta_{ij}, \quad (\text{A.19})$$

or rearranged into

$$\sigma_{ij} = J^{-1} F_{ip} \frac{\partial W}{\partial F_{jp}} - p \delta_{ij}, \quad (\text{A.20})$$

where the scalar p is conveniently chosen to represent the hydrostatic pressure serving as the internal constraint due to the incompressible response of the material. Note that the Cauchy stress tensor is symmetric here; thus $\sigma_{ij} = \sigma_{ji}$.

Assuming a state of simple strain (i.e. with no rotations) and considering only the principal axes, Eq.(A.20) reduces to

$$\sigma_i = \lambda_i S_i = \lambda_i \frac{\partial W}{\partial \lambda_i} - p \delta_{ij}, \quad (\text{A.21})$$

or expressing the strain energy as a function of the strain invariants, I_i , thus $W(I_1, I_2, I_3)$, obtained from the right Cauchy-Green tensor, Eq.(A.21) may also be written as

$$\sigma_i = \lambda_i S_i = \lambda_i \left[\frac{\partial W}{\partial I_1} \frac{\partial I_1}{\partial \lambda_i} + \frac{\partial W}{\partial I_2} \frac{\partial I_2}{\partial \lambda_i} \right] - p. \quad (\text{A.22})$$

Appendix B: Zero shift and corrected gauge length

The following provides details of the mathematical manipulations involved in zeroing the stress and strain data with respect to offset values due to unrecoverable strain. First, definitions for the original nominal strain, ε , the offset strain, $\varepsilon_{\text{offset}}$, and the zeroed strain, ε' , are given.

The original nominal strain, ε , is defined with respect to the original gauge length, L_o , such that

$$\varepsilon = \frac{L - L_o}{L_o}. \quad (\text{B.1})$$

The offset strain, $\varepsilon_{\text{offset}}$, is the strain that has not been recovered once the testpiece is load-free and is also defined with respect to the original gauge length, L_o :

$$\varepsilon_{\text{offset}} = \frac{L_{\text{offset}} - L_o}{L_o}. \quad (\text{B.2})$$

The zeroed strain, ε' , is defined with respect to the offset gauge length, L_{offset} , such that

$$\varepsilon' = \frac{L - L_{\text{offset}}}{L_{\text{offset}}}. \quad (\text{B.3})$$

To express ε' in terms of ε and $\varepsilon_{\text{offset}}$, using Eqs. (B.1), (B.2) and (B.3), the following manipulation may be followed:

$$\varepsilon' = \frac{L - L_{\text{offset}}}{L_{\text{offset}}} = \frac{\frac{L - L_o}{L_o} - \frac{L_{\text{offset}} - L_o}{L_o}}{1 + \frac{L_{\text{offset}} - L_o}{L_o}} = \frac{\varepsilon - \varepsilon_{\text{offset}}}{1 + \varepsilon_{\text{offset}}}, \quad (\text{B.4})$$

showing why, in the characterisation data, the offset strain, $\varepsilon_{\text{offset}}$, for each preconditioned curve is subtracted from all strain values for that curve, then divided by $(\varepsilon_{\text{offset}} + 1)$ to account for the larger stabilized gauge length.

Similarly, the nominal stress, S , is defined as

$$S = \frac{P}{A_o}, \quad (\text{B.5})$$

where P is the load and A_o is the initial cross sectional area. The zeroed stress, S' , is then defined by

$$S' = \frac{P}{A_{\text{offset}}}, \quad (\text{B.6})$$

where A_{offset} is the offset cross-sectional area. Since the material is assumed to be incompressible, the following volumetric compatibility equation must be satisfied:

$$A_o L_o = A_{\text{offset}} L_{\text{offset}} = V. \quad (\text{B.7})$$

Expressing S' in terms of S and the offset strain, ϵ_{offset} , leads to

$$S' = \frac{P}{A_{\text{offset}}} = \frac{P}{A_o} \frac{A_o}{A_{\text{offset}}} = S \frac{(V/L_o)}{(V/L_{\text{offset}})} S \frac{L_{\text{offset}}}{L_o} = S(\epsilon_{\text{offset}} + 1), \quad (\text{B.8})$$

showing that multiplying the stress values by $(\epsilon_{\text{offset}} + 1)$ accounts for the stabilized gauge cross-sectional area.

Appendix C: Characterisation data

The following tables provide the manipulated characterisation data for the three states of simple strain tested as well as the four levels of preconditioning.

Table C1: Uniaxial tension characterisation data

Virgin stretch		5%		10%		15%		25%		25% (cont'd)	
ε	σ [MPa]	ε	σ [MPa]	ε	σ [MPa]	ε	σ [MPa]	ε	σ [MPa]	ε	σ [MPa]
0.0000	0.0000	0.0000	0.0000	0.0000	0.0000	0.0000	0.0000	0.0000	0.0000	0.0975	1.0147
0.0021	0.1893	0.0030	0.1227	0.0024	0.0896	0.0035	0.1024	0.0026	0.0789	0.1003	1.0345
0.0038	0.2636	0.0061	0.2101	0.0050	0.1595	0.0060	0.1763	0.0047	0.1411	0.1033	1.0538
0.0062	0.3188	0.0083	0.2809	0.0078	0.2181	0.0094	0.2364	0.0071	0.1930	0.1065	1.0716
0.0090	0.3683	0.0122	0.3436	0.0112	0.2705	0.0118	0.2881	0.0100	0.2379	0.1096	1.0917
0.0118	0.4115	0.0140	0.4004	0.0139	0.3195	0.0147	0.3353	0.0131	0.2790	0.1130	1.1100
0.0146	0.4529	0.0180	0.4530	0.0166	0.3640	0.0180	0.3792	0.0148	0.3183	0.1155	1.1303
0.0176	0.4903	0.0205	0.5029	0.0197	0.4064	0.0202	0.4180	0.0186	0.3541	0.1186	1.1485
0.0205	0.5269	0.0229	0.5519	0.0229	0.4462	0.0229	0.4562	0.0217	0.3865	0.1213	1.1671
0.0228	0.5609	0.0255	0.5999	0.0258	0.4841	0.0257	0.4921	0.0245	0.4192	0.1240	1.1848
0.0258	0.5939	0.0288	0.6471	0.0288	0.5206	0.0284	0.5258	0.0270	0.4505	0.1264	1.2056
0.0289	0.6268	0.0312	0.6937	0.0310	0.5574	0.0339	0.5910	0.0302	0.4792	0.1289	1.2261
0.0306	0.6560			0.0343	0.5926	0.0366	0.6219	0.0327	0.5078	0.1323	1.2447
0.0338	0.6851			0.0368	0.6278	0.0400	0.6521	0.0350	0.5346	0.1354	1.2639
0.0366	0.7144			0.0393	0.6608	0.0431	0.6820	0.0387	0.5611	0.1369	1.2842
0.0398	0.7421			0.0423	0.6946	0.0457	0.7114	0.0406	0.5861	0.1402	1.3036
0.0427	0.7690			0.0446	0.7274	0.0484	0.7402	0.0437	0.6109	0.1430	1.3241
0.0449	0.7948			0.0478	0.7615	0.0542	0.7958	0.0462	0.6359	0.1461	1.3431
0.0483	0.8199			0.0506	0.7952	0.0569	0.8227	0.0500	0.6590	0.1487	1.3646
0.0999	1.2032			0.0534	0.8295	0.0597	0.8499	0.0528	0.6827	0.1516	1.3857
0.1500	1.4665			0.0561	0.8633	0.0627	0.8766	0.0558	0.7060	0.1541	1.4070
0.2475	1.8629			0.0589	0.8980	0.0652	0.9035	0.0585	0.7280	0.1574	1.4293
				0.0616	0.9345	0.0684	0.9302	0.0621	0.7503	0.1594	1.4509
				0.0644	0.9697	0.0735	0.9838	0.0643	0.7722	0.1621	1.4746
						0.0770	1.0096	0.0668	0.7937	0.1640	1.4977
						0.0797	1.0361	0.0701	0.8152	0.1670	1.5219
						0.0825	1.0634	0.0726	0.8359	0.1697	1.5458
						0.0852	1.0903	0.0755	0.8570	0.1721	1.5705
						0.0878	1.1177	0.0774	0.8773	0.1746	1.5981
						0.0906	1.1463	0.0805	0.8967	0.1774	1.6241
						0.0939	1.1750	0.0839	0.9180	0.1806	1.6515
						0.0963	1.2040	0.0857	0.9372		
						0.0991	1.2343	0.0890	0.9573		
						0.1015	1.2647	0.0913	0.9765		
						0.1039	1.2955	0.0949	0.9960		

Table C2: Planar tension characterisation data

Virgin stretch		5%		10%		15%		15% (cont'd)	
ε	σ [MPa]	ε	σ [MPa]	ε	σ [MPa]	ε	σ [MPa]	ε	σ [MPa]
0.0000	0.0000	0.0000	0.0000	0.0000	0.0000	0.0000	0.0000	0.0731	1.3626
0.0012	0.1308	0.0012	0.1196	0.0014	0.0894	0.0015	0.0989	0.0751	1.3873
0.0031	0.2158	0.0027	0.2164	0.0028	0.1614	0.0031	0.1764	0.0765	1.4161
0.0045	0.2855	0.0044	0.2952	0.0051	0.2269	0.0049	0.2417	0.0785	1.4372
0.0063	0.3416	0.0061	0.3667	0.0066	0.2810	0.0067	0.2931	0.0806	1.4644
0.0078	0.3997	0.0073	0.4313	0.0087	0.3360	0.0087	0.3464	0.0824	1.4910
0.0095	0.4500	0.0096	0.4937	0.0104	0.3790	0.0105	0.3920	0.0840	1.5196
0.0110	0.4974	0.0111	0.5464	0.0123	0.4289	0.0121	0.4367	0.0862	1.5440
0.0125	0.5423	0.0131	0.6000	0.0140	0.4710	0.0142	0.4725	0.0878	1.5720
0.0145	0.5861	0.0143	0.6536	0.0155	0.5173	0.0157	0.5121	0.0893	1.5995
0.0161	0.6268	0.0165	0.7053	0.0174	0.5527	0.0176	0.5485	0.0914	1.6238
0.0176	0.6726	0.0179	0.7503	0.0191	0.5938	0.0191	0.5834	0.0933	1.6573
0.0197	0.7052	0.0196	0.8011	0.0208	0.6316	0.0214	0.6126	0.0949	1.6863
0.0220	0.7440	0.0213	0.8503	0.0227	0.6691	0.0229	0.6512	0.0969	1.7220
0.0237	0.7778	0.0235	0.8943	0.0243	0.7003	0.0247	0.6812	0.0989	1.7484
0.0255	0.8142	0.0246	0.9444	0.0264	0.7398	0.0264	0.7141		
0.0272	0.8456	0.0265	0.9936	0.0280	0.7720	0.0292	0.7419		
0.0292	0.8770	0.0281	1.0438	0.0300	0.8077	0.0304	0.7734		
0.0310	0.9068			0.0322	0.8418	0.0321	0.8024		
0.0327	0.9307			0.0338	0.8737	0.0339	0.8314		
0.0349	0.9645			0.0359	0.9056	0.0356	0.8381		
0.0369	0.9908			0.0374	0.9401	0.0375	0.8837		
0.0388	1.0212			0.0392	0.9699	0.0395	0.9102		
0.0410	1.0427			0.0412	1.0020	0.0416	0.9386		
0.0428	1.0712			0.0431	1.0348	0.0431	0.9639		
0.0449	1.0967			0.0443	1.0429	0.0453	0.9896		
0.0465	1.1234			0.0458	1.0968	0.0472	1.0156		
0.0486	1.1408			0.0475	1.1280	0.0489	1.0421		
0.0998	1.6239			0.0497	1.1620	0.0510	1.0652		
0.1478	1.9003			0.0514	1.1933	0.0527	1.0888		
0.2494	2.3635			0.0537	1.2303	0.0545	1.1157		
				0.0554	1.2643	0.0562	1.1319		
				0.0571	1.3022	0.0585	1.1626		
				0.0586	1.3345	0.0600	1.1879		
				0.0602	1.3730	0.0620	1.2140		
						0.0641	1.2369		
						0.0658	1.2644		
						0.0676	1.2866		
						0.0695	1.3141		
						0.0713	1.3381		

Table C2 (continued): Planar tension characterisation data

25%		25% (cont'd)		25% (cont'd)	
ϵ	σ [MPa]	ϵ	σ [MPa]	ϵ	σ [MPa]
0.0000	0.0000	0.0741	1.1522	0.1497	1.8505
0.0016	0.0893	0.0759	1.1686	0.1519	1.8724
0.0037	0.1560	0.0779	1.1857	0.1537	1.8849
0.0052	0.2132	0.0800	1.2039	0.1556	1.9128
0.0070	0.2623	0.0818	1.2158	0.1572	1.9352
0.0090	0.3072	0.0836	1.2403	0.1593	1.9584
0.0111	0.3392	0.0859	1.2557	0.1607	1.9802
0.0125	0.3840	0.0874	1.2749	0.1626	2.0051
0.0145	0.4206	0.0895	1.2918	0.1652	2.0297
0.0164	0.4544	0.0916	1.3102	0.1664	2.0534
0.0182	0.4849	0.0933	1.3270	0.1683	2.0786
0.0200	0.5160	0.0951	1.3442	0.1701	2.1026
0.0218	0.5439	0.0970	1.3605	0.1716	2.1292
0.0232	0.5728	0.0986	1.3777	0.1735	2.1594
0.0252	0.6000	0.1005	1.3953		
0.0273	0.6263	0.1023	1.4115		
0.0295	0.6528	0.1044	1.4272		
0.0310	0.6788	0.1064	1.4442		
0.0330	0.7029	0.1086	1.4609		
0.0348	0.7263	0.1102	1.4762		
0.0363	0.7495	0.1124	1.4928		
0.0383	0.7702	0.1139	1.5084		
0.0399	0.7939	0.1161	1.5266		
0.0418	0.8136	0.1180	1.5390		
0.0436	0.8393	0.1194	1.5591		
0.0457	0.8565	0.1217	1.5768		
0.0478	0.8809	0.1239	1.5968		
0.0496	0.9025	0.1259	1.6110		
0.0516	0.9247	0.1272	1.6319		
0.0535	0.9444	0.1290	1.6482		
0.0553	0.9637	0.1309	1.6676		
0.0571	0.9846	0.1333	1.6793		
0.0590	1.0040	0.1349	1.7013		
0.0612	1.0156	0.1371	1.7195		
0.0627	1.0409	0.1386	1.7399		
0.0649	1.0598	0.1406	1.7574		
0.0665	1.0808	0.1425	1.7776		
0.0684	1.0979	0.1441	1.7960		
0.0704	1.1165	0.1460	1.8135		
0.0723	1.1350	0.1479	1.8340		

Table C3: Equi-biaxial extension characterisation data



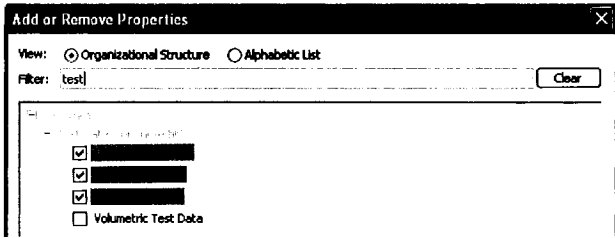
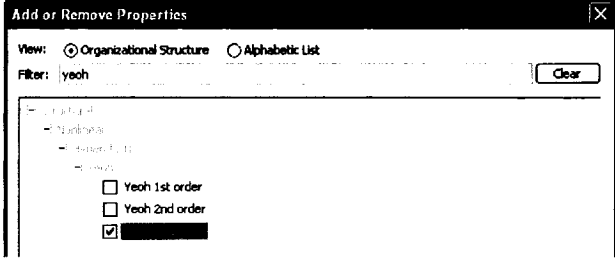
Virgin stretch		5%		10%		10% (cont'd)		15%		15% (cont'd)	
ϵ	σ [MPa]	ϵ	σ [MPa]	ϵ	σ [MPa]	ϵ	σ [MPa]	ϵ	σ [MPa]	ϵ	σ [MPa]
0.0000	0.0000	0.0000	0.0000	0.0000	0.0000	0.0606	1.5965	0.0000	0.0000	0.0623	1.3868
0.0001	0.0163	0.0007	0.0455	0.0006	0.0408	0.0623	1.6386	0.0004	0.0405	0.0642	1.4107
0.0004	0.0327	0.0019	0.1047	0.0016	0.0929	0.0638	1.6823	0.0005	0.0858	0.0659	1.4355
0.0007	0.0569	0.0033	0.1727	0.0031	0.1538	0.0656	1.7292	0.0019	0.1416	0.0678	1.4602
0.0012	0.0915	0.0050	0.2430	0.0047	0.2164	0.0672	1.7781	0.0036	0.2018	0.0696	1.4840
0.0019	0.1357	0.0064	0.3100	0.0063	0.2770			0.0052	0.2600	0.0713	1.5087
0.0027	0.1855	0.0082	0.3748	0.0080	0.3337			0.0070	0.3142	0.0731	1.5344
0.0037	0.2402	0.0095	0.4366	0.0095	0.3872			0.0084	0.3658	0.0748	1.5591
0.0048	0.2990	0.0110	0.4949	0.0110	0.4372			0.0098	0.4142	0.0765	1.5848
0.0065	0.3591	0.0124	0.5517	0.0124	0.4858			0.0112	0.4600	0.0783	1.6114
0.0082	0.4182	0.0138	0.6068	0.0138	0.5322			0.0127	0.5035	0.0800	1.6373
0.0098	0.4760	0.0150	0.6598	0.0150	0.5765			0.0142	0.5450	0.0819	1.6644
0.0114	0.5322	0.0163	0.7112	0.0166	0.6191			0.0156	0.5837	0.0837	1.6918
0.0131	0.5873	0.0176	0.7627	0.0179	0.6607			0.0171	0.6218	0.0854	1.7185
0.0147	0.6403	0.0189	0.8118	0.0193	0.6995			0.0188	0.6580	0.0873	1.7495
0.0165	0.6919	0.0202	0.8618	0.0208	0.7372			0.0203	0.6930	0.0891	1.7800
0.0179	0.7417	0.0214	0.9107	0.0223	0.7746			0.0221	0.7265	0.0909	1.8110
0.0193	0.7900	0.0226	0.9615	0.0239	0.8114			0.0238	0.7592	0.0927	1.8440
0.0208	0.8321	0.0241	1.0102	0.0254	0.8468			0.0254	0.7903	0.0946	1.8777
0.0223	0.8806	0.0252	1.0616	0.0271	0.8811			0.0271	0.8214	0.0964	1.9138
0.0237	0.9239	0.0266	1.1130	0.0286	0.9145			0.0288	0.8515	0.0982	1.9506
0.0253	0.9652	0.0280	1.1692	0.0303	0.9470			0.0303	0.8805	0.1000	1.9890
0.0268	1.0047	0.0292	1.2276	0.0318	0.9798			0.0319	0.9081	0.1018	2.0319
0.0282	1.0435			0.0334	1.0113			0.0335	0.9368	0.1036	2.0750
0.0296	1.0800			0.0349	1.0339			0.0350	0.9639	0.1054	2.1212
0.0311	1.1160			0.0364	1.0737			0.0366	0.9911		
0.0325	1.1513			0.0380	1.1045			0.0381	1.0173		
0.0338	1.1844			0.0395	1.1349			0.0398	1.0436		
0.0352	1.2180			0.0408	1.1654			0.0414	1.0691		
0.0366	1.2496			0.0424	1.1961			0.0430	1.0946		
0.0380	1.2806			0.0439	1.2269			0.0445	1.1195		
0.0395	1.3104			0.0454	1.2571			0.0461	1.1443		
0.0412	1.3399			0.0469	1.2877			0.0478	1.1699		
0.0427	1.3686			0.0484	1.3185			0.0493	1.1941		
0.0441	1.3954			0.0498	1.3499			0.0509	1.2182		
0.0458	1.4220			0.0513	1.3814			0.0525	1.2421		
0.0475	1.4488			0.0530	1.4141			0.0542	1.2654		
0.0492	1.4743			0.0544	1.4483			0.0557	1.2892		
0.0981	2.0055			0.0561	1.4827			0.0574	1.3133		
0.1498	2.3401			0.0576	1.5187			0.0590	1.3379		
0.2486	2.8646			0.0591	1.5561			0.0608	1.3621		

Table C3 (continued): Equi-biaxial extension characterisation data



25%		25% (cont'd)		25% (cont'd)	
ε	σ [MPa]	ε	σ [MPa]	ε	σ [MPa]
0.0000	0.0000	0.0635	1.2197	0.1411	1.9806
-0.0005	0.0421	0.0651	1.2367	0.1432	2.0035
0.0006	0.0868	0.0670	1.2564	0.1453	2.0275
0.0021	0.1408	0.0688	1.2745	0.1475	2.0513
0.0037	0.1975	0.0706	1.2925	0.1495	2.0761
0.0053	0.2515	0.0722	1.3121	0.1517	2.1010
0.0068	0.3027	0.0740	1.3306	0.1540	2.1255
0.0081	0.3503	0.0758	1.3486	0.1562	2.1530
0.0094	0.3949	0.0776	1.3670	0.1584	2.1798
0.0110	0.4362	0.0794	1.3853	0.1605	2.2078
0.0127	0.4765	0.0812	1.4037	0.1627	2.2367
0.0143	0.5142	0.0831	1.4219	0.1648	2.2670
0.0161	0.5505	0.0850	1.4402	0.1671	2.2995
0.0178	0.5847	0.0869	1.4582	0.1693	2.3315
0.0195	0.6172	0.0888	1.4762	0.1713	2.3666
0.0211	0.6485	0.0908	1.4928	0.1734	2.4034
0.0229	0.6783	0.0927	1.5112	0.1755	2.4428
0.0245	0.7066	0.0946	1.5288	0.1774	2.4829
0.0263	0.7355	0.0963	1.5464	0.1797	2.5262
0.0280	0.7629	0.0983	1.5655	0.1816	2.5668
0.0297	0.7893	0.1001	1.5840		
0.0313	0.8156	0.1022	1.6028		
0.0330	0.8405	0.1041	1.6201		
0.0347	0.8644	0.1060	1.6390		
0.0364	0.8879	0.1078	1.6585		
0.0378	0.9108	0.1097	1.6770		
0.0394	0.9339	0.1118	1.6960		
0.0411	0.9567	0.1139	1.7149		
0.0427	0.9786	0.1158	1.7323		
0.0444	0.9996	0.1179	1.7514		
0.0460	1.0209	0.1202	1.7685		
0.0477	1.0420	0.1222	1.7897		
0.0494	1.0632	0.1243	1.8093		
0.0511	1.0840	0.1264	1.8288		
0.0529	1.1045	0.1284	1.8496		
0.0546	1.1239	0.1305	1.8703		
0.0564	1.1438	0.1327	1.8916		
0.0581	1.1627	0.1349	1.9132		
0.0599	1.1822	0.1367	1.9350		
0.0618	1.2007	0.1389	1.9578		

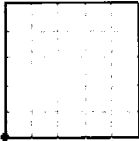
Appendix D: Curve-fitting demo in Workbench 10.0

The following is a demo on how to use the curve-fitting tool in Workbench 10.0 for hyperelastic materials. It is adapted from a demonstration written by the author of this thesis for the ANSYS™ World Cup (2006).

Steps and points to convey	Picture Guide
<p>Material Property Data (curve-fitting)</p> <ol style="list-style-type: none"> 1) In the top main menu, select the Data icon; . 2) RMB click on “Materials” in left tree menu and select  Insert New Material. 3) Name it (e.g. SEAL_RUBBER) 4) Select the <u>Add/Remove Properties</u> link under the structural properties of your new material and add Uniaxial, Biaxial and Shear Test Data as well as a third-order Yeoh hyperelastic model, when you are done, select “OK”. Try using the Filter: first type “test” and select the test data for curve-fitting, then type “yeoh” and select the third-order Yeoh model. 	 

Input the test data

- 5) Open the provided text files (test_ST.txt, test_EB.txt and test_PT.txt) in Excel, TextPad or equivalent (must recognize tab delimited data).
- 6) Back to the Engineering Data tab in the Workbench Environment, select  in the  tab. (Yellow usually indicates incomplete data in the Engineering Data Tab).
- 7) Copy the entire content of test_ST.txt (ctrl + C, or RMB click → Copy) then click in the first cell of the strain data and paste (ctrl + P, or RMB click → Paste) the content of the clipboard. The entire data of the test_ST.txt file should copy into the Stress vs. Strain columns.
- 8) Select the “Biaxial Test Data” box



Biaxial Test Data

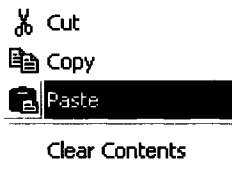
at the bottom right of the screen, and repeat the above operations with the test_EB.txt file.

Repeat again for the Pure Shear data in the test_PT.txt file.


SEAL_RUBBER - Uniaxial Test Data

Stress vs. Strain

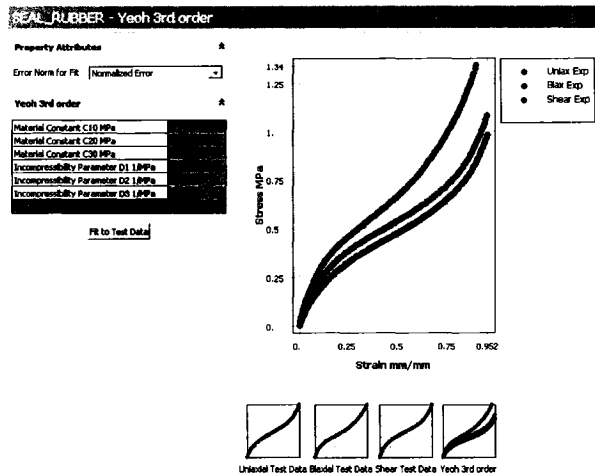
	Strain mm/mm	Stress MPa
1		
2		
3		
4		
5		
6		
7		
8		
9		
10		
11		
12		
13		
14		
15		



Curve-fitting



- 9) Similarly to the previous steps, select the “Yeoh third-order” figure at the bottom right of the screen. You should see a screen shot similar to the one on the right.
- 10) Click on Fit to Test Data and take a look at the fitted third-order Yeoh curves on the right.
- 11) Under “Property Attributes”, change the “Error Norm for Fit” to “Absolute Error” rather than the current “Normalized Error” selection.
- 12) Again, click on Fit to Test Data and recheck the fitted curves on the right; these coefficients will be acceptable for the current analysis.
- 13) Select  Close Curve icon along the top menu.

NOTE: Since no volumetric data was inputted, the incompressibility parameters are set to zero, meaning that the material will be assumed to be incompressible.



Exporting the material library

NOTE: Although you can just use the currently defined material in your simulation, you might want to use it again without having to go through all the steps you just went through. The following allows you to create a Material Library in which you can save several material models and quickly access them in the future when performing other simulations.

- 14) Select the  Export  icon, then "Selected Engineering Data to a Library". Note that you can also save the data in an existing library.
- 15) Select a library name general enough to encompass other material models you expect to save in the same library. In this case, we called our library RUBBER_MPL.

